# Spin-polarized scanning tunneling microscopy studies on in-plane magnetization components of thin antiferromagnetic films on Fe(001)

## Dissertation

zur Erlangung des akademischen Grades

doctor rerum naturalium (Dr. rer. nat.)

vorgelegt der

Mathematisch-Naturwissenschaftlich-Technischen Fakultät
(mathematisch-naturwissenschaftlicher Bereich)
der Martin-Luther-Universität Halle-Wittenberg

von Frau Katharina Uta Schlickum
geb. am: 01. Januar 1976 in: Herdecke

Gutachter /in

1. Prof. Dr. J. Kirschner

2. Prof. Dr. I. Mertig

3. Prof. Dr. U. Köhler

Halle (Saale), den 02.02.2005

II

# Contents

# Chapter 1

# Introduction

Magnetic nano structures are of great importance for modern applications. Hand in hand with the ongoing miniaturization of magnetic devices new questions of the magnetic behavior on the reduced length scale arise. In the last decades, the recording density has increased immensely by decreasing the size of magnetic areas in which information is stored (down to some 10 nm). This trend is still continuing and magnetic structures on the atomic scale are the aim. The imaging of magnetic arrangements at the nanometer or even atomic length scale is of fundamental interest as well [1, 2]. It provides insights into new and elementary behavior of magnetic phenomena.

In many magnetic devices, antiferromagnets in direct contact to ferromagnets play an essential role, though fundamental properties concerning the interplay between both are not fully understood. In the last years, spin-polarized scanning tunneling spectroscopy (Sp-STS) [3] and spin-polarized scanning tunneling microscopy (Sp-STM) [4] became powerful tools to investigate magnetic structures on the nanometer scale. Even antiferromagnetic surfaces can be imaged with these methods [5, 6]. In this work, Sp-STM is extended successfully to image a well-defined magnetic in-plane component [7]. This method was applied to study the behavior of magnetic frustration at the surface of thin antiferromagnetic films which are in direct contact to a ferromagnetic substrate [8].

The first prove that a magnetic body may consist of areas where the magnetization points in different directions was given by Barkhausen in 1919 [9]. Starting from this, new methods that allow the direct imaging of magnetic pattern in real space have been invented. Real space imaging methods have the advantage over methods working in the reciprocal space that they are capable to investigate non periodic and localized magnetic structures. With the development of the first methods, one of the main effort has always been to improve the resolution to be able to investigate smaller structures. Recently, the challenge has reached to image magnetic structures on the atomic scale [10].

Up to now, several techniques have been developed exploiting different physical effects and the most important are shortly introduced below. Magnetic imaging

techniques can be divided into two groups. On the one hand, there are methods that map the local magnetic field which is emerging from the sample (local magnetic stray field). On the other hand, there are methods which investigate internal properties determined by the local magnetization. Since the interest typically lies on the local magnetization, the techniques investigating the magnetic stray field have the disadvantage that only a limited conclusion can be drawn to the arrangement of the local magnetization pattern.

The first real space picture of magnetic patterns was obtained by mapping the distribution of small magnetic particles (magnetic powder) arranged along flux lines of the local stray field by Bitter in 1932 [11]. Nowadays, a resolution of some 10 nm has been achieved with the Bitter-technique [12]. Another technique that is sensitive to the magnetic stray field is magnetic force microscopy [13]. Here, the magnetostatic interaction between a magnetic tip and the stray field of the sample is analyzed with respect to the lateral tip position. This method belongs to the well established magnetic imaging techniques because of the simplicity of operation and the easily achievable high lateral resolution between 20 and 100 nm [14]. One technique that is sensitive to the local magnetization components is the magneto-optic Kerr microscopy [15]. This method analyzes changes of the polarization of light caused by the reflection from a magnetic sample surface. The lateral resolution is limited by the wave length of the light. By performing so-called near field microscopy measurements the resolution was enhanced to below 200 nm [16–18]. Various types of electron microscopes have been developed which analyze electrons emitted, reflected from, or transmitted through a magnetic sample. One important method is scanning electron microscopy with polarization analysis (SEMPA) [19]. Here, a focussed high energy (keV) electron beam is scanned over a sample surface and the emitted low-energy secondary electrons are analyzed with respect to their spin. The spin reflects the local magnetization of the sample near the surface. This method allows the measurement of all three spatial magnetization components and the reflectivity of a sample surface, independently. A lateral resolution better than 10 nm has been achieved, recently [20–23]. Another technique, the so called photoemission electron microscopy has the additional advantage that the magnetic structure can be imaged element specifically by exploiting the different absorption energies of core-level electrons. Thus, it is possible to address element specific magnetic layers within multilayered structures and in alloyed films [24]. All these methods yield insight into micromagnetic phenomena and will do so in the future. However, there is need for techniques with a higher lateral resolution.

Binnig and Rohrer's [25] development of scanning tunneling microscopy (STM) allowed to image the topography of a sample surface with atomic resolution [26]. Since than the question arose wether the analysis of the electron spin can be used to map magnetic structures on the atomic scale as well. This idea was first mentioned by Pierce [27]. He suggested to use the effect of tunneling magneto resistance discovered in 1975 by Jullière [28]. Jullière showed, that the tunneling probability between two ferromagnetic electrodes separated by an insulator depends on the

relative orientation of the magnetization of both. The first pioneering works on Sp-STM experiments have been performed in the beginning of 1990. In these experiments, the spin-dependent tunneling current between ferromagnetic tips and magnetic samples was measured in air [29] and under vacuum [30], but it was not possible to separate the topographic and magnetic information. A further, but unsuccessful development was to try to separate the magnetic information from the topography by using optically pumped semiconducting GaAs tips [31–33].

Recently, the attempt to investigate the spin-dependent tunneling current between a ferromagnetic tip and magnetic samples received new interest. As already mentioned, two successfully experimental approaches have been developed which allow the separation of magnetic and topographic information. Bode and coworkers developed Sp-STS [3] to image the magnetic structure of a sample surface and Wulfhekel and coworkers designed a Sp-STM [4]. Both techniques allow imaging of magnetic structures with a high lateral resolution of at least 1 nm [34, 35].

In thin films and at the surface of bulk samples, the magnetization lies often in the plane of the surface because of shape effects (shape anisotropy). Therefore, it is of high interest to investigate a well-defined in-plane component of the magnetization with the Sp-STM. As shown in this work, this is achieved by the proper choice of the Sp-STM electrode [7]. In our approach, we use ferromagnetic rings instead of conventionally sharp tips as STM-electrodes. A high lateral resolution of 1 nm has been achieved using these rings, comparable to the resolution achieved for the out-of-plane component.

The advantage of Sp-STM measurements is that changes in the electronic structure can be separated clearly from the magnetic signal which allows the investigation of alloys and of systems having unknown electronic structures. Also a well-defined in-plane component of the magnetization was imaged whereas in Sp-STS only one random in-plane component can be measured.

In the following chapter, a short overview is given on the static behavior of magnetic phenomena. The focus lies on combined systems consisting of a ferromagnet that is in direct contact with an antiferromagnet. The principle of tunneling, STM and the extension to Sp-STM are introduced in the last part of chapter 2. The experimental setup, the realization of Sp-STM measurements and the preparation of Sp-STM ring electrodes are described in the first part of chapter 3. To confirm the imaging of a well-defined in-plane component, the method was tested on Fe-whiskers which have well known magnetic patterns (second part of chapter 3). The capability of high lateral resolution of Sp-STM is used to investigate local magnetically frustrated regions down to 1 nm, formed in thin antiferromagnetic Mn films grown on Fe(001). The magnetic frustration within Mn films is caused by interface roughness of the underlying Fe substrate and was imaged at the Mn film surface (first part of chapter 4). It was found that the measured size and sign of the spin contrast strongly depends on the bias voltage (second part of chapter 4). The results obtained on thin Mn films on Fe(001) are discussed in chapter 5. The magnetically frustrated regions are compared to simple continuum approximations and to calculations performed

on the basis of a Heisenberg model. For the understanding of the voltage dependent spin contrast the experimental data are discussed in the framework of theoretical calculations.

# Chapter 2

# Theoretical background

The first part of this chapter gives an overview of the main static magnetic behavior of itinerant ferromagnetic and antiferromagnetic materials. The formation of the magnetic order is described. A more detailed discussion focuses on ferromagnetic systems in direct contact to antiferromagnets.

In this work, spin-polarized scanning tunneling microscopy (Sp-STM) is used to investigate the local magnetic structure at sample surfaces. The basic principles of this technique are summarized in the second part of this chapter.

## 2.1 Itinerant ferromagnets and antiferromagnets

Ferromagnetic and antiferromagnetic solids are characterized by magnetic moments which show magnetic order below a critical temperature. For ferromagnets this ordering temperature is called Curie-temperature ($T_C$) and for antiferromagnets Néel-temperature ($T_N$). The spontaneous order of the magnetic moments is caused by an interaction between them. The ferromagnets Fe, Co, Ni and antiferromagnets Cr and Mn are 3d metals, in which itinerant electrons carry the magnetic moments. In these materials, the magnetic moments are mainly caused by the electron spin. The orbital magnetic moments are quenched because of a strong inhomogeneous electrical field in these crystals [36]. The strongest interaction, which is responsible for the magnetic order, is the exchange interaction. This interaction results from the quantum mechanical properties of the indistinguishability of the electrons, but the origin is the electrostatic Coulomb interaction.

In the Heisenberg model [37], the Hamiltonian describes the exchange interaction of localized magnetic moments. In the case that the total magnetic moment is dominated by the moments of the electron spins, the Hamiltonian can be expressed by:

$$H = -\frac{1}{2} \sum_{i,j \neq i} J_{ij} \overrightarrow{S}_i \cdot \overrightarrow{S}_j \tag{2.1}$$

where $\overrightarrow{S}_{i(j)}$ is the total spin moment of the atom at the position $i(j)$. $J_{ij}$ is the
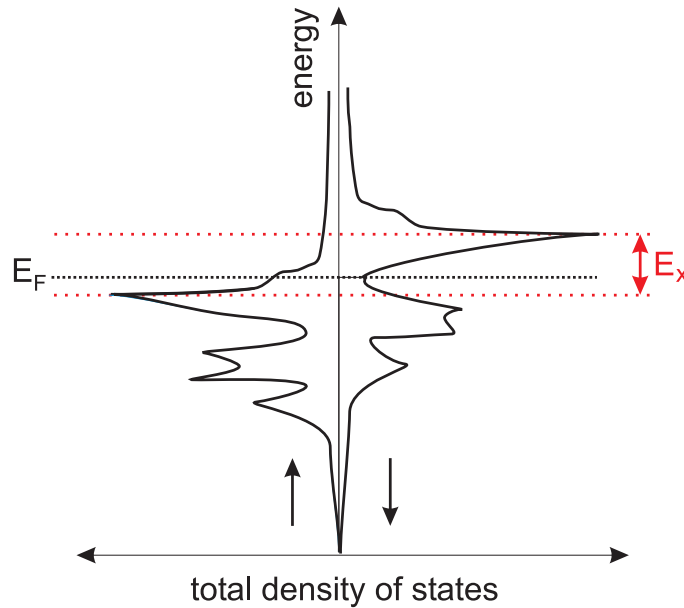
Figure 2.1: Total density of states of bulk Fe showing the exchange splitting by the amount $E_x$ between majority electrons ($\uparrow$) and minority electrons ($\downarrow$) [42]. The Fermi energy is indicated by $E_F$.

exchange coupling constant between particular magnetic moments. When the sign of $J_{ij}$ is positive the lowest energy is reached for parallel alignment of spins, which means ferromagnetic order is preferred. For negative sign, the spins do not couple parallel so that the total magnetic moment vanishes. Antiferromagnetic order is preferred. For a detailed description see for example [38]. Later (in section 5.1.2), a Heisenberg model is used to model the micromagnetic behavior of the system under investigation.

In 3d metals, the itinerant electrons are not localized but arranged in bands. The magnetic order in these materials was discussed by Stoner [39, 40]. The requirement for ferromagnetism, i.e. the Stoner criterium, is that the product of the density of states at the Fermi energy and the exchange interaction is larger than a critical value. For details see for example Ref. [41]. If the Stoner criterium is fulfilled, a splitting of the bands for spin up and spin down electrons occurs and due to the fact that the Fermi energy for both spin directions has to be the same a difference in the occupation for spin up and spin down electrons is caused. Such a situation is present in the 3d ferromagnetic metals Fe, Co and Ni. In these metals, the bands are exchange split and the summation over all occupied states yields a greater number of so-called majority electrons than of minority electrons resulting in a net magnetic moment. Fig. 2.1 shows the spin-polarized density of states of bcc Fe which arises by integrating over all states having different wave vectors but the same energy. The exchange splitting between the bands is indicated by the energy $E_x$. Because of the exchange splitting, the occupation for majority and minority electrons close to the

Fermi level is different resulting in a spin polarization of the conduction electrons. The spin polarization at the Fermi energy is given by the density of states at this energy. The spin polarization close to the Fermi level is an important quantity in this work because this property is used in Sp-STM, as will be shown later (see section 2.3).

The difference between ferromagnetism and antiferromagnetism is the absence of a net magnetic moment in one magnetic unit cell, in the latter case. Different types of antiferromagnetic order exist and one special case is the antiparallel coupling of neighboring magnetic moments. When introducing a surface along specific crystallographic directions in these antiferromagnets, the neighboring antiferromagnetic order can result in uncompensated surfaces. In this case, the neighboring magnetic moments within one layer are coupled ferromagnetically but antiferromagnetically to adjacent layers. Thus, the net magnetic moment of each separate monolayer (ML) is non zero. These types of antiferromagnets are called layer-wise antiferromagnets. Examples are NiO(111) [43], Cr(001) [5], Cr/Fe(001) [44,45] and Mn/Fe(001) [46,47]. In this work, the uncompensated surfaces of the layer-wise antiferromagnetic ordered films of Mn/Fe(001) and Cr/Fe(001) are studied by Sp-STM.

## 2.1.1 Domains and domain walls

In a magnetic material, the magnetization prefers to lie along certain crystallographic directions, the so-called easy axes. This is caused by the magneto-crystalline anisotropy.

A magnetic particle having a net magnetization has magnetic poles producing magnetic surface charges. These charges result in a magnetic stray field containing magnetic energy which is energetically unfavorable. The reduction of the stray field energy is achieved by aligning the magnetic moments parallel to the particle boundary to obtain a magnetic closed flux.

A direct consequence of these energy contributions is that the magnetic order in a ferromagnetic particle may split up into domains. Within the domains, the magnetic moments are pointing in one direction. In different domains they are often aligned along different easy axes [48]. A continuous transition between adjacent domains is formed by domain walls. Two different kinds of domain walls exist: Bloch walls, where the magnetization rotates in the plane of the wall and Néel walls, where the magnetization rotates perpendicular to the plane of the wall. The width of natural bulk domain walls is determined by the competition between the anisotropy and the exchange energy. The exchange alone would result in an infinitely wide wall, where the angle between neighboring magnetic moments is infinitesimal small, whereas the anisotropy would prefer an atomically sharp transition.

By using a magnetic continuum model, the width of static domain walls can be calculated. In this model, the magnetization is taken as a continuum in space and the atomistic discretization is neglected. This model is naturally limited to large structures, where atomistic details are not important. In general, there are
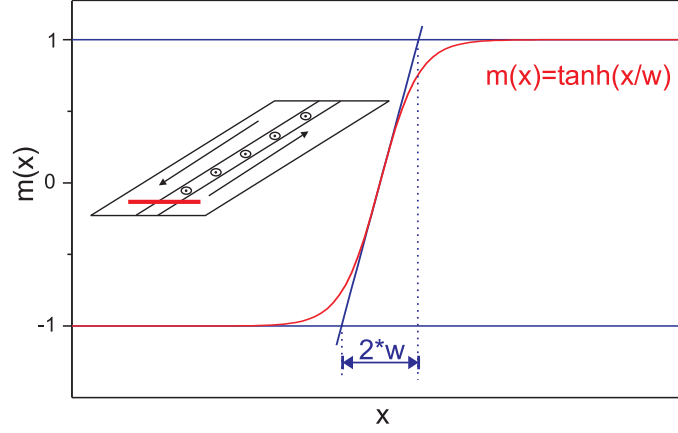
Figure 2.2: A magnetic line profile calculated for a 180° bulk wall. The line profile is a *tanh*-function and the width of the domain wall is given by $2w$. In the inset, the underlying magnetic configuration is shown.

no analytical solutions for the equilibrium magnetic structure in three dimensions when considering all energetic terms. However, an analytical solution can be found for the wall profile in a one-dimensional 180° domain wall when considering only the magneto-crystalline anisotropy and the exchange interaction and neglecting the stray field [48]. The resulting profile is a simple *tanh*-function

$$m(x) \propto tanh(x/w). \tag{2.2}$$

Here, $m(x)$ is the normalized projection of the magnetization along the direction perpendicular to the domain wall (along the red line in the inset of Fig. 2.2). The domain wall width ($2w$) is defined by the crossings of the tangent at $m(0)$ with the saturation lines, see Fig. 2.2. Throughout this work, the *tanh*-function is used to determine wall widths between two domains. For a 180° Bloch wall the width is given by

$$w = 2\sqrt{A/K} \tag{2.3}$$

where $K$ is the anisotropy constant and $A$ is the exchange constant [48]. By considering the lattice constant $a$ of the crystal, $J$ and $A$ are related by:

$$A = \frac{JS^2}{a}c \tag{2.4}$$

where $c =$1, 2 or 4 for a simple cubic, bcc or fcc crystal structure, respectively [38].

For thick films or in bulk crystals, typically Bloch walls are formed as these walls are free of magnetic charges. At the surface, Bloch walls produce magnetic charges and thus create a stray field. Néel walls are not charge free in the interior of the wall. They, however, produce no charges at the sample surface. Therefore, Néel walls are often energetically more favorable at surfaces and in thin films [48]. To minimize the energy of bulk walls, the direction of rotation of the magnetization near the
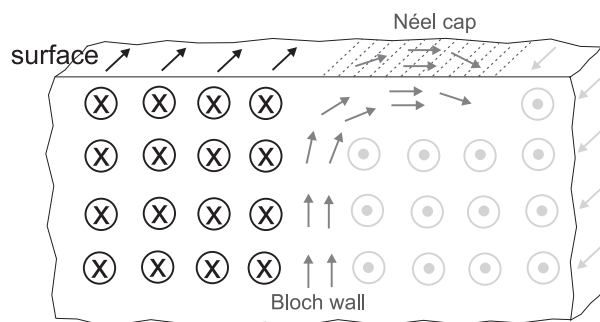
Figure 2.3: Schematic representation of the transition between a bulk Bloch wall and a surface Néel wall. The Bloch wall is running vertically through the center of the image and is terminated into a Néel cap at the surface. Crosses and dots correspond to magnetization vectors pointing in and out of the image plane.

surface can turn over from a rotation parallel to the plane of the domain wall to a rotation perpendicular to it. In other words, to reduce the magnetic charges a bulk Bloch wall can terminate in a Néel wall at the sample surface [49]. Fig. 2.3 shows a schematic sketch where a Bloch wall is transformed into a Néel wall at the surface.

Domains in antiferromagnets are defined as areas showing the same order of magnetic moments. In ferromagnets the driving force for creating domains is the stray field. Due to the absence of macroscopic stray fields in antiferromagnets, other mechanisms have to be responsible for the formation of domains. Perturbations of the regular arrangement of the crystal lattice may disturb the antiferromagnetic order. Recently, antiferromagnetic domains were imaged on $LaFeO_3$ [50, 51] showing that the domain structure can be correlated to areas of different crystallographic order (crystallographic domains). In a different work, antiferromagnetic domains were imaged in NiO single crystals. In this case, the formation of domains is attributed to magneto elastic effects [52–54].

Locale defects in a crystal, e.g. screw dislocations, can cause the formation of domains [5]. As shown in the present work, another defect, i.e. monatomic steps at an interface between a ferromagnetic substrate and an antiferromagnetic film, also lead to the formation of domains in the antiferromagnet.

## 2.1.2 Exchange coupled systems: an uncompensated antiferromagnet in contact to a ferromagnet

A ferromagnet in direct contact to an antiferromagnet is called an exchange coupled system. In the following, we will only consider uncompensated antiferromagnets of such an exchange coupled system. Complex effects can occur caused by the exchange interaction at the interface between a ferromagnet and an antiferromagnet. The most common structural defects at the interface are monatomic steps. When a layer-wise antiferromagnetic film is overgrowing monatomic steps of a ferromagnetic
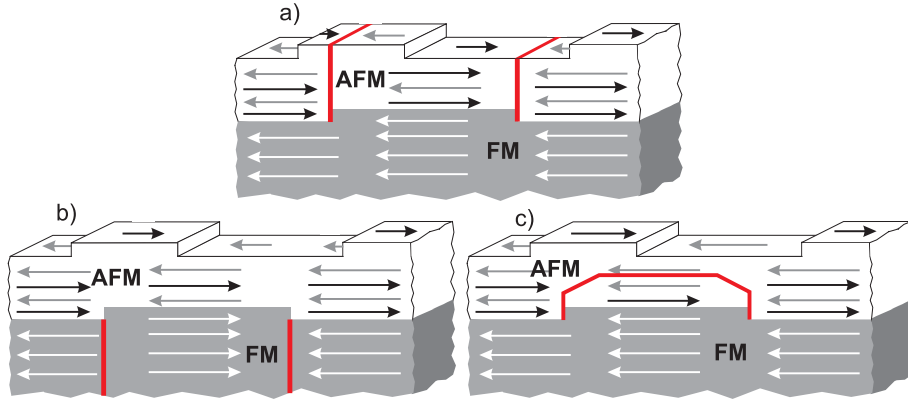
Figure 2.4: Three possible structures of magnetic frustrations caused by monatomic steps at the interface between a layer-wise antiferromagnet and a ferromagnet. In a) the magnetic frustration is formed throughout the antiferromagnetic film above the buried substrate steps and in b) the frustration is formed in the substrate. c) shows the possibility of forming a closed magnetic frustration within the antiferromagnetic layer connecting two frustrated regions. This frustration could also be formed at the interface or in the substrate.

substrate, a difference in the thickness of one atomic layer between both sides of the steps is created in the film. In the case of collinear coupling between the antiferromagnet and the ferromagnet, it is not possible to keep for all nearest neighbors the ferromagnetic order in the ferromagnet, the antiferromagnetic order in the antiferromagnet, and the same magnetic order at the interface. This conflict in the magnetic order leads to a magnetic frustration. Three possible configurations for a magnetic frustration are illustrated in Fig. 2.4. In the configuration of Fig. 2.4a) and b) either the antiferromagnet or the ferromagnet is split into two domains at each position of an interface step. The magnetic frustration starts at the step edges and is located above or below them throughout the film. In the third case (Fig. 2.4c), a magnetic defect line is formed parallel to the interface connecting two frustrations at interface steps. The wall can either lie in the ferromagnet or the antiferromagnet or at the interface. The region of magnetic frustration caused by such defect lines is often described as a domain wall caused by a frustration [55–57]. Close to the topological defect, the magnetically frustrated region cannot be described by a competition between the exchange and the anisotropy energy as in the case of conventional domain walls in ferromagnets and antiferromagnets (section 2.1.1). The magnetic frustration is pinned at this topological perturbation. The main focus of this work lies on the investigation of magnetic frustrations in thin antiferromagnetic films caused by monatomic steps at the interface in an exchange coupled system. In the following, an overview of models and calculations performed on these kind of magnetic frustrations is given.

Berger and coworkers [56] performed calculations of a model system consisting of

a ferromagnetic film on top of a bulk antiferromagnet having two monatomic steps at the interface. Note that this is the reversed situation compared to the one shown in Fig. 2.4. They found the three phases of wall states illustrated in the figure. In their calculations, it was demonstrated that the stability of each phase depends on the over-layer thickness, the defect density, the strength of the exchange coupling and the temperature [56]. In the special case that the temperature is well below $T_C$ and $T_N$ and in the limit of low step density, it is energetically more favorable to form magnetic frustrations in the thin over-layer (case Fig. 2.4a)). In the case of a high step density at the interface, magnetic frustrations can be connected to reduce the length of the magnetic frustration and thus the energy of the system, as illustrated in Fig. 2.4c) [58].

Morosov and coworkers [57, 59] performed calculations for a thin antiferromagnetic film on top of a much thicker ferromagnetic substrate having monatomic steps at the interface. Their calculations show the formation of a wall in the thin film separating it into domains of opposite magnetization directions. This behavior was observed assuming similar conditions as used by Berger and coworkers [56] for the case that the magnetic frustration was formed in the thin over-layer. Their calculations correspond to the case presented in Fig. 2.4a). For such a situation, it was shown that the main rotation of spins occurs in the thin film and that only a small tilt of the spins is present in the ferromagnetic substrate. In the limit of thin films, the width of the created magnetic frustration was found to be smaller than the width of conventional domain walls and it is mainly determined by a competition between different exchange interactions in the ferromagnetic-antiferromagnetic system [57, 59].

The most frequently studied system in this context is Cr on Fe [55, 60–63]. Stoeffler and coworkers [62, 63] studied the magnetic behavior of Cr atoms on a stepped Fe substrate. Thin Cr films on Fe (001) show a layer-wise antiferromagnet coupling [44, 45]. Therefore, this system is a realization of the model described in Fig. 2.4. The calculations show the formation of a magnetic frustration in the form of a defect line separating two Cr domains of opposite magnetization at the position of the Fe substrate step, corresponding to the case a) in Fig. 2.4. The calculations indicate a rotation and a change of the size of the magnetic moments in the antiferromagnetic film above an Fe step edge. Also a tilt of the magnetic moments of the underlying Fe substrate in the vicinity of the step edge was found. The magnetically frustrated region increases in width with increasing the Cr thickness. The lateral extension of the magnetic frustration is rather small, only extended over some atoms, and localized in the vicinity of the Fe step. The magnetic configuration at the surface reflects the roughness of the Cr surface and the interface roughness between Cr and Fe. As we will see later, the behavior of the magnetic frustration theoretically predicted for the system Cr on Fe is found experimentally for a similar system, layer-wise antiferromagnetic ordered Mn films on Fe(001).

## 2.2   Tunneling and scanning tunneling microscopy

Since the development of quantum mechanics in the 1920s, it is known that a particle with a kinetic energy smaller than the potential energy of a barrier has a non-vanishing probability to enter the barrier. In the case of a finite potential barrier (height and width), the particle can tunnel from one side of the barrier to the other one. When the tunneling particles are charged, e.g. electrons, this results in a so-called tunneling current. In a one dimensional model with a rectangular potential barrier ($V_B$) and for free electrons with a kinetic energy $E < V_B$ the solution of the Schrödinger equation gives a simple correlation between the tunneling current and the barrier width ($d$):

$$I \propto e^{-2kd} \tag{2.5}$$

with the wave vector $k = \sqrt{2m(V_B - E)}/\hbar$. Here, $m$ is the electron mass, and $\hbar$ the Planck constant divided by $2\pi$. As a result, the tunneling current decays exponentially with increasing barrier width due to the exponential decay of the probability density of the electrons in the barrier. The tunneling probability from each side of the barrier to the opposite side is the same. Therefore, the resulting tunneling current is zero. When a voltage is applied over a barrier (between two electrodes) their Fermi energies are shifted with respect to each other and a net tunneling current flows. In materials, a barrier exists which electrons need to overcome to enter the vacuum. It is the energetic difference between the bound states and states in the vacuum and is called work-function.

The high sensitivity of the tunneling current on the distance is used in scanning tunneling microscopy (STM). There, one electrode is replaced by a conducting tip which is scanned over a sample surface, while the local tunneling current between the tip and the sample is measured. For this geometry and assuming the simple equation 2.5, one expects that electrons with a wave vector perpendicular to the sample surface yields the highest tunneling probability, while electrons with a component parallel to the surface have to travel a longer distance d which results in a reduced tunneling probability.

Typically, the work-function in metals have values of $4 - 5$ eV. Assuming the simple equation 2.5 and considering usual conditions of a STM experiment, a drop of the tunneling current by about one order of magnitude for every 1 Å of vacuum between the electrodes occurs.

The analysis of the local tunneling current in STM measurements opened the possibility to image electronic structures on a surface at the atomic scale [26]. The precise lateral and vertical movement of the tip during the scanning process in STM measurements is controlled by piezoelectrical crystals. These piezos change their length when a voltage is applied and the elongation can be precisely varied in the sub-angstrom range. The most common mode for performing STM measurements is the constant current mode (Fig. 2.5). In this case, the tip is stabilized at a fixed voltage (of the order of 1 V) applied between tip and sample and a fixed tunneling current (typically of the order of 1 nA) above the sample surface. Holding the
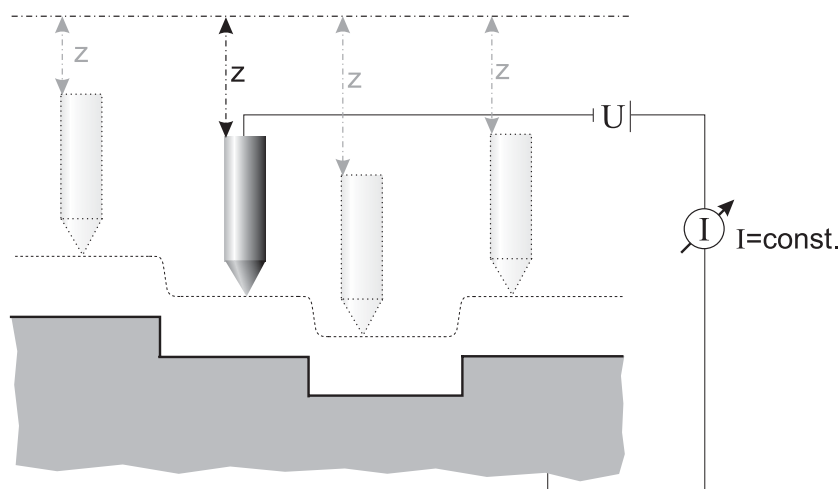
Figure 2.5: Schematic drawing of a STM working in a constant current mode. While the tip is scanned over the sample surface, the tunneling current is kept constant by changing the vertical position of the tip (indicated by the length z).

tunneling current and the bias voltage constant the tip is scanned over the sample surface while the vertical position of the tip is adjusted by a piezoelectrical feedback mechanism. Thus, the tip is following the contour lines of constant tunneling current, as indicated by the dashed line in Fig. 2.5. By detecting the vertical motion of the piezo, a contour map of the constant tunneling current of a sample surface is obtained. For details see for example Ref. [64]

To describe the features visible in STM images, the transmission probability between the tip and the sample has to be known. This requires the knowledge of the atomic structure of the tip and the sample surface. One of the notorious problems is the unknown and noncontrollable detailed arrangement of the atoms at the end of a STM tip. In the approach of Tersoff and Hamann [65, 66], the atomistic arrangement of the atoms at the tip apex is assumed to be spherical and characterized by a spherical potential well. The electronic structure of the tip is considered to be constant and described by a s-orbital. Using these simplifications, they found that the tunneling current is proportional to the density of states of the sample at the position of the tip apex which is described by the center of the sphere $\vec{R}$. Thus, in this model STM images present only properties of the sample surface. In the limit of small voltages ($eV \ll \phi$, with $\phi$ being the work-function) the tunneling current ($I$) can be written as:

$$I \propto eV n^s(\vec{R}, E_F) \tag{2.6}$$

where $n^s(\vec{R}, E_F)$ is the local density of states of the sample surface at the position $\vec{R}$. $n^s(\vec{R}, E_F)$ includes the wave function of the sample at the position $\vec{R}$ and the exponential decay of the wave function within the vacuum gap. In this description, an image of constant tunneling current presents a plane of constant local density

of states of the sample surface. In this case and a homogeneous sample, in first approximation constant tunneling current images reflect the topography of a sample surface.

In the Tersoff and Hamann model, the lateral resolution of the STM ($\delta$) is determined by the radius of the sphere placed at the tip apex, the distance between tip and sample ($d$), and the wave vector of the tunneling electrons, $\delta = [2k^{-1}(R+d)]^{1/2}$ [65]. As a result, the measured structure ($w_{exp}$) can be treated as a superposition of two Gaussian functions consisting of the local expansion of the surface structure ($w_s$) and the resolution of the STM tip $w_{exp} = \sqrt{w_s^2 + \delta^2}$. Since the tip apex is always finite and cannot be smaller than one atom, monatomic steps can never be imaged atomically sharp, as indicated in Fig. 2.5.

In scanning tunneling spectroscopy (STS) measurements, the tip is scanned over the sample surface (as in normal STM measurements) and at each scanning position, the tip to sample distance is fixed for a short moment while the bias voltage is ramped. Therefore, variations of the tunneling current as a function of the bias voltage ($U$) are measured, resulting in $I/U$ spectra of each spatial point. Within the simple Tersoff and Hamann model, the differential conductivity $dI/dU$ is directly proportional to the local density of states of the sample surface. One possibility to measure directly $dI/dU$ spectra is to apply a small alternating voltage on top of the ramped bias voltage. By detecting variations of $dI/dU$ as a function of the bias voltage, the local electronic properties can be observed. Thus, the dispersion of bulk states, resonances and surface states can be visualized [67]. Surface states are characterized by spatial localization of electron states at the surface. The bands of surface states are placed in the energy gap of bulk bands. If a band of a surface state is overlapping with a bulk band, the resulting state is called resonance due to imperfect localization at the surface [68].

The simple interpretation of treating the STM images as the topography of the sample surface has to be taken with caution. The tunneling current depends in a complex way on the electronic structure which is especially important on the atomic scale. In the nanometer range or at larger scales, however, the interpretation of STM images as the topography can be a good approximation. An overview of the interpretation of STM images based on the above mentioned theory is given in Ref [69].

A more complete model of STM images, including the dependence of changes of the tunneling current with the bias voltage, requires a complete description of the electronic structure of the sample, the tip and the coupling between them through the vacuum gap. The Landauer-Büttiker theory [70], which is introduced in the context of spin-polarized tunneling in the following section, is one step in this direction.
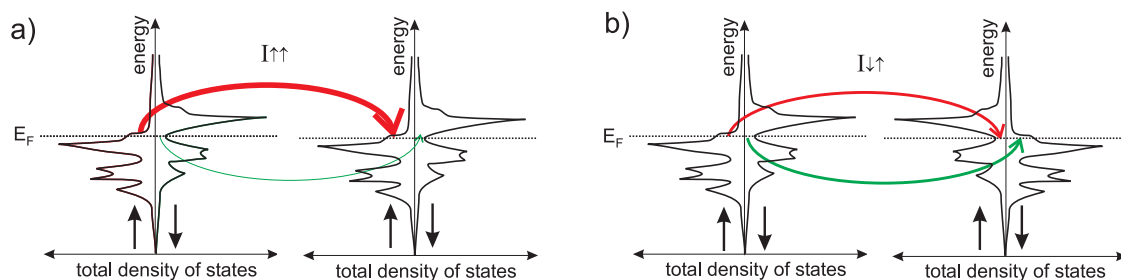
Figure 2.6: Simple illustration of the origin of the spin-dependent tunneling current on the example of the bcc Fe spin-dependent density of states in the limit of small bias voltages. a) and b) show the case of parallel and antiparallel alignment of the magnetization of two Fe electrodes, respectively.

## 2.3 Spin-polarized scanning tunneling microscopy

First experiments on spin polarized tunneling where performed by spin-polarized field emission of electrons emitted from a magnetic tip [71,72]. In these experiments, a high negative voltage is applied to a sharp tip. The spin direction of the emitted electrons reflects the spin polarization of the material under investigation.

In 1975 Jullière discovered that the tunneling current between two ferromagnetic electrodes separated by an insulator depends on the relative orientation of the magnetization of both electrodes [28]. This effect is known as the tunneling magnetoresistance effect. In this experiment, one has to take into account not only the spin dependence of the occupied states in one electrode, as in the field emission experiments but also the one of the unoccupied states in the second electrode. Jullière proposed an explanation of his experimental result based on the spin polarization of the conduction electrons in both ferromagnetic electrodes. In his model, he assumed that the tunneling probability from any occupied state of one electrode to any unoccupied state in the other electrode is the same and that the tunneling current is independent of the geometry and the electronic structure of the barrier. Further assumptions are the conservation of the electron spin during the tunneling process, zero temperature (T=0 K), and a small external voltage. Under these conditions, the spin-dependent tunneling process can be explained by the difference in the spin-dependent densities of states at the Fermi energy. As already mentioned in section 2.1, the electron density in ferromagnetic materials at the Fermi energy is dominated by electrons with one particular spin direction resulting in a spin polarization close to the Fermi energy. Fig. 2.6 shows the spin-resolved density of states for two bcc Fe electrodes [42] having parallel (a)) or antiparallel (b)) alignment of their magnetization directions. At the Fermi energy there are more occupied and unoccupied states of majority than of minority character. The spin polarization close to the Fermi energy in Fe is about 35% [73]. In the case of parallel alignment of the magnetization of two Fe-electrodes, majority electrons from one electrode can tunnel into empty majority states of the other electrode and in an analogue way

minority electrons into minority states. If the magnetization direction of both Fe electrodes is aligned antiparallel, electrons having the same spin direction are of majority character in one electrode and of minority character in the other electrode. Because the electron spin is assumed to be conserved during tunneling, a different tunneling current flows for parallel and antiparallel alignment of the magnetization directions of the two Fe electrodes. Though, many simplifications are included in this model, it leads to a qualitative description of the spin-polarized tunneling process.

A more elaborate model by Slonczewski [74] shows that the tunneling current does not only depend on the properties of the ferromagnetic electrodes but as well on the electronic structure of the tunneling barrier. He analyzed the tunneling current through a rectangular barrier by assuming that the tunneling electrons in the two ferromagnets are free electrons. Therefore, he described the ferromagnets by two simple parabolic bands (one for spin up and one for spin down) which are split by the exchange splitting. Further assumptions included in his model are zero temperature (T=0K), vanishing external voltage, and that mainly electrons with a wave vector perpendicular to the plane of the tunneling contact contribute to the tunneling process. The resulting equation for the spin-dependent tunneling current is given by:

$$I = I_0(1 + P_1 P_2 \cos \Theta), \tag{2.7}$$

where $I_0$ presents the tunneling current without spin polarization of the electrodes, $P_{1,2}$ is the effective spin polarization, and $\Theta$ is the angle between the magnetization directions of both ferromagnetic electrodes. The effective spin polarization is given by

$$P_{1,2} = \frac{k_{1,2}^\uparrow - k_{1,2}^\downarrow}{k_{1,2}^\uparrow + k_{1,2}^\downarrow} \cdot \frac{\kappa^2 - k_{1,2}^\uparrow k_{1,2}^\downarrow}{\kappa^2 + k_{1,2}^\uparrow k_{1,2}^\downarrow}. \tag{2.8}$$

Here, $\kappa$ is the wave vector in the barrier[1] and $k_{1,2}^\uparrow, k_{1,2}^\downarrow$ are wave vectors of majority and minority electrons at the Fermi energy. In the free-electron model, $k^{\uparrow,(\downarrow)} \propto D^{\uparrow,(\downarrow)}(E_F)$ with $D(E_F)$ density of states at the Fermi energy. The first term of the effective spin polarization in equation 2.8 contains only the polarization of the two ferromagnetic electrodes as introduced by Jullière. The second term can be treated as a correction term which contains the barrier height. For high barriers ($\kappa^2 \gg k_{1,2}^\uparrow k_{1,2}^\downarrow$), the value of the effective polarization reduces to Jullière's result [75]. Slonczewski's model shows that the tunneling current depends on the type of the tunneling barrier which therefore plays an important role in the tunneling process.

Recently, it was possible to describe tunneling processes by ab-initio calculations which are based on the Landauer-Büttiker formalism [76]. The Landauer-Büttiker theory [70] is an elastic and ballistic transport theory in which two electrodes and a tunneling barrier are considered. Here, elastic means that the energy of the electrons is conserved and ballistic transport that the phase coherence of the electrons is maintained from the point when they entering the tunnel system until they leave it.

---

[1]$\kappa\hbar = [2m(E_F - V_B)]^{1/2}$.

In this case, the tunneling is described by the transmission probability of electrons, considered as Bloch waves which are passing the whole tunnel system. The tunneling current ($I$) is expressed by:

$$I \propto T(E), \tag{2.9}$$

where the transmission $T$ depends on details of the electronic structure of the tunneling system, e.g. the dispersion relation ($E(k)$) and the barrier properties. The Slonczewski model is a special case of the Landauer-Büttiker theory, in which the realistic band structure is replaced with a free electron band. The consideration of realistic band structures, obtained by ab-initio calculations and included in the Landauer-Büttiker theory, shows that the band gaps have a pronounced influence on the tunneling current. Thus, the different matching between the electronic states plays an essential role. However, a direct consequence of this transport approach is that localized states, e.g. surface states cannot contribute to the tunneling current because they are placed in energy band gaps of the bulk states and they have only a wave vector parallel to the sample surface. In contrast to surface states, resonances can couple to the bulk states and they can produce a strong enhancement of the tunneling current. Using the above introduced theory, the spin-dependent tunneling current through various tunnel systems has been calculated recently [77–82].

In Sp-STM measurements, the spin-dependent tunneling current is used to investigate the spin polarization of a sample surface in addition to the topography. The spin polarization gives information of the local magnetization of a sample surface. In a Sp-STM, the two ferromagnetic electrodes are replaced by a ferromagnetic STM electrode (tip or ring, as shown later) and a ferromagnetic sample and the vacuum between Sp-STM electrode and sample plays the role of the insulator [4]. As shown in equation 2.7, the spin-polarized tunneling current depends on the angle $\theta$ between both magnetization directions. Switching the magnetization ($M$) of the electrode from $M$ to $-M$ corresponds to a change of the angle from $\theta$ to $\theta + 180°$. One can easily see that the average of the two spin depended tunneling currents reduces to $\bar{I} = I_0$. Therefore, the average tunneling current (averaged over the opposite alignment of the magnetized directions) is independent of the spin polarization and yields the topographic information like in the case a non magnetic electrode is used. However, the difference of these two spin-dependent tunneling currents is proportional to the spin polarization, $\Delta I = 2I_0 P_1 P_2 \cos \Theta$.

The magnetization direction of the Sp-STM electrode defines the direction of sensitivity and hence the direction of the imaged component of the spin polarization of the sample surface (Fig. 2.7). Performing constant tunneling current STM measurements and using ferromagnetic STM electrodes which are magnetized in one direction, changes of the spin-polarized tunneling current will change the distance between electrode and sample surface. This is because the feedback mechanism will adjust the vertical position of the electrode to keep the tunneling current constant. A change of the spin polarization is only visible in the form of an additional topographic contrast in the STM image [30]. When the magnetization of the electrode is switched with a frequency much higher than the frequency of the feedback mecha-
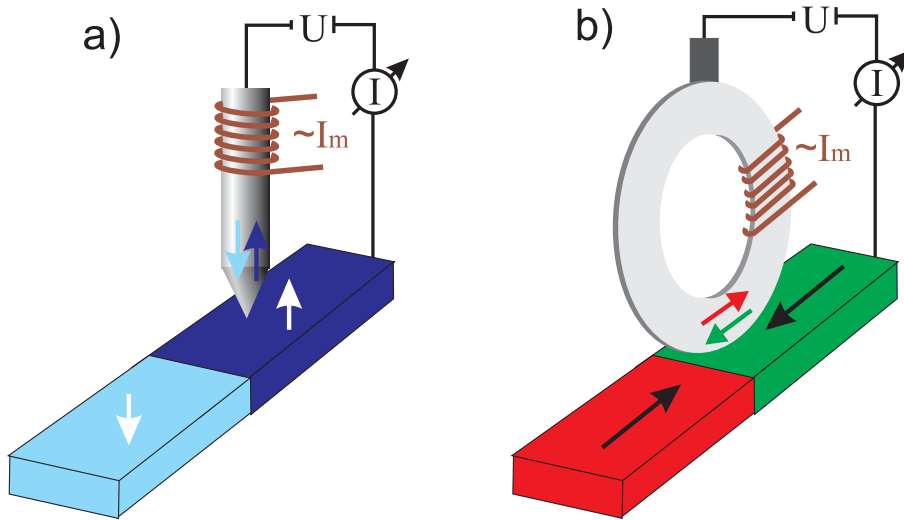
Figure 2.7: Schematic representation of Sp-STM electrodes, a) for measuring the out-of-plane [4] and b) the in-plane component [7].

nism, no changes of the distance occurs as the changes of the spin-polarized tunneling current are averaged out. Therefore, one can separate an average tunneling current $\bar{I}$ which gives topographic information from the modulated current $\Delta I$ that results from the spin-polarized tunneling current and yields the spin information.

In our experiment, the magnetization of a ferromagnetic STM electrode is switched by applying a small alternating current to a coil wound around the electrode. This is schematically shown in Fig. 2.7. The alternating magnetic field induced within the coil is large enough to fully reverse the magnetization of the electrode. Details of the experimental realization are described in section 3.1.1.

To measure the magnetic out-of-plane component, a sharp ferromagnetic tip is used. Using the above described technique, the out-of-plane magnetization component was imaged for the first time in 1998. A high lateral resolution of at least 1 nm has been achieved [35]. Because of the elongated shape of a sharp tip, it has a large shape anisotropy resulting in a magnetization direction collinear to the axis of the tip. The sharper the tip the smaller the amount of magnetic material close to the sample and hence the smaller the stray field which may influence the magnetization of a sample [83]. Fig. 2.7a) shows a schematic drawing of the out-of-plane setup.

In this work, the concept of the Sp-STM is expanded by the capability to image a well-defined in-plane component. To investigate the in-plane spin polarization of a sample surface a Sp-STM electrode is needed having a magnetization direction in the plane of a sample surface at its apex. Because of the above mentioned reason it is difficult to achieve in-plane sensitivity using a conventional sharp tip. One solution is to use a ferromagnetic ring (Fig. 2.7b)) as a Sp-STM electrode. Here, the magnetization direction lies always tangential to the outer perimeter of a ring. Thus, at the bottom of the ring where the tunneling occurs, the magnetization lies

in the plane of the sample surface. Because the magnetic flux in an ideal ring is closed, the magnetic stray field is zero. Therefore, ideal rings have no influence on the magnetization of the sample. By choosing the plane in which the ring is oriented, the magnetization direction of the ring is defined and thus the direction of the sensitivity in the surface plane for the measured spin signal is known as well. One may wonder if such macroscopic rings used as a STM electrode will not significantly decrease the lateral resolution. As it will be shown later, the rings are not perfectly smooth and nano tips exist at the apex which can give a high lateral resolution.

Besides the imaging of magnetic structures, Sp-STM measurements allow the investigation of the spin-dependent tunneling current through a well-defined tunneling barrier (vacuum gap). Under these well-defined conditions, one typical experimental difficulty of a structured three layer system, the undefined interfaces and thus complicated potential barriers, is avoided [80]. The size and sign of the spin-dependent tunneling current as a function of the bias voltage gives information of differences in the spin polarization close to the Fermi energy. Therefore, spin-polarized spectroscopic details can be obtained.

An other possibility to image the spin polarization of a sample surface by STM is to perform STS measurements [3]. In this case, non magnetic metal tips, e.g. W-tips, are coated with ferromagnetic or antiferromagnetic materials. Here, the magnetization of the tip is not switched during the measurements. Depending on the tip material and the material deposited on its apex, magnetic sensitivity is achieved for the in-plane or out-of-plane component [84]. Performing STS measurements $dI/dU$ spectra are recorded and changes of the relative orientation between tip and sample magnetization may cause changes in the $dI/dU$ spectra. In the case of a homogeneous electronic structure of the sample surface, these changes can be related to variations of the local magnetization at the sample surface. A typical $dI/dU$ spectrum measured on an Fe (001) single crystal is presented in Fig. 2.8a) [1]. The spectra was taken with an Fe-coated W-tip being sensitive to the in-plane component of the spin polarization [3]. The peak in the spectra corresponds to the well known surface state at about 130 meV [85]. The difference in the spectra (solid and dotted lines) is caused by the fact that they were taken on oppositely magnetized domains on the Fe crystal. The largest difference in the $dI/dU$ spectrum appears at the surface state, showing that it is strongly spin-polarized. Taking such $dI/dU$ spectra by spatially scanning over the sample surface, images of one component of the local magnetization can be taken. Fig. 2.8b) presents a Sp-STS image of Fe islands on a pseudomorphic ML of Fe on W(110) [86]. The image shows the in-plane component of the magnetization. The dark and light islands are homogenously magnetized but the magnetization vector points in different directions.

When comparing Sp-STM with Sp-STS both methods have their advantages and their drawbacks. In the case of Sp-STM, changes of the spin polarization can clearly be separated from changes caused by spin-independent variations of the electronic structure. This allows the investigation of the spin polarization of sample surfaces having unknown and inhomogeneous electronic structures. In contrast, Sp-STS data
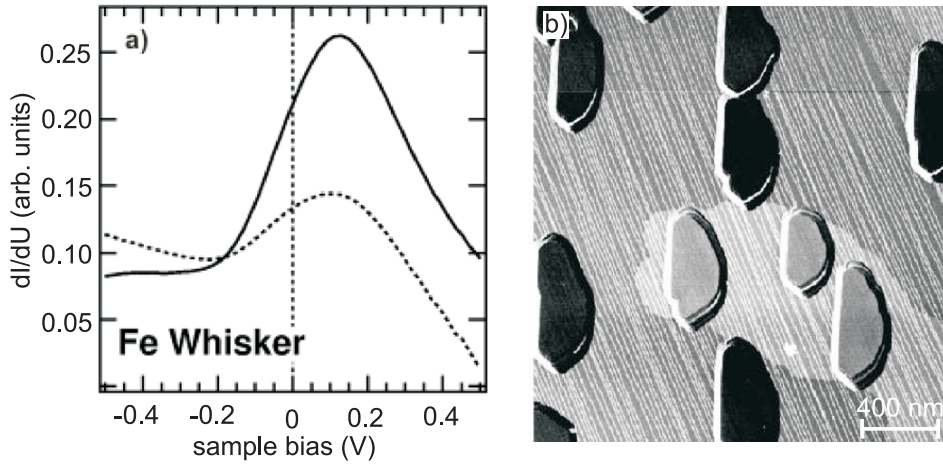
Figure 2.8: a) Sp-STS spectra (solid and dotted line) obtained on a clean Fe(001) surface by Yamasaki and coworkers [1]. The difference is caused by measuring on oppositely magnetized Fe domains. b) Sp-STS image of Fe islands on W(110) where each island is homogenously magnetized, but showing different orientations of their magnetization directions (black and gray islands), obtained by Bode and coworkers [86]. The two different gray levels of the surrounding correspond to different magnetization directions, as well. In these works, the in-plane magnetization component was imaged.

can only be interpreted as changes of the spin polarization of the sample surface when a homogenous electronic structure can be assumed. Since in Sp-STS the magnetization at the tip apex is fixed during scanning, the distance between tip and sample changes if the spin polarization of the sample surface changes. This leads to different tunneling conditions on different domains. This method is also only sensitive to variations of the spin-dependent tunneling current as a function of the bias voltage. A constant spin polarization cannot be detected because it would be compensated by changes of the tip to sample distance. In Sp-STM measurements, the distance between tip and sample is not changing on different magnetized domains (because the magnetization of the STM electrode is switched with a frequency that is higher than the frequency of the STM feedback loop), which allows the direct investigation of differences in the spin-polarized tunneling current. Using W-tips coated with an antiferromagnetic material, the magnetic stray field nearly vanishes and Sp-STS measurements can be performed under an applied external magnetic field [84]. This is impossible for higher fields using Sp-STM due to the necessity of switching the magnetization of the Sp-STM electrode. In Sp-STS, the magnetization direction of coated tips lies randomly in the plane of the sample surface whereas a well-defined in-plane component of the sample spin polarization can be imaged with Sp-STM using a ring as a STM electrode. In this work, only Sp-STM measurements were performed.

# Chapter 3

# Experimental techniques

Sp-STM investigations are best performed on well-defined, stable and reproducible surfaces. Thus, all Sp-STM experiments were performed in ultra high vacuum (UHV). The experimental equipment used for the investigations is presented in the following. A detailed description of the performance of the Sp-STM is given including the design of Sp-STM ring electrodes. To test the extension of the Sp-STM to measure a well-defined in-plane component, measurements are shown which were performed on a well-studied system, a 180° domain wall at the surface of Fe-whiskers.

## 3.1  Equipment

The experimental setup is the one that has been used now for several years to measure the out-of-plane component of the spin polarization with the Sp-STM. All Sp-STM measurements were performed in an UHV chamber with a base pressure of $1*10^{-10}$ mbar. The whole equipment consists of a three chamber system (air-lock, load-lock, main chamber) each having its own pumps. They are separated by valves and equipped with a transfer mechanism for samples and electrodes. This allows a transfer of STM-electrodes and samples from ambient conditions into the main chamber within 3 hours without breaking the vacuum. To avoid intense degassing of new samples and electrodes in the main chamber, baking can take place in each of the chambers. Since STM measurements are sensitive to all kind of mechanical vibrations, the whole chamber system sits on a pneumatic suspension system.

The main chamber consists of two parts, the preparation chamber and the STM chamber. The preparation chamber is equipped with a sputtering gun, an Auger electron spectrometer (AES), a low energy electron diffractometer (LEED), evaporators for the deposition of materials, and a Kerr-microscope. Fig. 3.1 shows an image of the whole vacuum system where the main facilities are indicated.

The differentially pumped sputter gun is used to clean sample surfaces by Argon ion bombardment. Surface atoms are removed by the impact of Argon ions having energies between 1 and 3 keV. Because the ion bombardment destroys the crystal
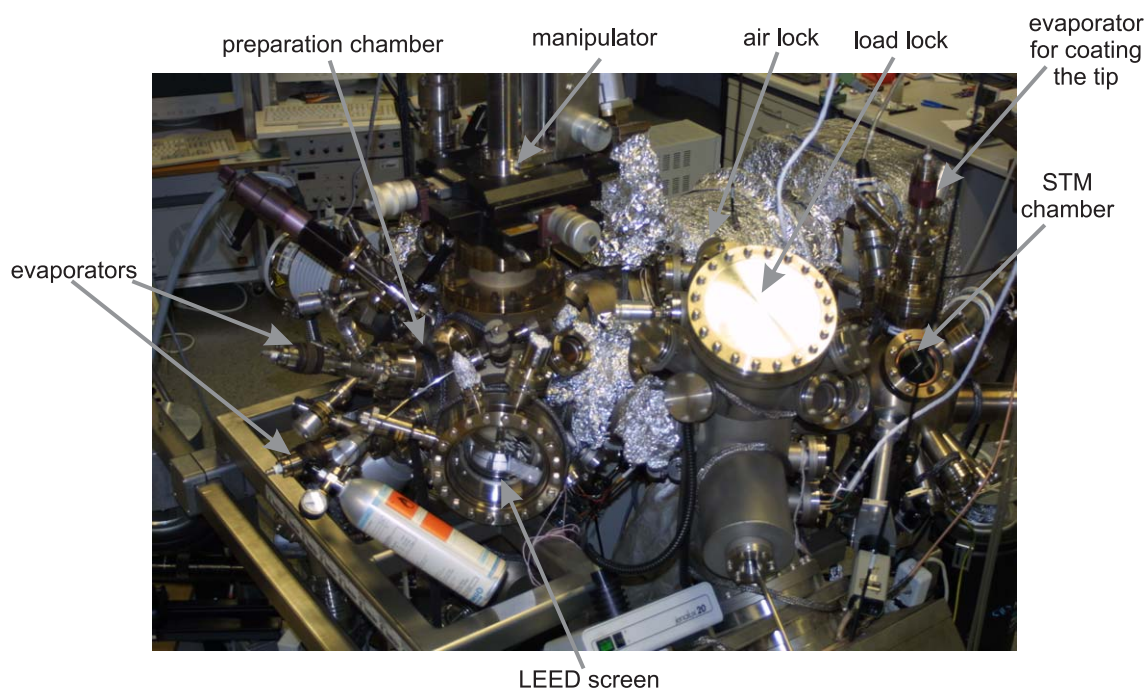
Figure 3.1: Image of the experimental UHV-chambers. The main features are indicated in the image.

lattice structure at the sample surface, the crystals were annealed after sputtering to reduce the induced defects and to release the implanted Ar.

AES allows the characterization of chemical elements at the sample surface. Auger electrons give information of the top most layers, up to about 15 layers depending on the energy of the Auger electrons. The chemical sensitivity is achieved because Auger electron energies are determined by the transition energies between core level electron states which are element specific.

To study the crystalline structure of the sample surface, LEED was used. Because of the low kinetic energy (up to 200 eV) of the incoming electrons the penetration depth without energy loss is only a few atomic layers. In LEED the diffraction of electrons with wave length of a few Å is used to create a diffraction pattern of the two dimensional reciprocal lattice of the sample surface. In the case of a single domain surface this pattern can be transformed into real space showing the unit cell of the crystal structure at the sample surface. LEED is mainly sensitive to periodic structures.

The evaporators are used to thermally evaporate a material onto a substrate by molecular beam epitaxy. This method allows the growth of well-defined films from the sub monolayer range up to nanometer thickness.

The LEED screen and the AES gun are positioned opposite to each other. This configuration is used for medium energy electron diffraction (MEED) measurements where the AES electron gun supplies the medium energy electrons (about 5 keV) and

the diffraction pattern is displayed on the LEED screen. MEED is performed during the evaporation of a material to a substrate. In the case of layer-by-layer growth the amount of deposited material can be determined by ML period oscillations of the diffraction spots.

The Kerr effect exploits the change of polarization of light upon reflection from magnetic surfaces. Linear polarized light can be separated into left and right circular polarized light. The reflection coefficient of magnetic surfaces is different for left and right circular polarized light. It depends on the relative orientation of the magnetization and the electrical polarization[1]. In general, incident linear polarized light is elliptically polarized with a rotated polarization plane after reflected from a magnetic surface. The change of the polarization state of the light is measured by the Kerr-ellipticity and the Kerr-rotation. A Kerr-effect setup consists of a light source, a polarizer, an analyzer, and a detector. In our case, we use light coming from a halogen lamp. The light beam passes a bandpass filter and the polarizer before it is reflected from the surface. The reflected light passes an analyzer and is imaged with a CCD-camera. Kerr measurements were performed in the longitudinal geometry which means that the magnetization of the sample lies in the scattering plane of the light. One can increase the Kerr contrast by calculating the asymmetries[2]. This procedure exploits the fact that the Kerr signal has a reversed sign on both sides of the extinction whereas changes due to the surface topology do not.

### 3.1.1    The spin-polarized scanning tunneling microscope

For the experiments, we used a commercially available Omicron $\mu$-STM [88]. Care was taken to avoid any magnetic material in the sample stage of the STM to exclude an influence on the spin sensitive measurements. The electrical circuit of the Sp-STM is schematically shown in Fig. 3.2. The voltage applied between the sample and the ring is called $U_{gap}$. The measurements were performed in the constant current mode (see section 2.2), where the tunneling current is controlled by the feedback loop with a cut-off frequency $f_{control}$. In this loop, variations of the tunneling current are compensated by changes of the distance between ring and sample by changes of the voltage of the z-piezo. The change of the z-piezo voltage can be recorded which results in the topographic image. With a lock-in amplifier an alternating current of frequency $f_{mod}$ between 15 to 30 kHz is applied to the coil around the ring to switch its magnetization. Because of the dependence of the tunneling current on the relative orientation of the magnetization between the ring and sample this results in a modulation of the tunneling current. By choosing $f_{mod} \gg f_{control}$ the feedback loop collects the average tunneling current. It contains no information on the spin

---

[1]The electrical polarization $Pe_i$ is defined by $Pe_i = \chi_{ij} E_j$ for small electrical fields (E). $\chi$ is the electrical susceptibility. For details see Ref. [87].

[2]For the asymmetry, two Kerr images were taken for analyzer positions on both sides of the extinction (some mrad). The asymmetry is then defined as the difference of the two Kerr images divided by the sum of them.
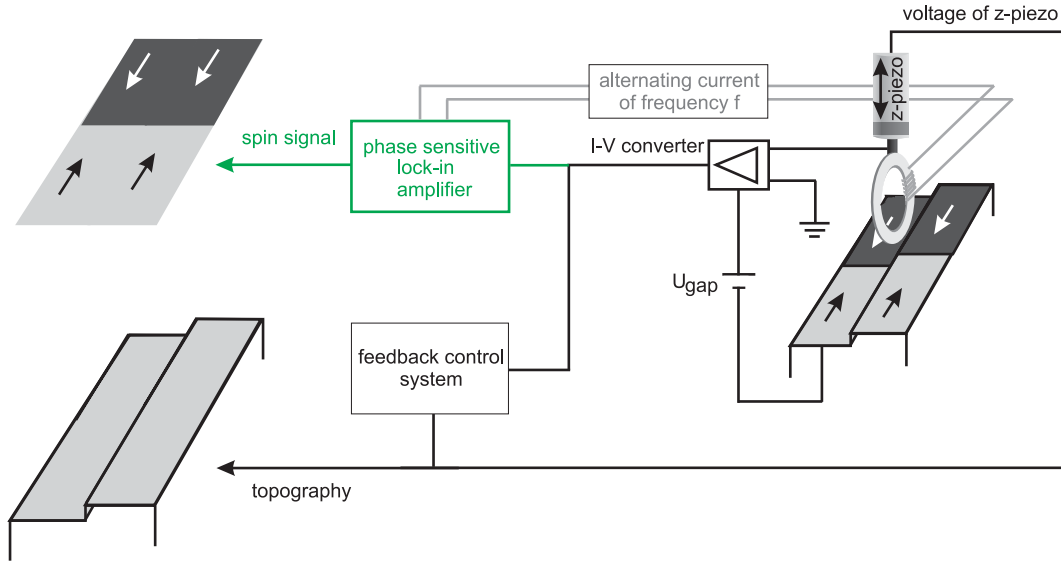
Figure 3.2: Electric circuit of the Sp-STM with the separation of topography and spin signal.

polarization. The modulation of the tunneling current is analyzed with a phase sensitive lock-in amplifier, yielding the spin signal [4].

A sketch of the relation between the switching of the magnetization of the ring, the spin-dependent tunneling current, and the average tunneling current as a function of time is shown in Fig. 3.3. The magnetization of the ring is switched with a constant frequency. The cases a) and b) represent the spin-dependent tunneling current measured on two domains being oppositely magnetized. When the ring is crossing the domain wall, a phase shift of $\pi$ occurs in the spin-dependent tunneling current which means the order between parallel and antiparallel alignment is reversed (the signal in case a) and case b) are phase shifted by $\pi$). If the magnetization of the ring is not completely collinear to the magnetization of the domains, the behavior stays the same but the amplitude $\Delta I$ decreases. By separating $\bar{I}$ and $\Delta I$ and analyzing the latter with respect to the correct phase, the topography and the spin polarization of a sample surface can be imaged at the same time. The spin signal is defined as the spin-polarized tunneling current normalized to the average tunneling current $\Delta I/\bar{I}$. The spin contrast is defined as the difference of the spin signal measured between two neighboring domains normalized to $2\bar{I}$. Because of the processing of the measured signal, the spin signal included in the spin contrast is multiplied by $2\sqrt{2}$ to obtain the true physical quantity of the current asymmetry. This allows the comparison between experimental and theoretical data, as shown later in chapter 5.

In our setup, a sinusoidal alternating current is applied to the coil. Because the phase shift between the applied current and the modulation caused in the tunneling current depends on the frequency and the impedances of all involved components,
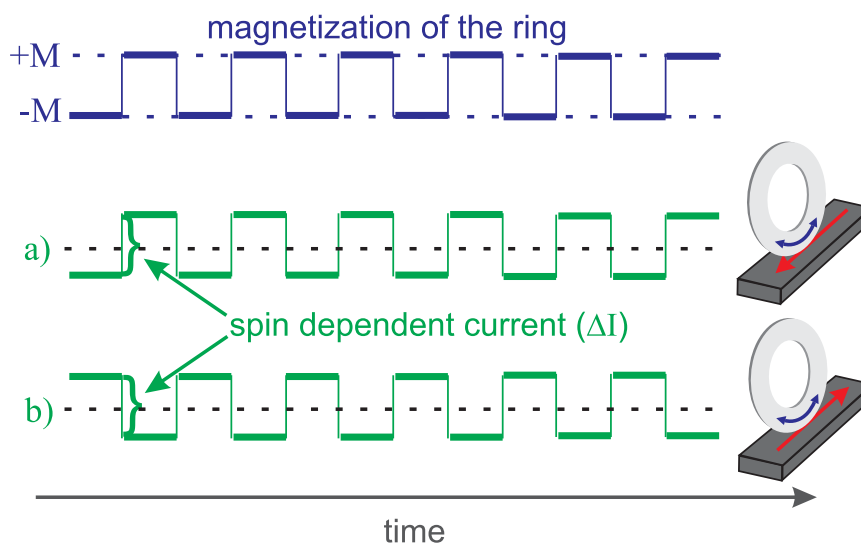
Figure 3.3: Schematic drawing of the relation between the switching of the magnetization of the Sp-STM electrode between the two saturation values $+M$ and $-M$ and the different current contributions. The black dashed lines represent the average tunneling current. Between oppositely magnetized domains, a phase shift of $\pi$ occurs in the spin-dependent tunneling current, represented by case a) and b).

two lock-in signals, signal channel (1) and channel (2) having a phase shift of $\pi/2$, are measured. Therefore, the full information is measured without a-priori knowing the exact phase correlation. The maximal spin signal is given by:

$$\cos\gamma \cdot \text{signal channel(1)} - \sin\gamma \cdot \text{signal channel(2)}, \qquad (3.1)$$

$\gamma$ being the phase. The right phase is found by determining the phase correlation $\gamma$ yielding the minimal spin contrast and calculating the spin signal for $\gamma + 90°$.

Fig. 3.4 shows an image of the Sp-STM. For adjusting the sample and ring position, the STM stage is equipped with three coarse piezos for the lateral movement and one for the vertical. The scanner (Omicron scanner) with the ring on top consists of a piezo tube which controls the precise movement of the ring over the sample surface during the scanning process. To change the ring, the whole scanner is transferred out of the vacuum chamber. In addition to the commercially STM setup, two wires are connected to apply an alternating current to the coil. The STM is placed on Viton O-rings to decouple the STM from mechanical vibrations of the chamber. Additional filters in the electric circuit of the instruments suppress high frequency noise of the power lines.

The lateral calibration of the scanner was performed on the reconstruction of a Au(111) surface. The reconstruction pattern and the distance between corrugation lines was compared with measurements performed by Barth and coworkers [89] and by van Hove and coworkers [90]. The distance between the corrugation lines is 6.3 nm. Fig. 3.5 shows reconstruction patterns imaged after calibration. Clearly
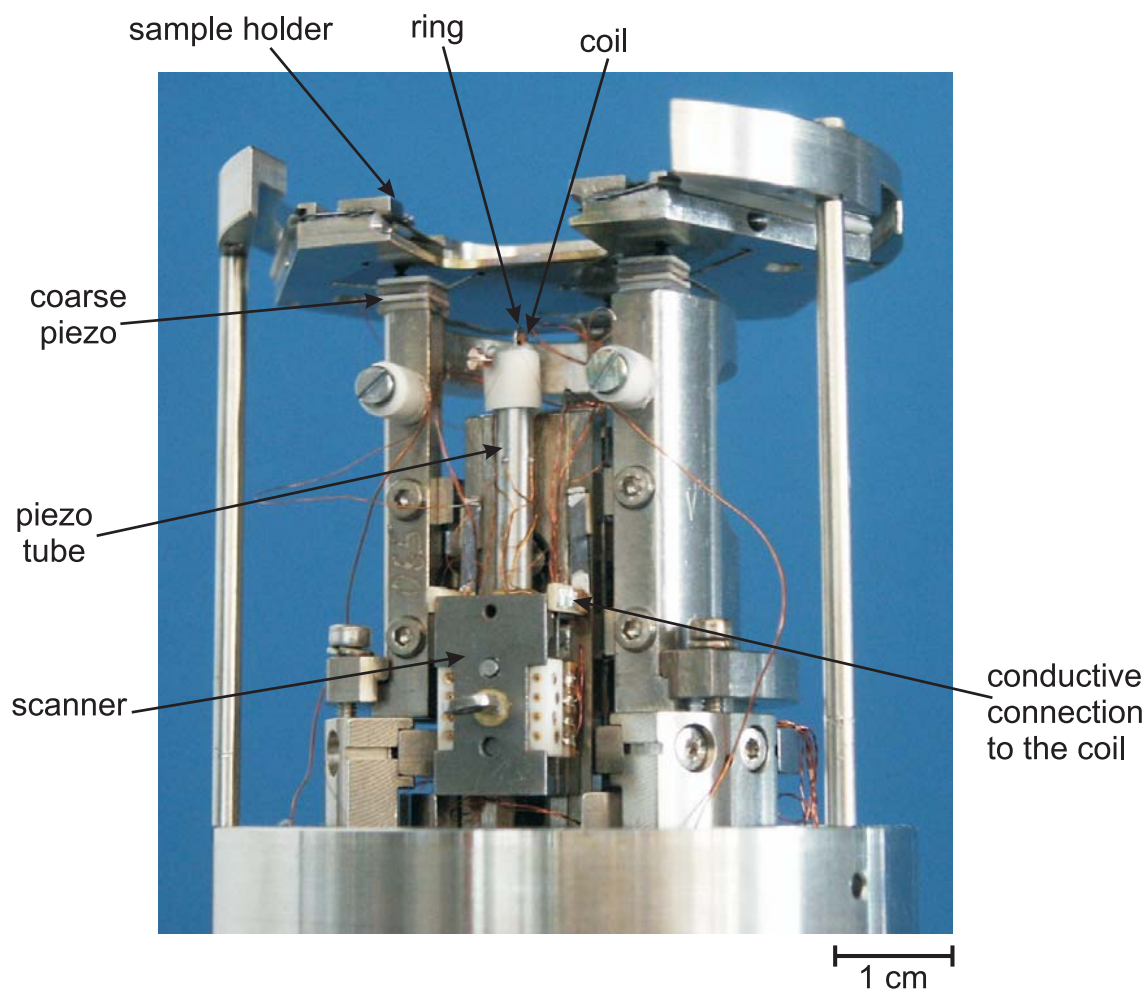
Figure 3.4: Image of the Omicron $\mu$-STM with the modification for Sp-STM measurements.

pairwise arranged corrugation lines of the reconstruction are visible.

## 3.1.2    Preparation of ring electrodes

We use an amorphous alloy of $Co_{68.15}Fe_{4.35}Si_{12.5}B_{15}$ [91] for the Sp-STM electrodes. This material is commercially available. The material has a nearly vanishing magnetostriction $(< 10^{-8})$ [4], which means that nearly no changes of the shape of the material occurs during the magnetization reversal process. This is important to prevent changes of the distance between the electrode and the sample surface during the switching of the magnetization of the electrode. As a rule of thumb, a distance change of 10 pm produces a change of about 20% of the tunneling current[3]. The

---

[3]In first approximation one can assume that the tunneling current depends exponentially on the distance between STM electrode and sample surface [67], see section 2.2.
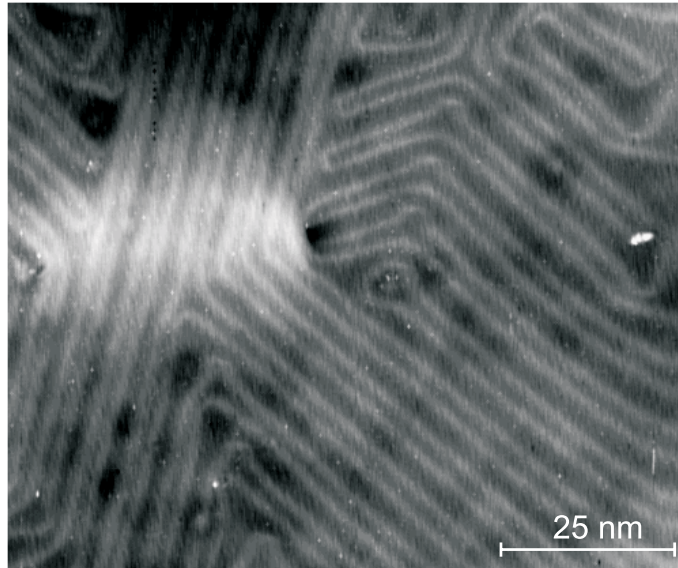
Figure 3.5: Typical reconstruction visible at the Au(111) surface, measured with STM. Pairwise arranged corrugation lines and zigzag patterns of the reconstruction are visible.

material has a low intrinsic coercitivity smaller than 10 $\mu$T. Therefore, only small magnetic fields are needed to switch the electrode magnetization. The low coercivity also results in low magnetic losses which avoids energy dissipation and thus periodic heating and thermal expansion of the electrode. This allows a rapid switching of the magnetization of the electrode without mechanical vibrations.

The rings used as Sp-STM electrodes were electrochemically etched from a foil of 25 $\mu$m thickness. To etch rings, we glued non conducting masks on one side of the CoFeSiB foil. These etching masks had an outer diameter of 2 mm and an inner diameter of 0.7 mm. Onto the other side of the foil, adhesive-tape was fixed. A schema of this preparation setup is shown in Fig. 3.6. The etching solution was a mixture of HF (40%), HCl (32%) and $H_2O$. One electrode was a Pt wire (cathode) and the other one was the CoFeSiB foil (anode). By applying a voltage between these two electrodes, the foil around the ring masks was etched away and rings remained on the adhesive-tape. During the etching process, a current of 40-60 mA was flowing. After etching, the masks and the adhesive-tape were removed with ethanol. The etching procedure alone produces some irregular structures at the outer perimeter of the rings, the part which was later used for scanning. To reduce the roughness, the outer perimeter of the rings was polished. The rings were polished with sand-paper of a grain size of 10 $\mu$m for 5 min, afterwards with a diamond paste, 10 min with a grain size of 6 $\mu$m, 10 min with a grain size of 1 $\mu$m and 5 min with a grain size of 0.25 $\mu$m. After these preparation steps, the rings were annealed in $H_2$ atmosphere to 513 K for 3 h. The ring material cannot be annealed to higher temperatures, because it crystalizes and becomes hard magnetic. Finally, a small
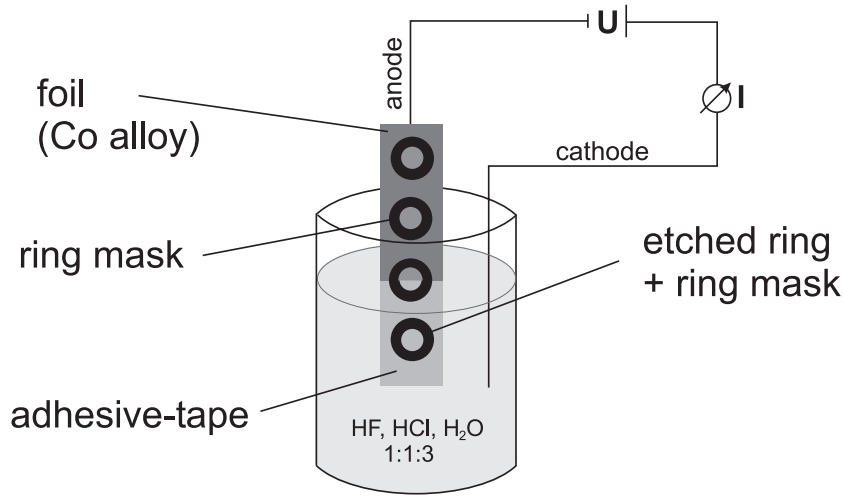
Figure 3.6: Schematic drawing of the electrochemical etching process.

coil of an insolated copper wire of 50 $\mu$m diameter was wound around the ring. The coil was fixed with a non conducting glue to avoid mechanical vibrations. To connect the ring to the STM scanner, a Ta wire was fixed to the ring with a conductive silver glue solution. In Fig. 3.7a) a photo of a ring is shown, as it is used for Sp-STM measurements. One can see the thin ring with a small coil to allow switching of the ring magnetization and the Ta wire for fixing the ring to the scanner. Just for clarification, the rings used as Sp-STM electrodes are macroscopic objects of about 2 mm in diameter and 25 $\mu$m in width. The quality of the outer perimeter of rings prepared as described above were investigated with a scanning electron microscope (SEM). Fig. 3.7b) shows an image of a part of the outer perimeter. Some grooves of some 100 nm in width could be found which originated from polishing. However, they are parallel to the outer perimeter and hence, they should not influence the tangential magnetization. A ring with an outer diameter of 2 mm is not expected to yield a high lateral resolution in STM measurements. Microscopically, there are small protrusions coming from polishing and possibly tips on the nanometer scale. Tunneling from such defects may result in a high lateral resolution. As usually in STM measurements, the exact shape of the tunneling-tip remains unknown. For Sp-STM it is on one hand essential to have a flat ring to ensure that the magnetization in the tunneling region switches in a well-defined way and on the other hand it is important to have not completely flat rings, so that a good lateral resolution is obtained.

The tip apex of a ring can be modified during STM operation by applying a high potential (about 10 V) for a short moment so that a few atoms can move from the surface to the tip apex or the other way round, depending on the sign of the bias voltage. This treatment can form a sharp tip apex. Also, a controlled crash of the tip apex into a sample surface can produce sharp nano tips [64].

To determine the current needed to switch the ring, magneto-optical Kerr-effect
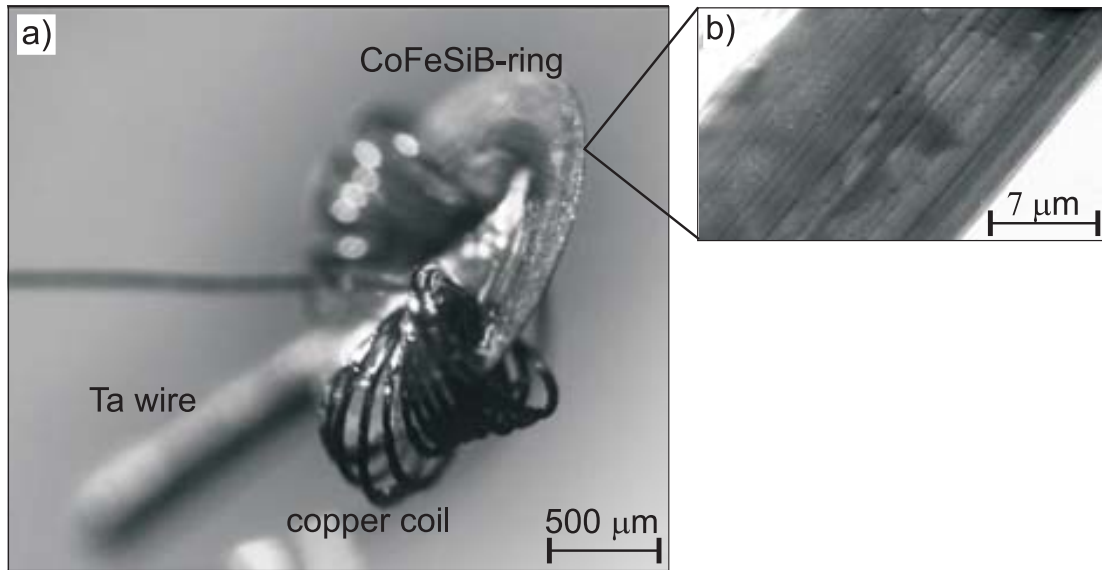
Figure 3.7: a) Optical image of a ring electrode (outer diameter: 2 mm, inner diameter: 0.7 mm) as used for Sp-STM measurements. Also visible are the coil around the ring and a connecting Ta wire. b) SEM image taken at the outer perimeter of a ring where tunneling can occur.

measurements were performed. The Kerr measurements were performed on a single spot on the ring surface. A current was applied to the coil and the ellipticity of the reflected light was measured as a function of this current. Such a Kerr loop is shown in Fig. 3.8. A small current of about 4 mA is sufficient to fully reverse the magnetization of the ring (coil with 20 turns).

After the etched ring was transferred into the vacuum, the outer perimeter, later used for tunneling, was cleaned by Argon sputtering for some hours. Before each measurement, the outer perimeter was always sputtered for some minutes. We figured out that a small amount of Fe deposited on the tunneling part of the outer perimeter improved the contrast in the spin signal. Thus, some Fe, $\approx$10 ML was evaporated on this part of the ring before operating Sp-STM measurements.

## 3.2 In-plane measurements on a test sample: Fe-whisker

We chose Fe-whiskers as test samples since they have been extensively studied in the past and are a well-defined system concerning the domain pattern, the orientation of the magnetization in domains, and the width of domain walls.

Fe-whiskers are Fe single crystal needles of bcc Fe with a lattice constant of 0.287 nm. They are grown from the vapor phase and form needles with a rectangular
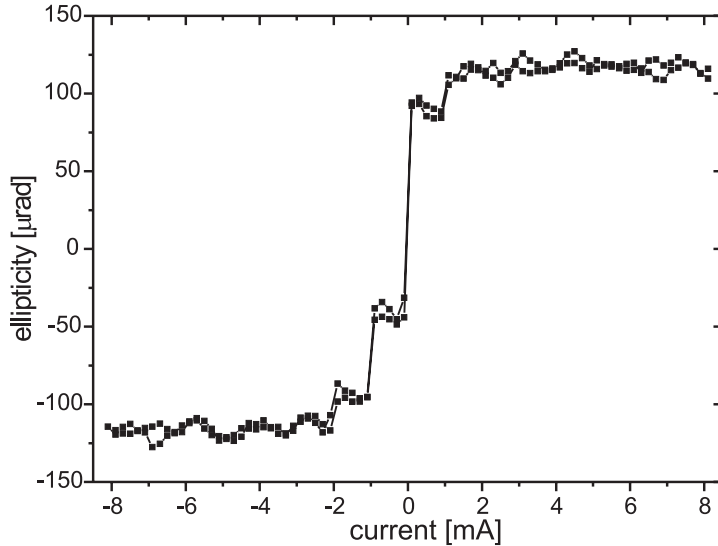
Figure 3.8: Kerr measurement performed on a ring used for Sp-STM measurements. To fully reverse the ring magnetization a current of $\approx 4$ mA is needed for a coil with 20 turns.

cross section and a length of 1 to 2 cm [48]. To illustrate the size and shape of a typical Fe-whisker, an image taken with a scanning electron microscope shows an Fe-whisker together with a fruit fly (Fig. 3.9). Good quality Fe-whiskers have nearly perfectly flat surfaces with terraces of several 100 nm width. The long axis lies along a $\langle 100 \rangle$ crystal axis and the surfaces are formed by (100) planes. A STM image of the topography of an Fe-whisker surface (Fig. 3.9b) shows terraces of 500 nm width. Sometimes defects exist on the surface, and occasionally screw dislocations could be found (Fig. 3.9c)).

The magnetization of Fe-whiskers is in the plane of the surface with easy axes along $\langle 100 \rangle$. Fe-whiskers are magnetically soft meaning the magneto-crystalline anisotropy is much smaller than the stray field energy. Therefore, the domain structure is mainly caused by minimizing the stray field energy. The domain structure of stress free and nearly perfect Fe-whiskers is simple. In the demagnetized state, the sample is subdivided into domains. Typically, the domain pattern consists of a so-called Landau structure, where a 180° domain wall runs parallel to the long axis of the Fe-whisker and end domains which have 90° walls to close the magnetic flux at the surface (Fig. 3.10a)). 180° domain walls always lie along the < 100 > direction and 90° domain walls along the < 110 > direction [48]. In bulk Fe, 180° domain walls are Bloch walls in the volume of the crystal, while at the surface they form Néel caps [93] to minimize the stray field energy at the sample surface. The domain pattern has been extensively investigated with electron microscopy with polarization analysis (SEMPA) [94], Kerr-microscopy [48], and magnetic force microscopy [95].

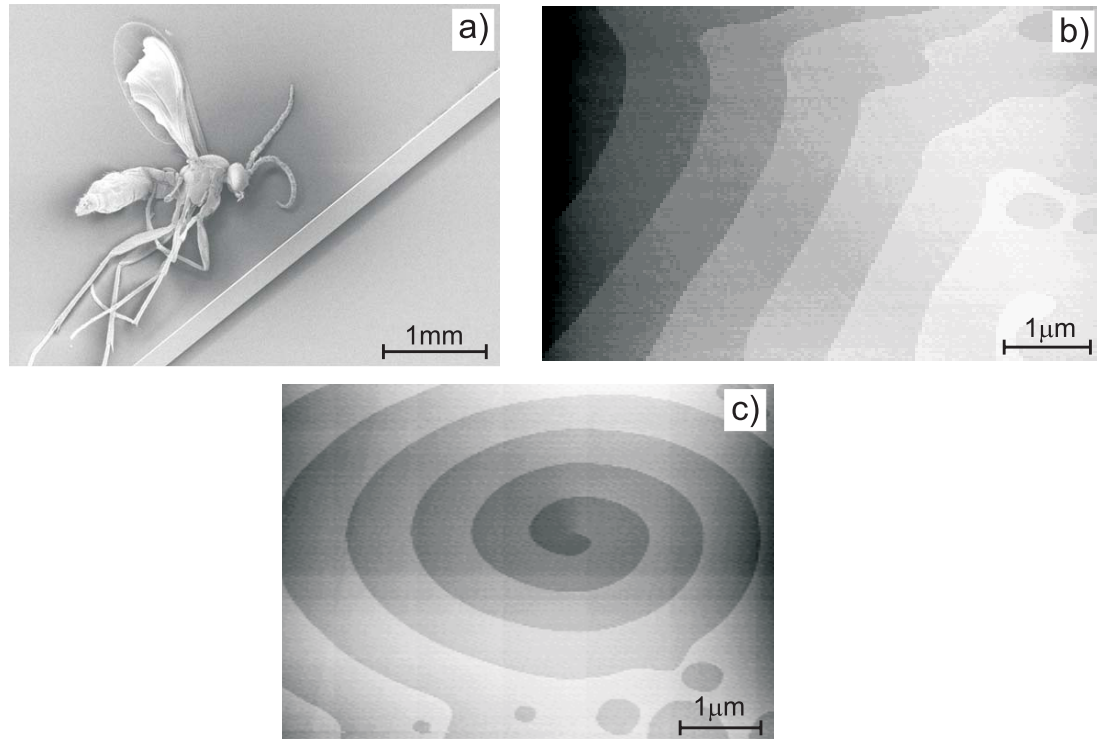180° domain walls of Fe-whiskers easy move in an applied external magnetic

Figure 3.9: a) SEM image of an Fe-whisker. A fruit fly is also shown to illustrate the dimension of Fe-whiskers [92]. b), c) STM images of an Fe-whisker surface. The different gray scales show steps of monatomic height. A flat Fe-whisker surface with a terrace width of about 500 nm is shown in b) and a screw dislocation in c).

field. It was for example shown that an external field of 50 Oe, applied along the easy axis (along the long axis of the Fe-whisker), could move a 180° domain wall of an Fe-whisker (50 $\mu$m width) about 15 $\mu$m [48].

On the one hand, Fe-whiskers have flat and crystalline sample surfaces showing simple domain patterns. These advantages make Fe-whiskers attractive using them as test samples for measuring a well-defined in-plane component with our Sp-STM. On the other hand, they are small which is a problem when fixing them to a sample holder without producing a lot of external stress that modifies their domain pattern.

## 3.2.1   Preparation and characterization of the samples

The Fe-whiskers were cleaned by cycles of Argon sputtering and annealing to 720 K. The kinetic energy of the $Ar^+$ ions was 2 keV and a flux of 0.3 $\mu$A mm$^{-2}$ was measured on the sample plate. The sample surface was controlled with AES and LEED. The magnetic structure of the Fe-whiskers was imaged in situ with a Kerr-microscope. It is not sufficient to check the domain pattern before the Fe-whisker is put into the vacuum chamber, because sputtering and annealing procedures may
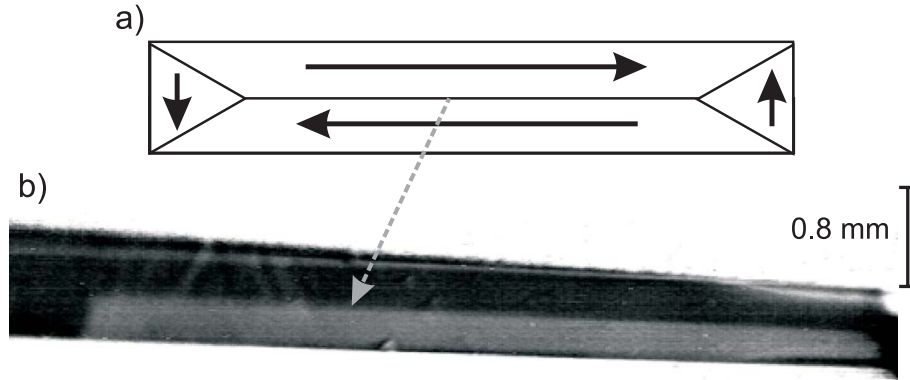
Figure 3.10: a) Schematic representation of a Landau-structure formed to minimize the stray field energy. The black arrows indicate the direction of the magnetization in each domain. b) Kerr-microscopy image of the surface of an Fe-whisker. Two domains are visible separated by a 180° domain wall along the long axis (the grey arrow indicates the correspondence between experiment and scheme). The structures at the ends are caused by stress due to the fixing of the Fe-whisker on a sample holder.

change these patterns.

Fig. 3.10b) shows an image of the domain configuration on a surface of an Fe-whisker taken with a Kerr-microscope. Two domains are visible separated by a 180° domain wall along the long axis. In the following experiments, the Fe-whiskers had such a domain configuration so that the direction of magnetization is well-defined and lies parallel to the long Fe-whisker axis.

## 3.2.2   Imaging of a 180° domain wall on an Fe-whisker

For Sp-STM measurements on Fe-whiskers, the direction of the ring and therefore the direction of spin sensitivity was chosen parallel to the long Fe-whisker axis. In Fig. 3.11a) and b) the topography and the spin signal is visible imaged with the Sp-STM on the surface of an Fe-whisker. The surface shows monatomic steps and terraces of 100 to 200 nm width. The corresponding spin signal in Fig. 3.11b) shows two areas of different spin signal represented as a black and white region. These correspond to two domains separated by a 180° domain wall running along the $\langle 100 \rangle$ direction. The difference in the spin signal between the two domains is 4%. This is a first proof that we are indeed able to image the in-plane spin polarization. In the spin signal, no crosstalk of the topography is seen and in the topography no influence of the magnetic domain wall is found.

Fig. 3.11c) shows a cross section of the calculated magnetic structure for a 180° domain wall in Fe near the surface [96]. The bulk Bloch wall, seen in the lower part of the figure rotates in the plane of the wall and terminates at the surface in a Néel cap. The calculations show that in this particular case the surface Néel wall is about
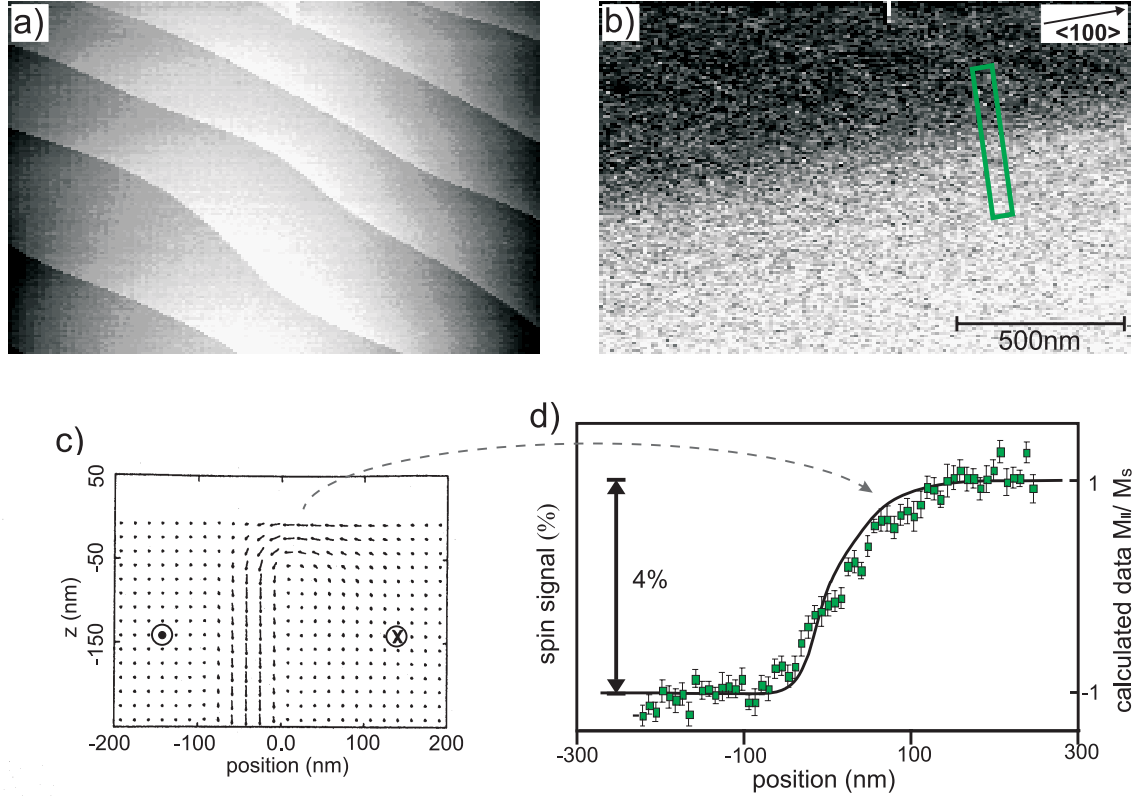
Figure 3.11: Sp-STM image of a) the topography and b) the spin signal of the surface of an Fe-whisker. Images were recorded simultaneously at a bias voltage of 0.4 V and a feedback current of 1 nA. c) Micromagnetic calculations of a 180° domain wall in Fe(001) [96]. The magnetization in the left and right part of the figure points out of and into the image plane, as indicated by the filled circles and the crosses. The arrows show the direction of the magnetization vector in the wall. d) Measured line profile (green squares and left scale) across the 180° domain wall at the position indicated by the green box in b). The error bars are the standard deviation of the mean value of 29 line scans. The black solid line represents the calculated line profile taken from c) (right scale) [96].

twice as wide as the bulk Bloch wall and penetrates into the crystal approximately by the width of the Bloch wall. Fig. 3.11d) shows a line profile over the measured 180° domain wall, obtained by averaging over 29 line scans (green squares). The line profile is taken at the position of the green box in Fig. 3.11b). The black solid line represents the micro-magnetically calculated surface line profile across the 180° domain wall, taken from the data in Fig. 3.11c) [96]. It shows the projection of the magnetization pointing along the domain boundary ($M_\parallel$) normalized to the saturation magnetization ($M_s$). A good agreement is found between the measured and calculated line profile within the lateral calibration error of the scanner ($\approx$ 10%). Néel caps create asymmetric walls [48] which are visible in the measured

and calculated line profile in Fig. 3.11d) so that a *tanh*-function does not fit the experimental wall profile satisfactory. Therefore, to extract the domain wall width we determined the intersection points of a tangent at the middle of the wall profile with a tangent of the maximum spin signal measured on both domains. This gives an estimate of the domain wall width of 150 nm. This is in good agreement with the width of 135±25 nm measured by Oepen and Kirschner [94] defined by the same procedure.

Such a good agreement is not always found. Some of the rings imaged slightly broader domain walls (some 50 nm) or even drag the walls some 100 nm. This might be due to the soft magnetic Fe-whisker where a 180° domain wall can be easily influenced by a small external field (see the introduction of Fe-whiskers in the beginning of this section). Likely, the occasional broadening and the dragging of walls is caused by a small residual stray field of the rings. By assuming a similar dependence of the movement of a 180° domain wall in an applied field as experimentally found by Hubert and Schäfer [48], the stray fields of the rings can be estimated to be of the order of 1 Oe.

The lateral resolution of the spin signal should be much better than the width of the imaged 180° domain wall. This is due to the fact that, as one can see from the topography, monatomic steps are resolved with a resolution of about 8 nm and the lateral resolution of the spin signal should be the same as the one of the topography. The resolution in this case is limited to the distance between two pixels. Because a large area was imaged the pixel density was low.

In conclusion, this experiment shows the first evidence that by Sp-STM measurements one well-defined in-plane component of the spin polarization of the sample surface can be imaged. Since the residual stray fields of the rings are small, even magnetic structures of soft magnetic materials can be imaged. The structure under investigation is well known and hence useful to test a new technique. However, the structure is big enough to be studied by other techniques. The real capability of the Sp-STM is to investigate magnetic structures on the nanometer scale. In the following chapter we focus on such small structures.

# Chapter 4

# Antiferromagnetic Mn films on Fe(001)

Details of magnetic frustrations in an antiferromagnetic film that is grown on a ferromagnetic substrate have been mainly investigated theoretically as discussed in section 2.1.2. Due to the limited lateral resolution of real space magnetic imaging techniques only little experimental data are available. In our Sp-STM study, we focus on antiferromagnetic surfaces of thin antiferromagnetic Mn films grown on a ferromagnetic Fe substrate.

## 4.1  Properties of Mn on Fe(001)

Bulk Mn exists in a wide range of crystallographic structures with different magnetic behavior. Up to 1000 K, bulk Mn appears in a complex cubic phase ($\alpha$-Mn) with 58 atoms per unit cell and is antiferromagnetic below 95 $K$ with a non collinear spin arrangement [97]. Between 1000 K and 1370 K, $\beta$-Mn is a stable cubic structure with 20 atoms per cell. A face centered cubic ($\gamma$-Mn) and body centered cubic ($\delta$-Mn) structure is found between 1370 K - 1410 K and 1410 K - 1518 K (melting point), respectively [98]. Because of the simple atomic structure of the high temperature phases ($\gamma$ and $\delta$ Mn), they have attract much attention in the last years. Many unsuccessful attempts were made to stabilize these phases directly at room temperature. Two ways were found to allow the stabilization: Alloying of Mn with a small amount of other metals or epitaxial growth on a suitable substrate. Mn can be stabilized in a body centered tetragonal (bct) structure on the (100) face of bcc Fe [99]. Many groups confirmed the bct structure of Mn in this system up to about 20 ML [100–102]. Performing strain analysis, Kim and coworkers [101] showed that the bct structure of Mn on Fe(001) could either originate from a deformation of the bulk $\gamma$ or the bulk $\delta$ phase which leads to a misfit of $-9\%$ or $+4\%$. LEED images and RHEED oscillations recorded during the growth of Mn showed that Mn grows in a layer-by-layer mode up to 10 to 25 ML [47,100,101]. Indications of some defects and

disorder were found [103–105] before three dimensional growth sets in. The thickness where the transition takes place is strongly influenced by the substrate quality, e.g. cleanliness, step and defect density, substrate temperature during evaporation, and growth rate [100]. For substrate temperatures between 420 and 470 K, Tulchinsky and coworkers [47] showed that the transition to three dimensional growth takes place between 15 and 23 ML and away from these so-called best growth conditions this transition occurs at thinner Mn film thicknesses. The onset of three dimensional growth is visible in the LEED pattern, where the intensity of diffraction spots fades away and a more complex diffraction pattern is observed [100]. RHEED oscillations vanish for the three dimensional growth [47]. Andrieu and coworkers found that the RHEED pattern taken above the critical thickness is the same as observed on thick $\alpha$-Mn films on Ir(001) [102]. Thus, it is believed that thick Mn films deposited on Fe(001) relax in the $\alpha$-Mn structure. The abrupt roughening is clearly visible in images taken with a scanning electron microscope. The transition from smooth to completely rough films happen within an increase of the Mn film thickness of about 4 ML [47]. This behavior is characteristic for the Stranski-Krastanov growth mode of Mn-films, in which the first 10 to 25 ML grow nearly layer-by-layer before a transition to three dimensional growth sets in. Because of the misfit between Fe and Mn the strain energy increases with increasing film thickness for pseudomorphic growth. At a critical thickness, the pseudomorphic epilayer becomes unstable and the film relaxes by forming defects such as dislocations and roughening of its surface. Likely, the driving force for the transition from layer-by-layer growth to three dimensional growth is the reduction of elastic strain energy induced by the lattice mismatch [106].

Thin Mn films grow pseudomorphically on Fe(001). However, a structural change is found between the second and third ML of Mn [100–102], which is interpreted as a modification of the out-of-plane lattice constant. The out-of-plane lattice constant increases after deposition of the second ML Mn, and it is possibly correlated with a magnetic transition from a ferromagnetic to an antiferromagnetic order of the Mn planes [102]. It is found that thick Mn films have an out-of-plane lattice constant of 0.323 nm [100, 101]. When Mn was deposited at room temperature on Fe(001), no intermixing was found between Mn and Fe. The onset of intermixing was observed by AES for substrate temperatures during the growth between 420 and 440 K [46, 102]. In STM and STS studies interdiffusion of Fe in the first ML Mn is found to start at substrate temperatures during Mn deposition of about 370 K [107]. At this substrate temperature, the intermixing was observed until the fourth Mn layer [105].

The spatial distribution, shape, and size of Mn islands during growth of Mn on Fe was analyzed by STM and STS measurements [104, 105]. In the sub-monolayer range, the growth of Mn at a substrate temperature of 430 K is characterized by small islands with about 10 to 25 nm diameter, an average spacing of the order of 10 nm and predominant step edge orientation along $\langle 100 \rangle$ [104]. Larger, rounder, and more widely spaced islands are found for a film thickness above 2 ML. At the Mn surface of films between 4 to 10 ML small regions with rectangular cross-shaped
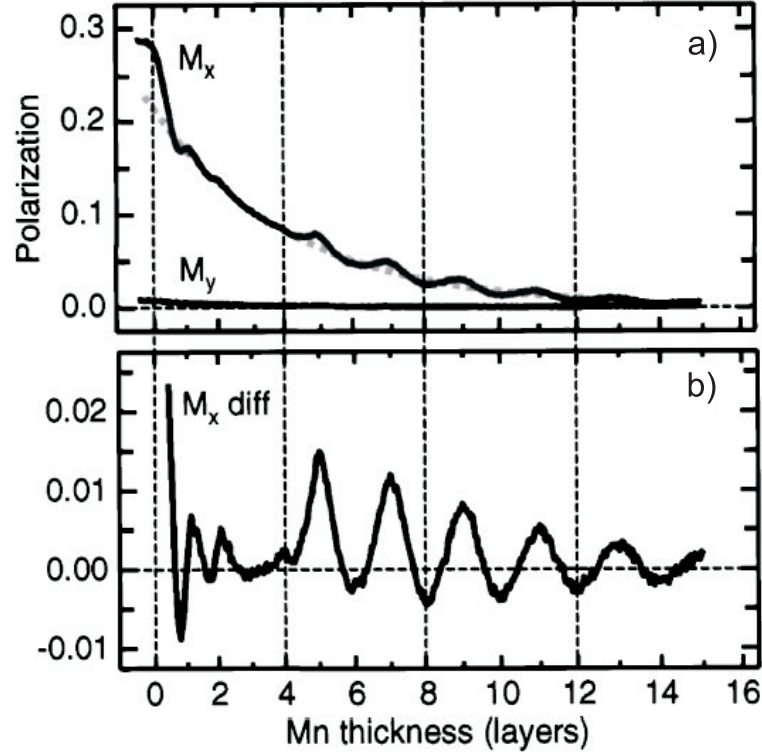
Figure 4.1: a) Line scans obtained by SEMPA measurements on a bare Mn wedge on an Fe-whisker [47]. The Mn thickness varied from 0 to 16 ML. The magnetization component collinear ($M_x$) and perpendicular ($M_y$) to the Fe-whisker magnetization as a function of the Mn film thickness is shown. b) presents the line scan $M_x$ of a) after substraction of the exponential background (indicated by the gray dotted line in a)) caused by the Fe substrate.

patterns start to form [104, 105]. It was speculated that these small rectangular islands are local reconstructions and a precursor to three-dimensional growth, the phase transition to $\alpha$-Mn which was found in thicker films.

The first evidence that Mn on Fe(001) forms ferromagnetic planes which order antiferromagnetically to each other with a period of two ML was presented by Walker and Hopster [46]. More recently, the layer-wise antiferromagnetic order between adjacent Mn atomic layers on Fe(001) was confirmed by scanning electron microscopy measurements with polarization analysis (SEMPA) [47]. Fig. 4.1 shows line scans of the magnetization component collinear to the magnetization of the Fe substrate ($M_x$) and perpendicular to it ($M_y$) as a function of the Mn film thickness [47]. An exponentially decay with superimposed oscillations is visible in the $M_x$ component while no $M_y$ component is observed (Fig. 4.1a)). Fig. 4.1b) shows the $M_x$ component after subtracting an exponential background, which is related to the Fe substrate, to clearly demonstrate the oscillations having a period of two ML with the beginning of the fourth Mn layer. This shows the layer-wise antiferromagnetic order. The growth

temperature was 420 K. The onset of the two layer oscillations varied depending on the substrate temperature during the Mn film growth [47]. The oscillations started with the third Mn layer when evaporating the Mn film at 520 K. The absence of the $M_y$ magnetization component is ascribed to two reasons. The first one is that Mn couples solely collinearly to the magnetization of the underlaying Fe substrate. The second is that the resolution of SEMPA during this measurement was about 100 nm. If non-collinear coupling is present in the form of equal numbers of small domains they may be averaged out.

Contradicting results exist concerning the magnetic coupling of the first and second Mn layer on Fe(001). Some groups confirm a ferromagnetic alignment of the magnetic moments of the first Mn layer [108, 109] whereas other found hints for an antiferromagnetic alignment [110, 111]. The investigation of the magnetic structure performed with SEMPA [47] suggest that the magnetic orientation of the first few layers is sensitive to the quality and crystallographic nature of the underlaying Fe. Andrieu and coworkers [112] found that the sign of the coupling of the first Mn layer strongly depends on the amount of O on the Fe substrate surface. They found a transition between ferromagnetic and antiferromagnetic orientation of the first layer with increasing the amount of O on the Fe surface. The following discussion of Sp-STM measurements performed on Mn films on Fe(001) will be similar in case of ferromagnetic or antiferromagnetic order of the first Mn layer and the Fe substrate. No qualitative differences occur.

## 4.2   Experimental results

Before each measurement, the Fe-whisker was cleaned by Ar-sputtering and annealing with the procedure described for the investigation of pure Fe-whisker surfaces in section 3.2. Mn was thermally evaporated and the growth rate was determined by the monolayer period oscillations obtained by MEED. Fig. 4.2 shows such MEED oscillations measured during the growth of Mn on Fe at a substrate temperature of 310 K. Eight MEED oscillations were observable in this measurement. After two strong oscillations, the intensity drops at a coverage of 1.8 ML and the further oscillations have much lower intensities. The coverage of 1.8 ML is determined by the period of the oscillations in the low intensity regime assuming structural homogeneity. A similar behavior of the oscillations were reported in the literature [47] and the drop in intensity occurred in the region where other groups observed structural changes in the Mn film [100–102].

To increase the accuracy to fractions of a ML even in thicker films, STM images of the topography were used. STM images yield a quite exact determination of the coverage between n and n+1 ML. Thus, the integer coverage n was defined by MEED and the fractional coverage between n and n+1 ML by topographic STM images. In the following, the uncertainty of the Mn coverage is defined by the accuracy of MEED measurements and all Mn film thicknesses presented in this work are given
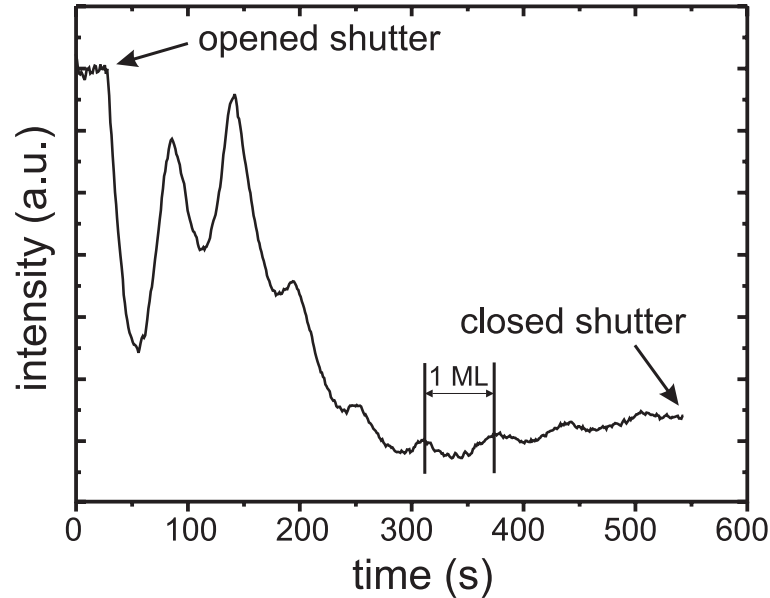
Figure 4.2: MEED oscillations obtained during the growth of Mn on Fe(001) at a substrate temperature of 310 K.

with an estimated error of 10%.

In Fig. 4.3a) and b) two STM images show the topography of 8.9 ML and 9.2 ML Mn. The substrate temperature during evaporation for the film presented in a) was 310 K and in b) 370 K. Each gray level corresponds to a change in thickness by one ML. The structure observed at the surface of the Mn films, evaporated at different substrate temperatures show a completely different behavior. Note that image Fig. 4.3a) has a magnified scale of a factor of 4 compared to image Fig. 4.3b). The film evaporated at lower substrate temperature forms small islands and four different levels are exposed at the surface. Small brighter dots are visible on the different levels (∼3 nm in diameter) which may have two possible origins. They can arise from intermixing in the first few Mn layers shining through the complete film due to the different lattice constants of Fe and Mn. As the substrate temperature during evaporation was close to room temperature, no intermixing should occur [107]. We believe that this structure is more likely due to the onset of the phase transition to $\alpha$-Mn. The Mn film is already in the thickness range where this phase transition can set in.

The film deposited at 370 K (Fig. 4.3b) shows a much smoother surface with rounder, larger, and more widely spaced islands. Weakly two steps of subatomic height are visible, indicated by black arrows. These steps are caused by steps of the underlying Fe substrate. The difference in the out-of-plane lattice constant between Fe and Mn, for Mn films thicker than 5 ML is 0.018 nm hence, n+1 ML Mn are higher by 0.018 nm compared to n ML Mn plus 1 ML Fe. Thus, where Mn overgrows an Fe step edge, steps of subatomic height are formed at the surface of the Mn film.
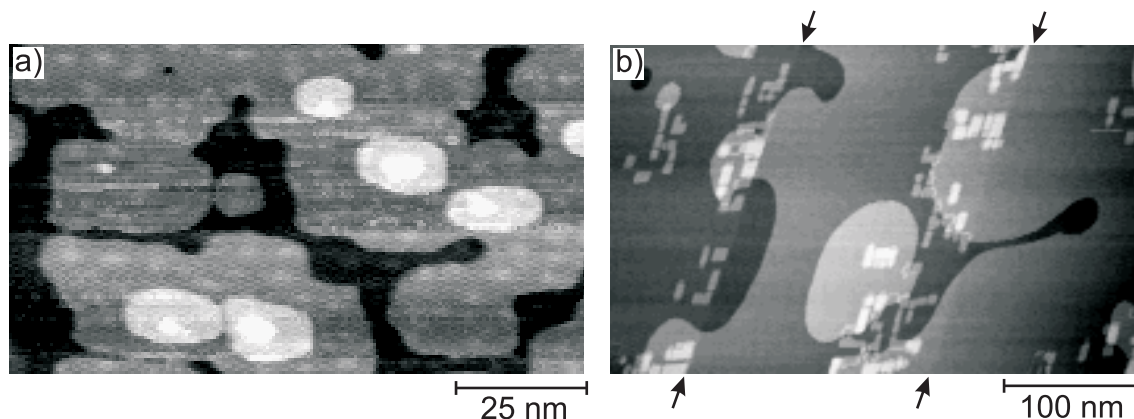
Figure 4.3: STM images of a) 8.9 ML and b) 9.2 ML Mn on Fe(001). The films were deposited at a substrate temperature of 310 K (a)) and 370 K (b)), respectively. In a) a bias voltage of -0.2 V was used and in b) 0.4 V, in both cases the average tunneling current was 3 nA. Note the different scale of these images.

Pierce and coworker found that such buried Fe steps are visible through the Mn films up to a film thickness of 10 ML.

Beside the large Mn terraces and the round Mn islands, small rectangular islands are visible which are found frequently along buried Fe step edges and defects. This observation is in agreement with the results found by Pierce and coworkers [104]. They related these islands to local reconstructions being a precursor to the phase transition to $\alpha$-Mn. We found that these islands have predominantly edges along $\langle 100 \rangle$. The analysis of the size of these islands showed no special unit cells. Every size within atomic distances was found. The height is about $\frac{2}{3}$ of the height of monatomic steps between Mn terraces.

All Mn films investigated with the Sp-STM in the following study were grown at 370 K.

### 4.2.1  Magnetic order in Mn films

As already discussed, thin Mn layers on Fe(001) couple ferromagnetically within one Mn atomic plane while normal to the surface an antiferromagnetic coupling of neighbored Mn planes with in-plane spin polarization was observed. Fig. 4.4a) shows a schematic model of the topographic and magnetic behavior of Mn layers on Fe(001). The arrows represent the direction of the magnetic moments of the atomic Mn planes and the Fe substrate, also visualized by the different gray levels. In the schema, ferromagnetic order between the first Mn layer and the Fe substrate was assumed, but antiferromagnetic order would not change the following results except the sign of the spin polarization. When several Mn layers are exposed at the surface, in adjacent Mn layers the magnetization points into opposite directions
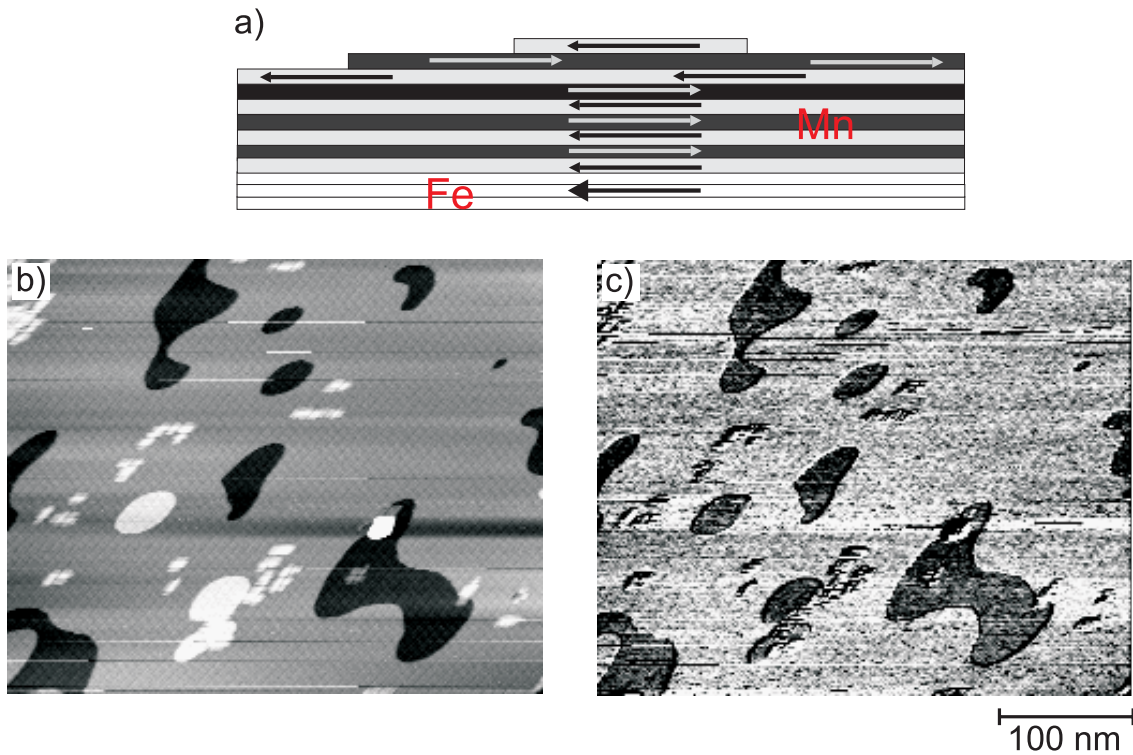
Figure 4.4: a) Sketch of the magnetic order of Mn films on Fe(001). The ferromagnetic Fe substrate and the antiferromagnetic order between adjacent Mn layers is indicated by different gray levels and arrows pointing in opposite directions. b) Topography and c) corresponding spin signal of 11.9 ML Mn on Fe (001) measured with the Sp-STM.

due to the layer-wise antiferromagnetic order, as schematically shown (Fig. 4.4a)). In Fig. 4.4b) and c) the topography and the corresponding spin signal taken with the Sp-STM on a 11.9 ML Mn film on Fe(001) are presented. Three different Mn layers are exposed at the surface, a nearly closed layer with some rounded holes and islands (Fig. 4.4b). Again small rectangular islands are also present.

The Fe substrate was homogenously magnetized in one direction over the whole imaged area, as determined by Kerr-microscopy. The direction of sensitivity of the ring was chosen collinear to the magnetization of the Fe substrate. Thus, the imaged spin signal shows the projection of the spin component collinear to the Fe magnetization. In the spin signal (Fig. 4.4c), clearly the layer-wise antiferromagnetic order between the three different Mn layers is visible. The spin polarization between adjacent Mn layers is opposite, indicated by the black and white areas. The spin signal for n and n+2 ML Mn is the same. This observation is in agreement with results found by Yamada and coworkers [6]. The Sp-STM measurement was performed with a bias voltage of 0.1 V at an average tunneling current of 3 nA. Under these conditions, the highest spin contrast was found, as will be discussed in
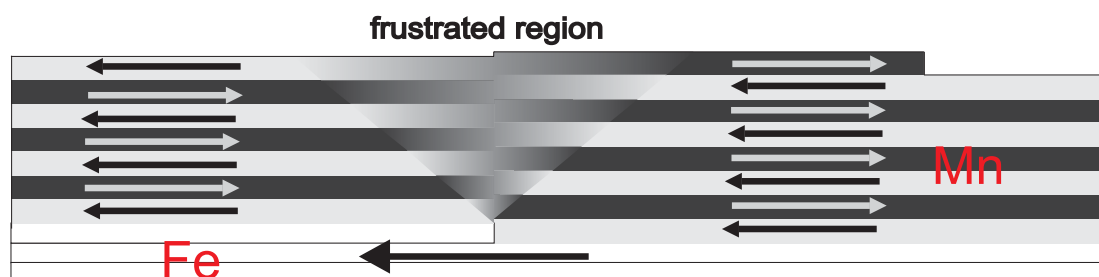
Figure 4.5: Schema of Mn layers overgrowing an Fe substrate step. The arrows indicate the direction of the local magnetization in each layer. Above the buried Fe step edge a magnetically frustrated region occurs.

section 4.2.2. All following Sp-STM images were taken under these conditions. The spin signal between oppositely spin-polarized Mn layers is about 1.2%. In spite of this low contrast, the signal to-noise-ratio is high. This magnetic order of the Mn film was found in images taken on one Fe terrace.

Around each island and hole, a contrast is visible in the spin signal close to the edges (Fig. 4.4c)). In general, such a cross talk of the topographic signal in the spin signal is always visible at the position of step edges but the size and the spatial extension changes depending on the tip apex. This will be discussed in more detail in section 4.2.1.

**Topologically induced magnetic frustrations**

The unperturbed layer-wise antiferromagnetic order is disturbed if a step of the underlaying Fe substrate is present. Fig. 4.5 presents schematically the topological and magnetic situation of Mn layers overgrowing a step edge of the Fe substrate underneath. The nomenclature is the same as presented in Fig. 4.4a). The thickness of the Mn layers on both sides of a monatomic Fe step differs by one ML. This means n layers Mn are grown on the upper side of the Fe substrate step edge and n+1 layers on the lower side. Due to the vertical lattice mismatch, subatomic steps are formed at the Mn film surface at the position of Fe step edges, as already shown in Fig. 4.3b). The situation of the magnetic order above such step edges is more complicated. An undisturbed layer-wise antiferromagnetic order within the Mn film is not possible when the Mn moments at the interface, on both sides of the step edge are aligned in the same direction by the Fe substrate. Thus, Mn layers which meet at the position of the Fe step edge have an opposite spin polarization. This leads to a magnetic frustration. When the Mn film thickness is smaller than the distance between two Fe steps, it is likely that the frustration reaches the Mn film surface, as schematically indicated in Fig. 4.5 (see section 2.1).

Fig. 4.6 shows Sp-STM images of the topography and the corresponding spin signal of a 6.9 ML Mn film grown over monatomic steps of the Fe substrate. In the topography, three buried Fe steps are visible indicated by the black arrows. The
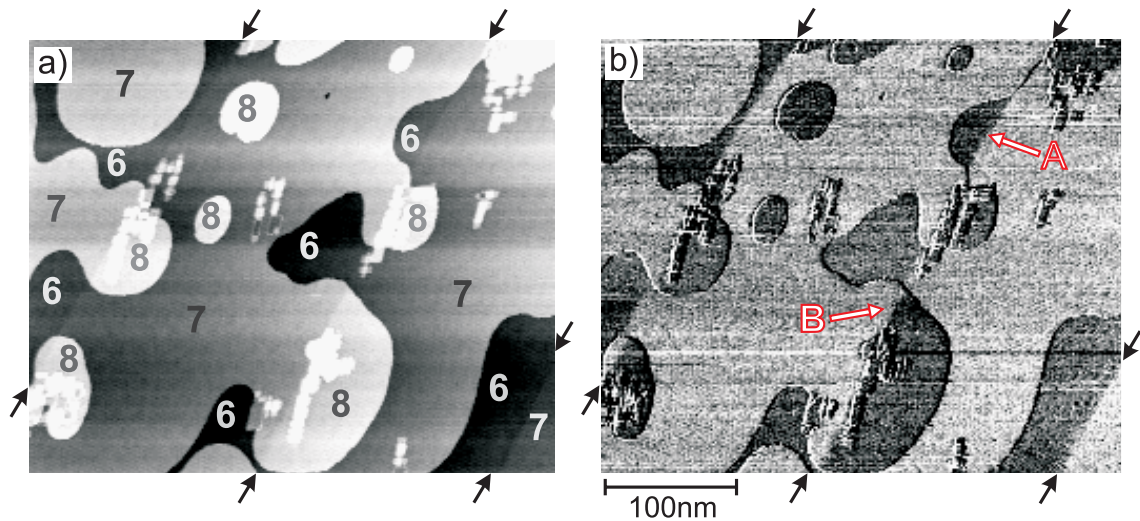
Figure 4.6: Sp-STM image of the topography a) and corresponding spin signal b) of 6.9 ML Mn on Fe(001). Three Fe step edges are running almost vertically through the images, indicated by black arrows. The layer-wise antiferromagnetic order and the rotation of the magnetization of 180° above the buried Fe step edges are visible (e.g. at point A and B). The different Mn layer thicknesses are indicated by numbers in a).

Mn coverage changes by one ML on both sides of the step edges which is clarified by the numbers presenting the different Mn layers. In the spin signal, the layer-wise antiferromagnetic order of neighboring Mn layers separated by monatomic Mn steps is visible. In addition, magnetic frustrations are visible in the regions above the buried Fe step edges, each separating the Mn film into two domains. Along the three buried Fe step edges, a reversal of the spin contrast appears. In these regions the spin polarization of the Mn rotates by 180°. In the areas indicated by A and B, the coverage changes from 6 to 7 ML Mn and from 7 to 8 ML along the same buried Fe step edge. As a consequence of the layer-wise antiferromagnetic order the contrast is reversed. Identical situations occur at other areas in this image. The magnetically frustrated regions are similar to 180° domain walls in the antiferromagnetic film but they are pinned at the Fe substrate step edges. For thin films, these regions are much narrower than bulk domain walls, as will be shown later.

The observation of the magnetically frustrated regions at the surface of thin Mn films at the position of buried Fe step edges indicates that the magnetic frustrations are extended throughout the whole Mn film up to the interface, as schematically shown in Fig. 4.5. This means that the coupling energy at the interface between Fe and Mn is higher than the domain wall energy in the Mn film which is likely for thin films. However, Sp-STM is only surface sensitive so that the behavior within the Mn film is not accessible.

A closer look at the region above a buried Fe step edge allows to study the
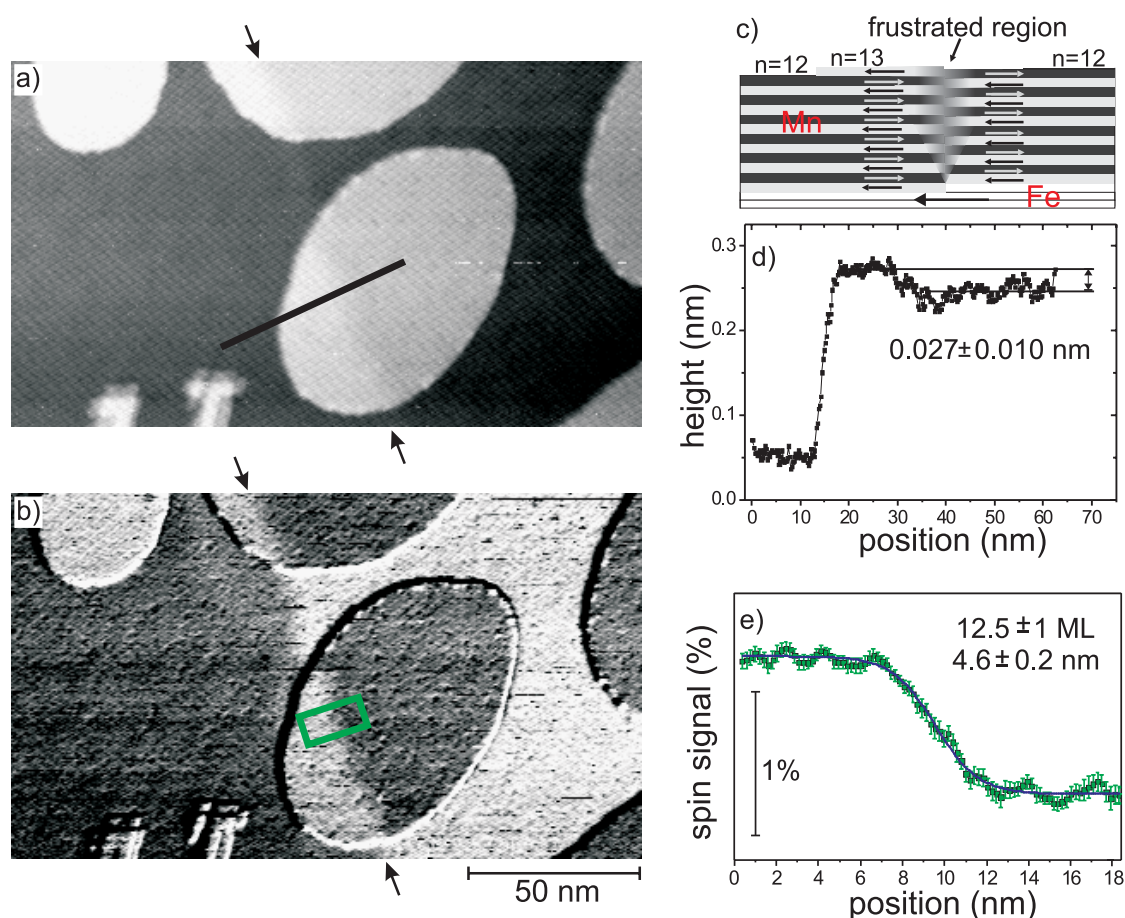
Figure 4.7: Sp-STM image of a) the topography and b) the corresponding spin signal of 11.9 ML Mn on Fe(001). One buried Fe step edge is running almost vertically through the center of the images, indicated by arrows. c) Sketch of the cross section along the black line in a). d) Line profile taken along the black line in a) showing a monatomic Mn step and a step of subatomic height formed because of a buried Fe step. e) Line profile (averaged over 70 lines) across the magnetically frustrated region in the Mn over-layer at the position of the green box in b). The solid line represents a fit of a *tanh*-function to the wall profile. In all images, line profiles shown in green are line profiles across magnetic frustrations.

magnetic behavior of the magnetic frustration in more detail. A magnified image of such a region is shown in Fig. 4.7 (a) topography and b) corresponding spin signal). Here, one buried Fe step edge is running almost vertically through the center of the imaged area (black arrows as guideline). The line profile in Fig. 4.7c) taken along the black line in Fig. 4.7a) shows a step of monatomic height between two different Mn layers ($\approx 0.16$ nm) and a step of subatomic height ($\approx 0.020$ nm) at the position of a buried Fe step edge due to the different lattice constants of Fe and Mn. In Fig. 4.7b) the layer-wise antiferromagnetic order between the Mn islands and the

Mn layer underneath is clearly visible. Following the way of the buried Fe step edge, a magnetically frustrated region is present in the spin signal. Fig. 4.7d) presents an averaged line profile across the topologically enforced magnetic frustration at the position of the green box in Fig. 4.7b)). The measurements indicate that the magnetic frustration has a certain lateral extension[1]. The difference of the spin signal is about 0.9%. To estimate the wall width at the surface, the experimental profile is fitted with a *tanh*-function (see section 2.1.1). This function is the exact analytical solution for a profile across a one dimensional domain wall in an infinite uniaxial system [48], and it is given by equation 2.2. This *tanh*-function is plotted as a blue line in Fig. 4.7d) and it reproduces the shape of the transition region well. Due to the good agreement, this function is used to determine the wall width which is in this case $4.6 \pm 0.2$ nm. In the fitting procedure, the experimental data is weighted by the errors obtained by the standard deviation of averaging over 70 line scans at every individual position. The weighted fit assigns greater importance to less noisy data points allowing a more accurate estimate for the fit parameters. The given error of the wall width only includes the statistical error as determined by the fitting routine. In the following, the presented wall widths are always given within this error. Errors arising for example from lateral calibration of the piezo of the scanner and errors caused by lateral drift during the measurement are not included.

The weak, regular pattern visible in the topography and in the spin signal (Fig. 4.7) is caused by noise. The frequency of this noise level is between 20 and 30 Hz and originates most likely from mechanical vibrations of the STM. The mean amplitude is about 23 pm. In addition, again the contrast at the step edges is visible. Nevertheless, no cross talk is visible in the spin signal at the position of subatomic steps at the position of buried Fe step edges.

In the following, the behavior of the magnetically frustrated regions with increasing Mn film thickness is investigated.

**Dependence of the width of the magnetically frustrated regions on the Mn film thickness**

The width of the magnetically frustrated regions was studied for several Mn film thicknesses. A Sp-STM image of the thinnest Mn film (2.7 ML) on which a spin contrast was obtained, is presented in Fig. 4.8. Andrieu and coworkers observed that the layer-wise antiferromagnetic order starts between the second and third ML Mn [102]. Tulchinsky and coworkers showed that the beginning of the two ML oscillations depends on the substrate temperature during Mn deposition. As visible in Fig. 4.1, magnetization changes occur already in the sub-monolayer range of Mn films.

In the Sp-STM image, four Mn terraces and two buried Fe steps are visible in the topography (Fig. 4.8a)), the latter are indicated by arrows. In this case, n Mn

---

[1]Note, this width is not determined by the lateral resolution of the Sp-STM. The resolution is much better, as will be shown later.
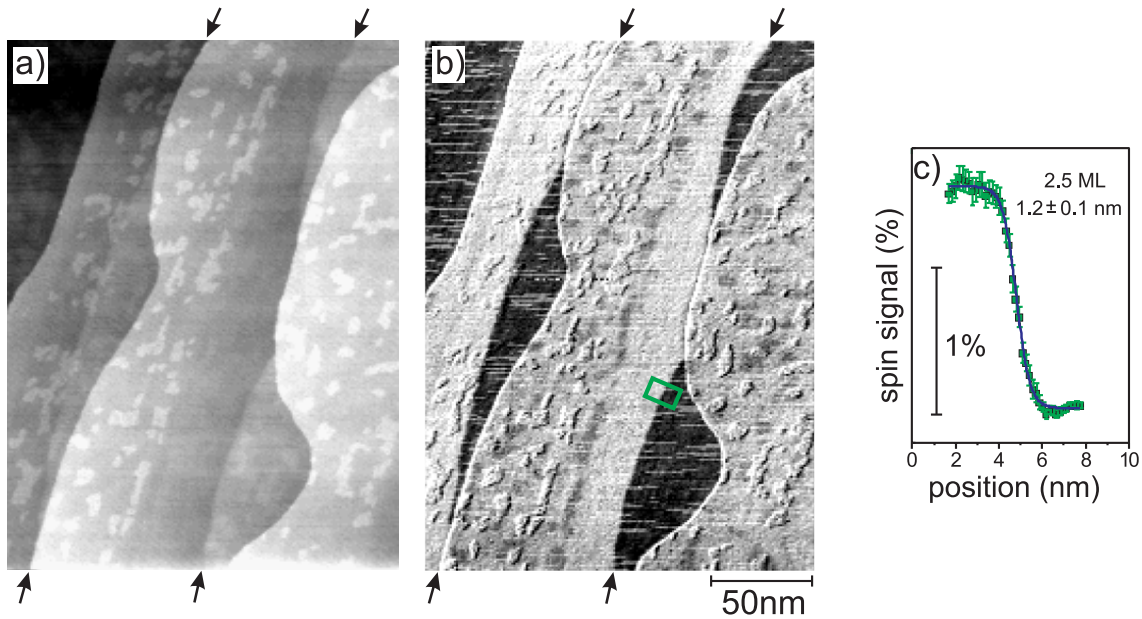
Figure 4.8: Sp-STM image of the topography a) and the corresponding spin signal b) of 2.7 ML Mn on Fe(001). The black arrows indicate the positions of buried Fe step edges. c) Line profile taken across a magnetically frustrated region at the position of the green box in b).

layers plus 1 ML Fe appear higher in the topography than n+1 ML Mn, because the out-of-plane lattice constant for thin Mn films, up to 2 or 3 ML is smaller than that of Fe. This reverses for thicker Mn films (see Fig. 4.6c)), where the out-of-plane lattice constant is larger than that of Fe. This observation is in agreement with the increase of the out-of-plane lattice constant of Mn for thicker films [101]. Beside the monatomic steps between Mn terraces and subatomic steps, formed by underlying Fe steps, small patches are imaged on the Mn terraces (Fig. 4.8a)). They have a width of about 10 nm and a height of about 50 pm and are more frequently found close to the edges of Mn terraces. From literature it is known that Mn intermixes with Fe for substrate temperatures above 370 K during Mn deposition [107]. Thus, most likely these islands are created by interdiffusion. Note on this thin Mn film, the small patches are likely due to intermixing, whereas the small rectangular islands of thicker films are related to the phase transition of Mn.

Since the spin signal contains only changes in the spin polarization, the spin polarization at the sample surface of the intermixed and alloyed layers can be imaged. In the corresponding spin signal (Fig. 4.8b)), the layer-wise antiferromagnetic order and the formation of a magnetic frustration along the buried Fe step edges are visible. We analyzed the width of the magnetically frustrated region between the second and third ML Mn. The line profile presented in Fig. 4.8c) was taken at the
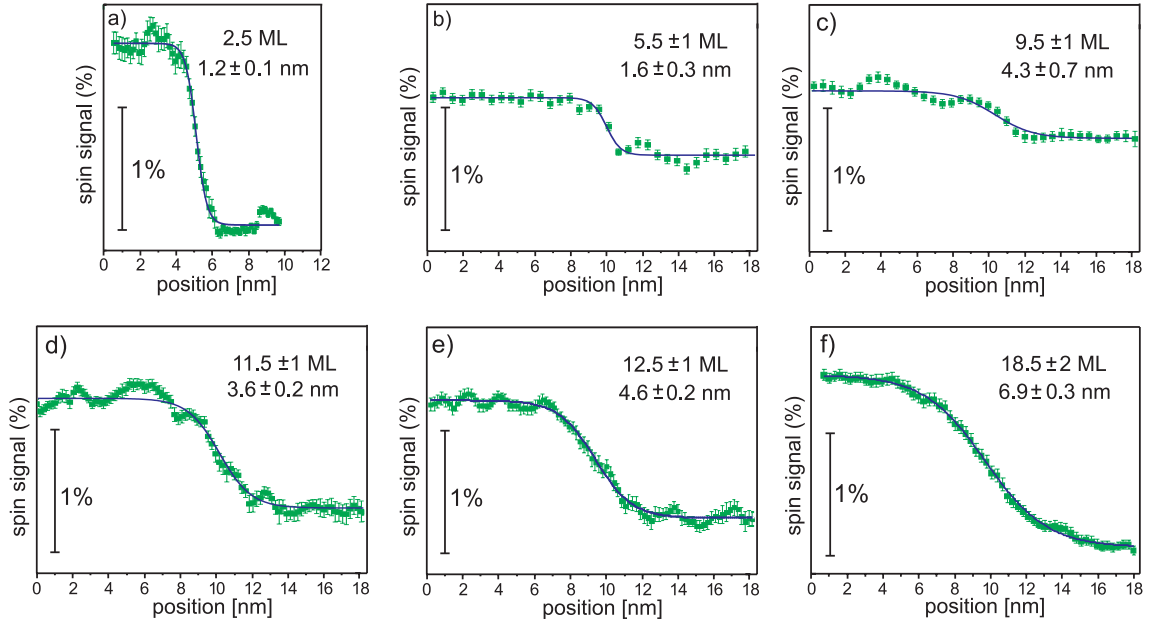
Figure 4.9: Six line profiles across magnetically frustrated regions in Mn films of different film thicknesses. The film thickness is presented by n+0.5 ML and the wall width in nm, both are indicated in the images.

marked area in Fig. 4.8b) where no changes of the contrast due to intermixing was observed. For this a thin Mn film, we found a narrow wall of only 1.2 nm across a buried Fe step edge. This is the sharpest magnetic feature we found on Mn films on Fe(001). From the line profile one can see that the lateral resolution of the Sp-STM is at least 1.2 nm.

The small darker areas (lateral extension of about 10 nm) which are only visible in the spin signal are most likely caused by intermixing of Fe and Mn resulting in a slightly different spin polarization. This measurement shows the capability of Sp-STM to investigate the spin polarization of intermixed regions independently of changes in the topography. The short, sharp white lines interrupting the spin signal are likely due to changes of the tip apex during scanning.

A selection of several line profiles obtained across magnetically frustrated regions in Mn films having different thicknesses (Fig. 4.9) clearly shows a widening of these regions with increasing Mn film thickness. The smallest width of 1.2±0.1 nm was imaged between the second and third ML Mn and the widest one of 6.9±0.3 nm between 18 and 19 ML (±2 ML) Mn. Thicker Mn films could not be investigated due to the phase transition to $\alpha$-Mn resulting in a three dimensional growth and rough surfaces.

The wall width across buried Fe step edges was determined for the six different Mn film thicknesses presented in Fig. 4.9. The widths of the magnetically frustrated regions were always extracted by fitting the experimental line profiles averaged over 25 to 70 lines with a *tanh*-function (equation 2.2). Fig. 4.10 shows the width of
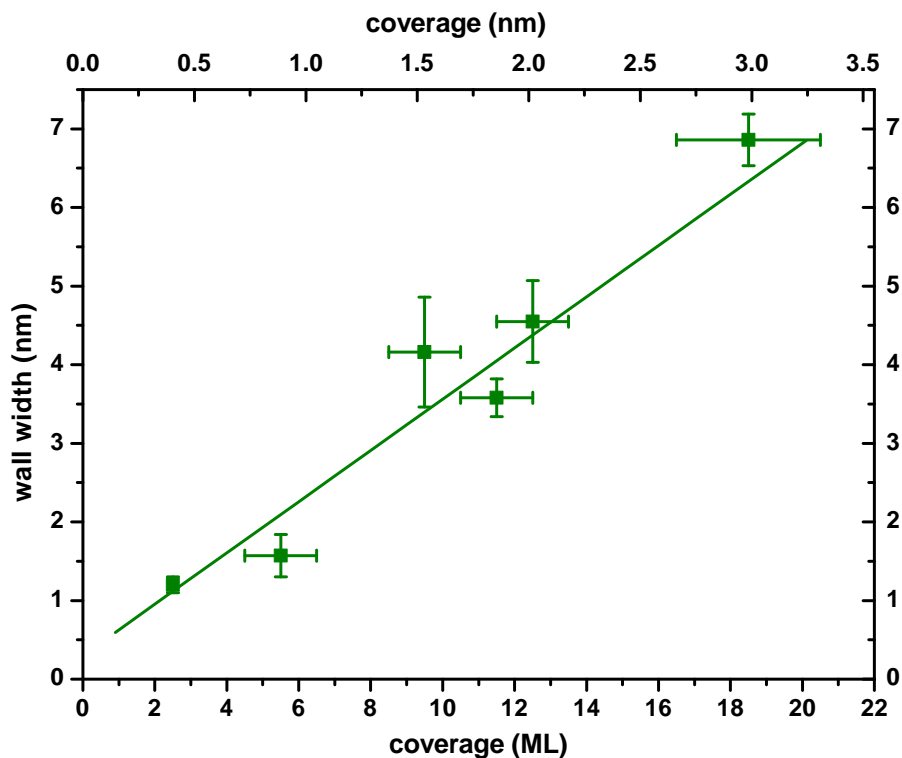
Figure 4.10: The width of magnetically frustrated regions of Mn surface layers as a function of the Mn film thickness in ML (bottom scale) and equivalent in nm (top scale). The solid line is a linear fit to the experimental data points.

magnetically frustrated regions as a function of the Mn film thickness. Since the wall occurs between two different Mn layers, i.e. n and n+1, we followed the nomenclature of Stoeffler and coworkers [62] and plotted the value of the wall width at the position of n+0.5 ML Mn. The error bars in the Mn thickness result from the uncertainty of the evaporation rate. For the wall width the statistical errors are indicated, as described above. Fig. 4.10 shows that the wall broadens linearly with increasing Mn film thickness, as indicated by a linear function fitted to the experimental data [8]. This behavior of the widening of magnetically frustrated regions with increasing Mn film thickness will be discussed in more details in section 5.1.

### Deviations from the layer-wise antiferromagnetic order of Mn

Normally, we observed the layer-wise antiferromagnetic order of Mn films on Fe(001) and magnetically frustrated regions in the Mn film at the position of buried Fe step edges. At some areas, we found no formation of a magnetic frustration at
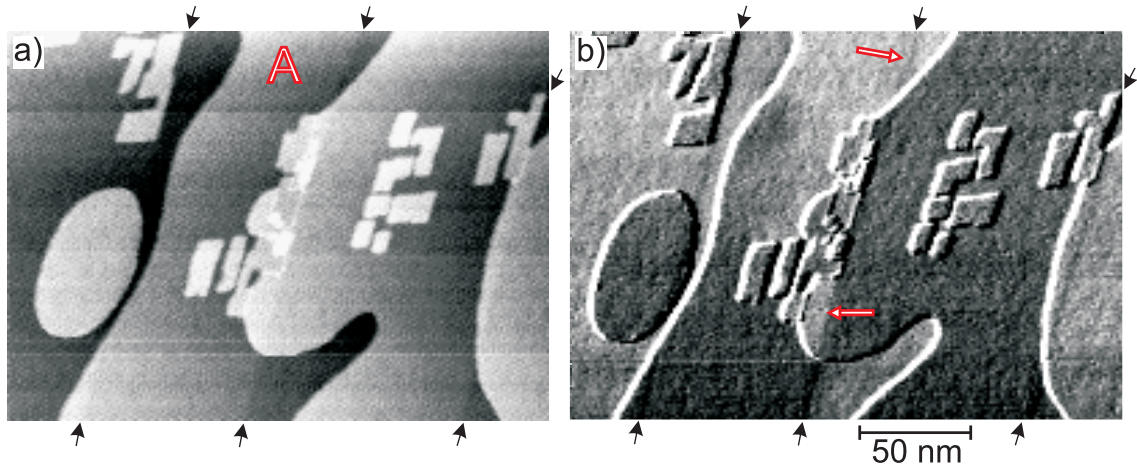
Figure 4.11: Sp-STM image of a) the topography and b) the corresponding spin signal of 9.2 ML Mn on Fe(001). Deviations of the magnetic order at the buried Fe step edges, as described so far are visible. The red arrows indicate a buried Fe step edge where a magnetic frustration is formed in the lower part of the image which is absent in the upper half. The black arrows indicate again buried Fe step edges.

the surface of Mn films, though a buried Fe step edge was present. No change of the projection of the spin polarization along the direction of the sensitivity of the ring appeared. Thus, the magnetic order in this case has to be different from the above discussed case. One example is presented in Fig. 4.11. In the topography (Fig. 4.11a)), three buried Fe step edges are visible running vertically through the image. In the corresponding spin signal, a clear spin contrast is visible, showing for example the alternating spin signal on both sides of Mn terraces separated by monatomic steps. Along the buried Fe step edges on the left and right side of the image, no magnetically frustrated regions are visible. Following the way along the buried Fe step edge running through the middle of the image, a magnetically frustrated region is formed in the lower part which disappeared in the upper half of the image. This is pointed out by the two red arrows. The transition between the two kinds of magnetic orders at this Fe step edge results in the formation of an extended magnetically frustrated region in one Mn layer, in this case visible on the Mn terrace A (Fig. 4.11a)). These changes of the magnetic order along buried Fe step edges occurred mainly in regions where an accumulation of the rectangular islands was found. It seems likely that the rectangular islands influence the order in the Mn film. Because a magnetic frustration has to occur somewhere when the Mn film grows over an Fe step edge, it might be that in this case a closed wall is formed near the interface as schematically shown in Fig. 2.4c).

We also observed a change from one configuration to the other by scanning the same area more than once. This case is presented in Fig. 4.12. Fig. 4.12a) and b) shows the topography and the corresponding spin signal measured during the first scan. Only one buried Fe step edge is running vertically through the image
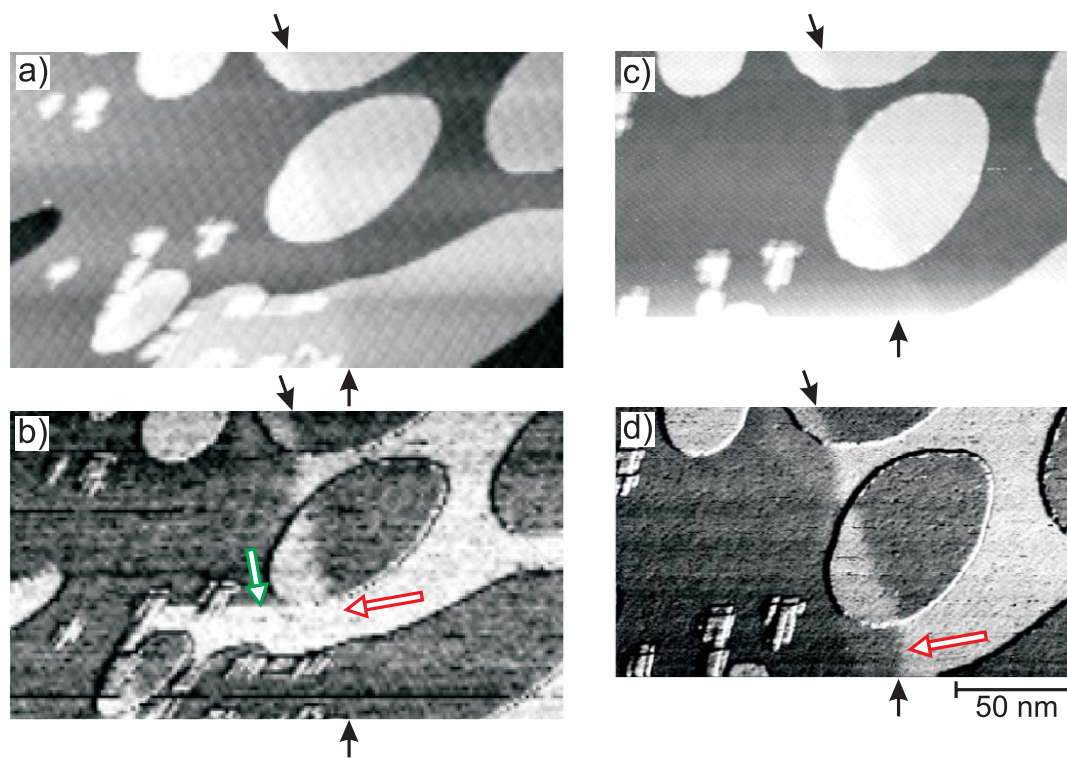
Figure 4.12: Sp-STM images, a), c) topography and b), d) corresponding spin signal of 11.9 ML Mn on Fe(001). Both images are taken at the same area but images c) and d) were taken 2 hours later than a) and b). The red arrows indicate a region where a change in the magnetic order along a buried Fe step edge was observed. Deviations in the shape of the imaged structures between a), b) and c), d) are caused by a different lateral drift of the sample during scanning. In image a) and b) a drift mainly in the horizontal direction occurred.

(indicated by the black arrows). In the upper part of the spin image a magnetically frustrated region is formed in the Mn layer whereas in the lower part no reversal of the spin polarization is observed at the step edge. Again, the behavior of the frustration changes in the vicinity of an accumulation of rectangular islands. The region of interest is indicated by the red arrow. Fig. 4.12c) and d) shows the same scan area imaged 2 hours later. In the mean time, images were taken by zooming into the area of the upper part of Fig. 4.12a). The magnetic frustration along the buried Fe step edge is now formed in the entire imaged area. The red arrow shows the position to which the domain wall shifted. The position of the buried Fe step edge is difficult to see in Fig. 4.12c), but the comparison to Fig. 4.12a) shows that the wall in Fig. 4.12d) is really formed along the buried Fe step edge. Comparing the two spin images (Fig. 4.12b) and d)) the whole area left from the red arrows changed the spin polarization by 180°. A change of the magnetization by 180° at the

surface can presumably be attributed to a change of the magnetization within the whole Mn film. However, by Sp-STM we are only sensitive to the surface magnetic structure and thus cannot determine the magnetic order within the subsurface Mn layers.

In Fig. 4.12b), a sharp transition between the two different magnetic configurations occur (see green arrow). There, the contrast changes abruptly from one scan line to the other. The spin signal was imaged for both scan directions, which means for scanning from right to left and from left to right, called forward and backward scan. When comparing the images of forward and backward scan, the contrast in the discussed region is opposite in only one scan line (not shown here). This means that the change occurred during scanning that particular line. In this case, no normal wall is visible. The wall has no extension and is as sharp as the transition between two adjacent line scans. Most likely, the wall position has changed at one lateral scan point. Magnetically frustrated regions were predominantly observed in the Mn surface layer above buried Fe step edges. This indicates that this configuration is energetically more stable than the absence of magnetic frustrations at these positions. However, our measurements show that the system can stay in this metastable configuration long enough to be observed.

The experiment indicated that an energetic barrier had to be overcome to move the magnetic frustration to the position above the Fe substrate step. The simplest assumption is that a magnetic frustration in form of a 180° domain wall had to be formed. We assume that a wall of a length of about 17 nm, corresponding to the length of the region between the two islands indicated by the red arrow in Fig. 4.12b), had to be formed. Once it is established, it can freely move to the step edge. To estimate the probability for that process we used the wall energy of a 180° bulk domain wall according to $2\sqrt{AK}$ [113]. The thermal switching probability can be expressed by an Arrhenius law of the form [114]:

$$\tau = \tau_0 e^{\frac{E_B}{k_B T}} \tag{4.1}$$

where $\tau$ is the inverse of the switching rate and $\tau_0$ is the inverse of the attempt frequency which is of the order of $5*10^{-9}$ s [115]. $k_B$ is the Boltzmann constant and $E_B$ the energy barrier. It is difficult to estimate the energy barrier accurately and a rough estimation suggests a value of 0.5 eV which results in a high probability of thermal switching processes. However, our observations show that switching events are rare. We imaged only this particular one. From this estimation, we can only say that thermal activation provides one possible explanation.

Alternatively, the wall could be moved by effects induced by the Sp-STM electrode. We used a current density of $\approx 10^6$ Acm$^{-2}$. From literature it is known that with a spin-polarized current of a density of $10^7$ Acm$^{-2}$, a current induced switching of magnetic particles is possible [116]. Therefore, it cannot be excluded that the movement of the magnetic frustration is triggered by the spin-polarized current flowing between the SP-STM electrode and the sample while scanning.

**Cross talk in the spin signal**

As already mentioned, a cross talk of the topography is observed in the measured spin signal. Two different explanations for this observation seem reasonable. If the reaction of the feedback loop of the z-piezo is chosen too slow, a higher tunneling current is measured when the STM-tip has to go a step upwards (tip is for a short while too close to the surface) and a lower current is measured when it scans a step downwards (tip is for a short while too far away from the surface). Thus, at step edges, the tunneling conditions are different which causes changes in the spin-polarized tunneling current as well. This mechanism implies that the contrast of the cross talk reverses when changing the scanning direction. This was indeed observed, especially when scanning fast over large areas (of the order of $\mu$m).

In the case of small area scans, the cross talk was found not to depend on the scan direction so that the influence of the feedback loop can be excluded. In this case, large changes of the size, the sign and the spatial extension of the cross talk were found. Variations from day to day or even within one day have been observed. Therefore, this effect is likely influenced by local changes at the tip apex. In accordance with that, in topographic line profiles across islands with monatomic steps, changes in the profiles were found on different island sides (smoother or sharper transitions). Thus, the shape of measured line profiles across a step strongly depends on the exact shape of the tip apex.

The tunneling position at the tip apex may change when the tip is crossing a step edge and sidewise tunneling may occur producing different tunneling conditions. These differences are likely producing changes in the spin-polarized tunneling current and by this may cause a cross talk in the topography and in the spin signal. Even a dependence of the cross talk on the bias voltage was observed which supports the above ideas. This kind of phenomena is inherent to the method and cannot be suppressed easily.

## 4.2.2 Measurement of the voltage dependence of the spin contrast

The difference of the spin-dependent tunneling current between adjacent Mn layers on Fe(001) strongly depends on the bias voltage. All presented spin images were obtained at a bias voltage of 0.1 V, because at this voltage, a high spin contrast was observed. In the following, we show how the spin contrast changes by changing the bias voltage.

The measurements were carried out on Mn films thicker then 4 ML, were a constant electronic structure of Mn films was found [105]. In these measurements, the ring was scanned over the sample surface and at each point the bias voltage was ramped. When the measurements were performed the feedback was on during the ramping of the bias voltage. The spin signal detected in this experiment corresponds to the signal obtained in constant current mode images in our Sp-STM
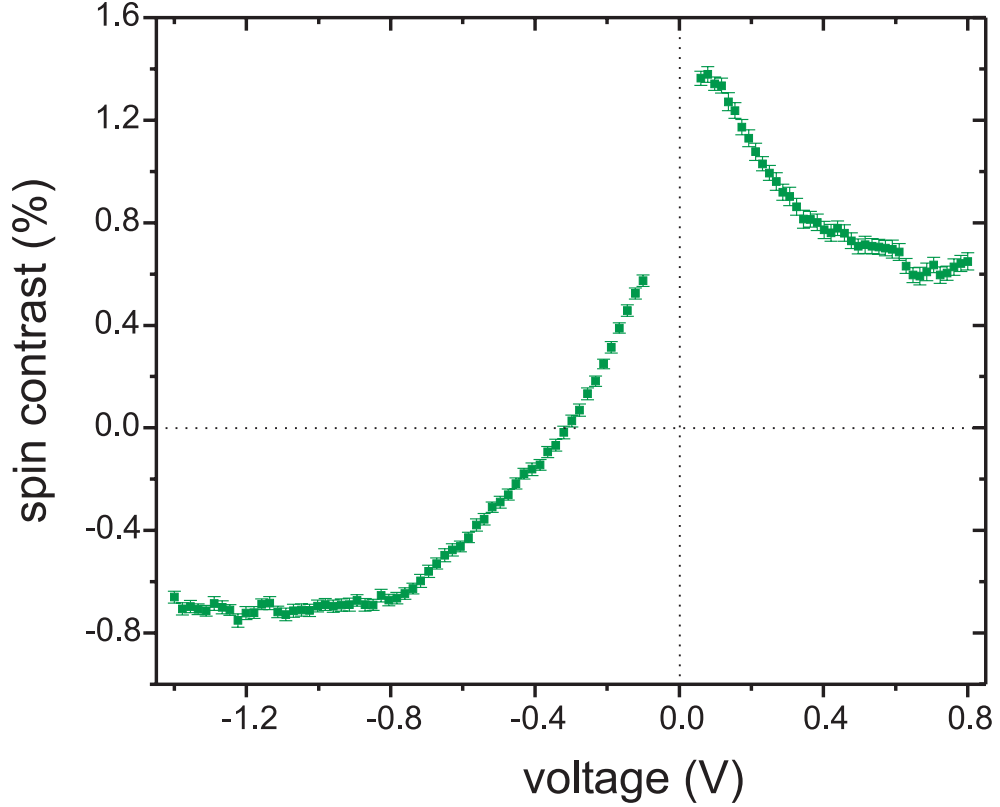
Figure 4.13: Spin contrast between oppositely spin polarized Mn layers normalized to the tunneling current $2\bar{I}$ as a function of the bias voltage. The measurement was performed between 11 and 12 ML ($\pm 1$ ML) Mn.

measurements. This mode was selected to find the maximum spin contrast for the measurement shown before. By changing the bias voltage, the distance between ring and sample changed to keep the average tunneling current constant. Changes of the distance influence the transmission probability of states between ring and sample. For smaller distances, states with $k_{\parallel} \neq 0$ are suppressed less than for larger distances. In our experiment, the voltage was reduced by about a factor of 10 which results in a distance change of the order of 1 Å [67]. In experiments on Co(0001), no influence of the barrier properties on the spin polarization of the tunneling electrons was found for these conditions [117].

Fig. 4.13 presents the result for ramping the bias voltage from $+0.8$ V to $0.06$ V and from $-1.4$ V to $-0.1$ V. The general trend can be described by a positive spin contrast above 0 V, a change of sign and a negative spin contrast below -0.3 V. The spin contrast becomes more negative when the applied voltage is decreases down to -1 V. For positive voltages, the spin contrast is highest at about 0.1 V. For different tips, the size of the spin contrast may change but qualitatively similar results for the voltage dependence were observed.
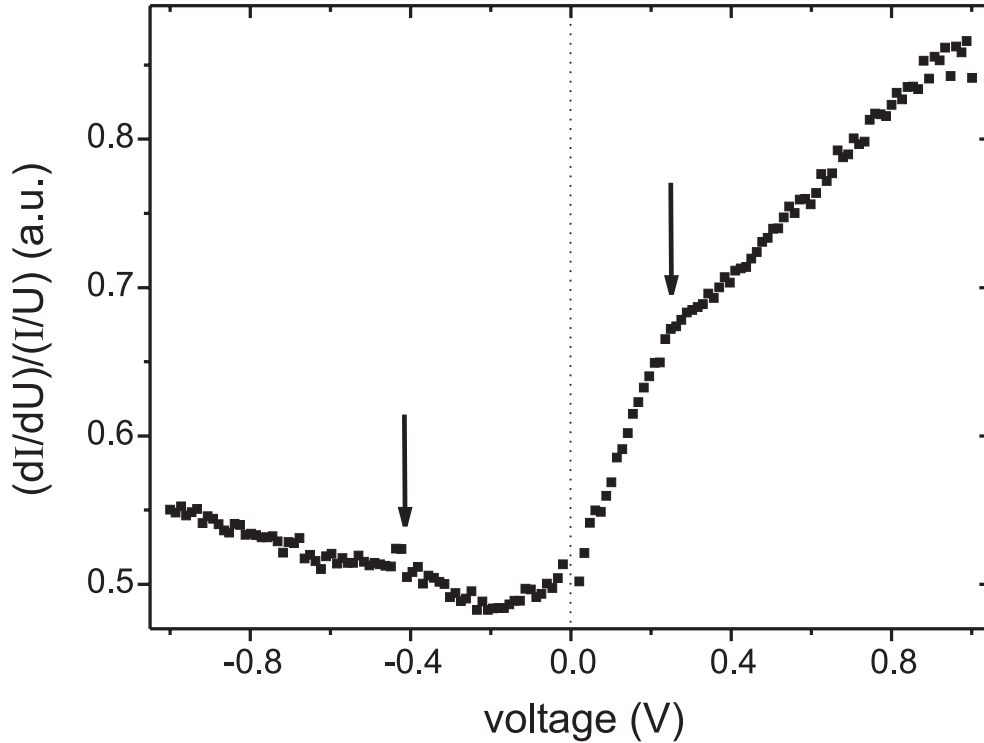
Figure 4.14: Spectroscopy measurement performed on a 6.1 ML Mn film on Fe(001). Shown is a $dI/dU$ spectrum normalized to $I/U$. The black arrows indicate two small shoulders in the spectrum.

STS measurements were performed to compare the behavior of the spin contrast with the electronic structure of the Mn films. For the STS measurements, the tunneling current was stabilized at 1 nA and a bias voltage of 1 V. In this case, the magnetization of the ring was not switched and the spectroscopic measurement was performed on only one Mn terrace. During the measurement, the bias voltage was modulated by 30 mV with a frequency of about 6 kHz and changes of d$I$/d$U$ were detected with a phase sensitive lock-in amplifier. In Fig. 4.14, the normalized d$I$/d$U$ spectrum is presented. Two small shoulders are visible, one at about $+0.25$ V and one at about $-0.5$ V. As discussed in section 2.2, d$I$/d$U$ is assumed to be proportional to the local density of states. In this approximation, the two shoulders indicate that bulk band edges or surface states/resonances are present at these voltages. The shoulder around $+0.25$ V is not far away from the enhanced spin contrast shown in Fig. 4.13. Thus, they are possibly caused by the same electronic properties. However, no direct correlation can be found between the shoulder at about $-0.5$ V and features in the spin contrast. Sp-STS measurements performed by Yamada and coworkers [6] on the same system for Mn films thicker than 4 ML show two features in $(dI/dU)/(I/U)$ spectra. In agreement with our data, one feature is present at about $-0.5$ V, but the other, a pronounced peak at about 0.8 V

is absent in our data. These differences may be caused by differences in the local density of states of the sample or the tip. Differences on the sample surface can be caused by different substrate temperature during Mn deposition or cleanliness of the substrate or the Mn film.

Comparison between our experimental data of the spin contrast as a function of the bias voltage and our STS data and theoretical calculations are given in the discussion in section 5.2.

# Chapter 5

# Discussion

This chapter is divided into two parts. In the first part, the magnetic structure of the magnetically frustrated regions in thin Mn films is discussed. The focus lies on the comparison between the experimentally observed widening of magnetic frustrations with increasing Mn film thickness and model descriptions of this effect. First, we present a continuum model. In the second approach a Heisenberg model is used.

The second part deals with the discussion of the spin contrast as a function of the bias voltage and theoretical descriptions of this experimental finding. The explanations are based on calculated spin-resolved spectral density of states and current asymmetry calculations. These calculations were performed by J. Henk [118].

## 5.1  Magnetically frustrated regions

In section 2.1.2, it was shown that a frustration in the magnetic order occurs if an antiferromagnet is in direct contact to a stepped ferromagnetic surface. For the system Cr on Fe(001), the work of Stoeffler and coworkers predicted magnetic defect lines separating two Cr domains above buried Fe step edges. Their calculations showed that the magnetic frustrations are laterally localized in the vicinity of the buried Fe steps and that they widen with increasing Cr thickness [62]. A similar behavior was experimentally observed for the system Mn on Fe(001), as presented in chapter 4. Sp-STM measurements showed spatially localized magnetically frustrated regions at the surface of thin Mn films above buried Fe step edges. These observations suggest that the Mn spins are pinned at the interface by the exchange interaction to the Fe substrate and that the coupling energy at the interface is higher than the domain wall energy in the thin Mn films. This results in magnetic frustrations running through the entire Mn film above an Fe substrate step edge. In the experimental study of Mn films on Fe(001), a liner widening of the magnetically frustrated region which increased in proportion to the Mn film thickness was found. The smallest width of 1.2±0.1 nm was measured between the second and third ML and the largest width of 6.9±0.3 nm between the 18 and 19 ML (±2 ML). The widening of the magnetically frustrated region is a consequence of the pinning of

the Mn magnetic moments at the interface and the tendency to minimize the exchange energy in the frustrated region. Up to the highest Mn thickness investigated, the width of the magnetically frustrated region is increasing and shows no sign of saturation. This indicates that a bulk like arrangement of magnetic moments in the wall will be reached at much higher thickness which cannot be stabilized for this Mn phase. Therefore, the thickness of 20 ML Mn is still too thin to relax the wall width to its bulk value.

### 5.1.1 Continuum model of the magnetically frustrated regions

In bulk ferromagnets, the width of a 180° domain wall is determined by a competition between the exchange energy and the magnetic anisotropy energy and is given by equation 2.3, in section 2.1. The bulk domain wall width for the cubic itinerant ferromagnets is between 20 and 80 nm [119]. For the layer-wise antiferromagnetic bulk Cr a wall width of about 120 nm [5] has been found. Assuming an antiferromagnetic exchange of similar size and a similar anisotropy, one expects a similar size of a bulk domain wall widths in Mn. By estimating the exchange for Mn (for details see section 5.1.2) and assuming a similar anisotropy as of bulk Fe, a Mn bulk wall width of approximated 20 nm would be expected. Performing a similar approximation by taking the value for the anisotropy for Cr [120], a domain wall width of about 60 nm would result. For the following arguments, the exact knowledge of the bulk domain wall width is not needed. It is only important that it is much larger than the width of the magnetic frustrations measured on the thickest Mn film in our experiments. The linear increase of the magnetic frustration with increasing Mn film thickness supports this argument.

The pinned domain walls in thin Mn layers across buried Fe step edges result in a narrow frustration at the surface between the second and third Mn layer of 1.2 nm. The driving force for the widening of the magnetic frustration for thicker Mn films is the energy which is gained by approaching the bulk domain wall configuration. Thus, the width of the magnetically frustrated region should asymptotically approach its bulk wall width.

Interestingly, we found a slope of the linear increase of the magnetic frustration which is close to 2, meaning that the wall width increases nearly twice as fast as the film thickness. In Fig. 5.1a), the experimental wall width is presented together with the linear function having a slope of 2 (red dotted line).

The slope of 2 of the widening of the magnetically frustrated region can be explained within a continuum model in which the exchange is assumed to be isotropic in any direction. In a similarly frustrated ferromagnet, this would mean that the pinned wall widens isotropically when increasing the distance from the perturbation. Considering a layer-wise antiferromagnet as a ferromagnet where only the magnetization of every second layer is rotated by 180°, a similar homogeneous widening would be expected for the pinned wall in Mn films at Fe steps. In the case of Mn, this
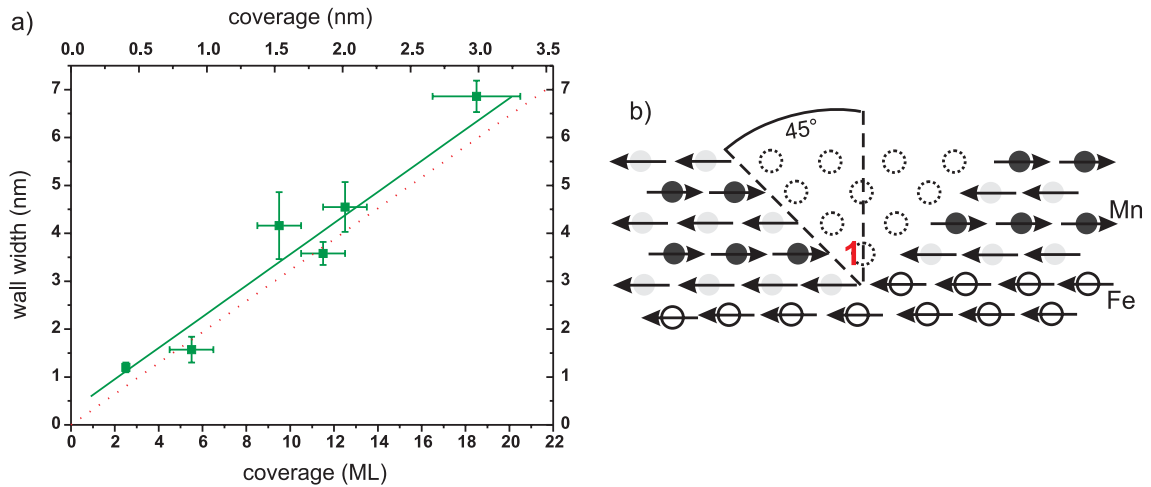
Figure 5.1: The measured data (green data points) with a linear fit (green line) shown in Fig. 4.10 are presented in a) together with a linear function having the slope of twice the film thickness (red dotted line). In b) a schematic sketch of the increase in wall width is presented as expected from simple considerations.

would mean that the ferromagnetic exchange energy within one Mn layer is equal in size to the antiferromagnetic exchange energy to an adjacent Mn layers. The energy needed to turn the magnetization in one point away from its equilibrium state is than only a function of the distance to the neighboring exchange coupled points. This results in a widening of the magnetically frustrated region with an angle of 45°. This corresponds to a linear widening having a slope of twice the film thickness.

Alternatively, this slope can be explained by a simple atomistic bcc model presented in Fig. 5.1b). We again assumed ferromagnetic coupling at the interface between Fe and Mn. Then, the direction of the magnetic moment of atom 1 (see Fig. 5.1b)) placed over the step edge cannot couple ferromagnetically to the Fe atom on the lower right and antiferromagnetically to the Mn atom on the lower left at the same time. The same holds for two Mn atoms in the layer above, for three two layers higher, and so forth which results in an angle of widening of 45°. Again a slope of 2 results.

The linear fit to the experimental data has a slope of 2 but a constant offset occurs to the expected linear function derived by the two models. This may have several reasons. First, the frustrated region in the Mn induces a torque on the Fe moments at the interface via the exchange interaction. This may induce a tilt of the Fe magnetic moments near the step edges. Some of the exchange energy caused by the frustration would then be transferred to the Fe and would widen the magnetic frustration in the Mn film. Second, the Sp-STM has a finite resolution which can lead to a widening in the measured Mn wall profile, especially for narrow walls. A third reason is the limit of the continuum model at the atomic scale. However, this small offset is about the size as the experimental accuracy.

### 5.1.2  Calculations of the width of magnetically frustrated regions using a Heisenberg model

A different approach which considers the interaction within the exchange coupled system and may provide a quantitative description of the magnetic frustration is a Heisenberg model. The Heisenberg Hamiltonian was introduced in section 2.1. This model is in particular useful due to its simplicity. However, one should keep in mind that localized magnetic moments are considered which is at most a crude approximation for the itinerant magnetic materials like Fe and Mn due to the delocalized nature of the electrons. As shown in Ref. [121], one possibility is to use an effective Heisenberg model to approximate the magnetic interaction in itinerant materials. The itinerant exchange is considered in an effective exchange coupling constant.

To calculate the width of the magnetically frustrated region in the Mn film on Fe(001) an effective Heisenberg model with classical spins is used and in addition, a fourfold magnetic anisotropy is included. The energy of the system can be written as:

$$E = -\frac{1}{2} \sum_{i,j \neq i} J_{ij} cos(\theta_{ij}) + \sum_i K_i sin^2\varphi_i cos^2\varphi_i. \qquad (5.1)$$

In this notation, the size of the magnetic moment is included in the exchange coupling constant $J_{ij}$. For the calculations a constant magnetic moment is assumed in each of the two materials (Fe and Mn). $\theta_{i,j}$ is the relative angle between the directions of the magnetic moments $i$ and $j$. $\varphi_i$ is the angle between the magnetic moment $i$ and the direction of the easy axis of the Fe substrate magnetic moments, and $K_i$ is the anisotropy constant. This means, only a rotation completely in-plane or out-of-plane is allowed and no difference occurs between these two cases because dipole interactions are neglected. Thus, a Néel wall and a Bloch wall are energetically degenerate[1]. To determine the numerical solution, the angles of the magnetic moments are varied to find the minimum energy configuration.

The values for the exchange coupling constants and the anisotropy constant are well known for bulk bcc Fe. M. Pajda and coworkers [121] calculated $J$ up to the tenth nearest neighbor. The main contributions are given by the nearest and next nearest neighbor, where the next nearest neighbor has still a contribution of 57% of the nearest one. This is mainly due to the bcc structure of Fe where differences of the distance between the nearest and next nearest neighbor are small (about 13%). The other contributions are less than 13% [121].

For bct Mn, the values for $J$ can only be estimated. The value for the nearest neighbor is determined by assuming a linear dependence between the ordering temperature and the exchange coupling constant [121]. The Néel temperature of $\gamma$-Mn is $T_N = 540$ K [122, 123]. Using this temperature and $J \propto T_N$ a value of $J = -20$ meV is estimated for the nearest neighbor exchange coupling constant. For estimating $J$

---

[1]From geometry of a bcc crystalline structure, an antiparallel alignment of all nearest neighbors is possible. Assuming only nearest neighbor interaction, this arrangement is energetically favorable compared to more complex antiferromagnetic order.
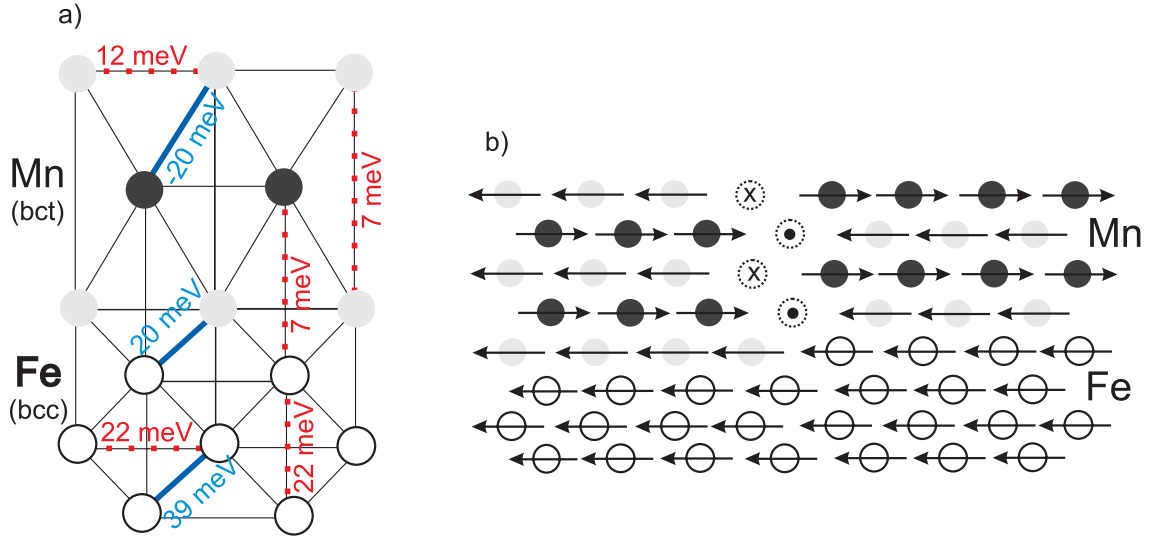
Figure 5.2: The lattice structure of bct Mn on Fe projected in the (100) plane is shown in a). The exchange coupling constants used in the calculations are indicated by numbers. The starting configuration for the calculations in a Heisenberg model is presented in b). The different gray levels of the localized magnetic moments are correlated to the Fe substrate and the layer-wise antiferromagnetic order of the Mn layers. The arrows represent the direction of the magnetic moments parallel or antiparallel to the Fe one and the dots and crosses the moments having an angle of $\pm 90°$.

for the next nearest neighbor exchange in the Mn film, we assumed a decay of the exchange with increasing distance ($r$) proportional to $\frac{1}{r^5}$. This assumption is based on tight binding calculations [124]. We are aware that this is only a rough estimate but ab-initio calculations of this Mn phase are not available. The calculated values for the nearest and next nearest neighbor exchange for bcc Fe have decay rates between $\frac{1}{r^3}$ and $\frac{1}{r^5}$ [121,125], which supports the assumption. Using this approximation and considering the tetragonal distortion in the Mn film we obtained a next nearest neighbor coupling constant of $J = 12$ meV for the in-plane exchange and $J = 7$ meV for the out-of-plane exchange. The coupling of next nearest neighbors is assumed to be ferromagnetic. At the interface between Fe and Mn the same exchange values are assumed as used in the Mn film.

The choice of the exchange coupling constants is summarized graphically in Fig. 5.2, where the three dimensional structure is projected into a two dimensional plane, for simplicity. The first Mn layer is assumed to couple ferromagnetically to the Fe layer. For the anisotropy the value for bulk Fe was taken ($K_i = 4$ $\mu$eV/atom [126]). In the case of thin Mn films, we are in the limit where the magnetically frustrated region is much thinner than a bulk domain wall. While in the latter case, the width is determined by the equilibrium between the exchange and the anisotropy energy, in thin films the width is dominated by the exchange interaction being much higher

than the anisotropy energy. Therefore, the anisotropy in the Mn film can be neglected. To confirm this approximation, test calculations were performed choosing different realistic values for the anisotropy in the Mn film. No changes occurred in the width of the calculated magnetically frustrated region. However, the anisotropy cannot be neglected in the Fe substrate due to the fact that the anisotropy limits the propagation of the magnetically frustrated region into the Fe substrate. In the calculation, the effect of strain or the lattice mismatch in the Mn film at the position of the buried Fe step edge caused by the difference in the out-of-plane lattice constant is not considered.

The starting configuration for the minimization of the energy is presented in Fig. 5.2b). The Fe film is homogeneously magnetized and consists of 70.5 ML. No influence of the magnetically frustrated region was found for thicker Fe films. The thickness of the Mn film is varied between 2.5 and 20.5 ML and an atomically sharp 180° wall is placed above an Fe step edge having the same width in every Mn layer. To check the influence of the starting configuration several different starting arrangements were chosen. For one configuration no magnetic frustration was inserted in the Mn film. The result and especially the calculated width of the magnetically frustrated region was found to be independent of the starting configuration, though the calculation time was significantly increased in some cases. Therefore, the above mentioned starting configuration, which is already close to the energy minimum, was chosen.

Fig. 5.3 shows the result of the calculation of a magnetically frustrated region of 20.5 ML Mn. The result is presented in a two-dimensional plot together with the underlying Fe substrate. Black and white areas correspond to MLs where the magnetic moments have an angle of 180° and 0° compared to the direction of non-tilted Fe magnetic moments. The rotation of the magnetic moments in the magnetically frustrated region is visible and the calculations show that the frustration is localized above the Fe step edge (Fig. 5.3a)). Fig. 5.3b) displays only the Fe film with enhanced contrast (more than 95%) to show the weak tilt of the Fe magnetic moments. The induced rotation of the Fe moments is at most 36° in the top most Fe layer close to the step edge, and it is already reduced to about 7° in a distance of 30 atoms in the plane away from the Fe step edge. In the 10th layer below the step the rotation is reduced to 12°. The size of the rotation of the Fe moments depends strongly on the Mn coverage. For low coverage nearly no rotation is found. From this model, we see that the magnetic frustration in the Mn film induces a torque on the Fe moments due to the exchange which results in a tilt of the Fe moments near the Fe step edge. This means that a topological defect can be associated with a long-range effect extending into the whole antiferromagnetic Mn film and into the ferromagnetic substrate. Calculations performed by Stoeffler and coworkers showed a similar behavior for Cr films overgrowing an Fe step edge [63]. In the calculations, it was found that the magnetic defect line extends into the whole Cr film and that the magnetic moments of the underlying Fe substrate are tilted close to the Fe step edge.
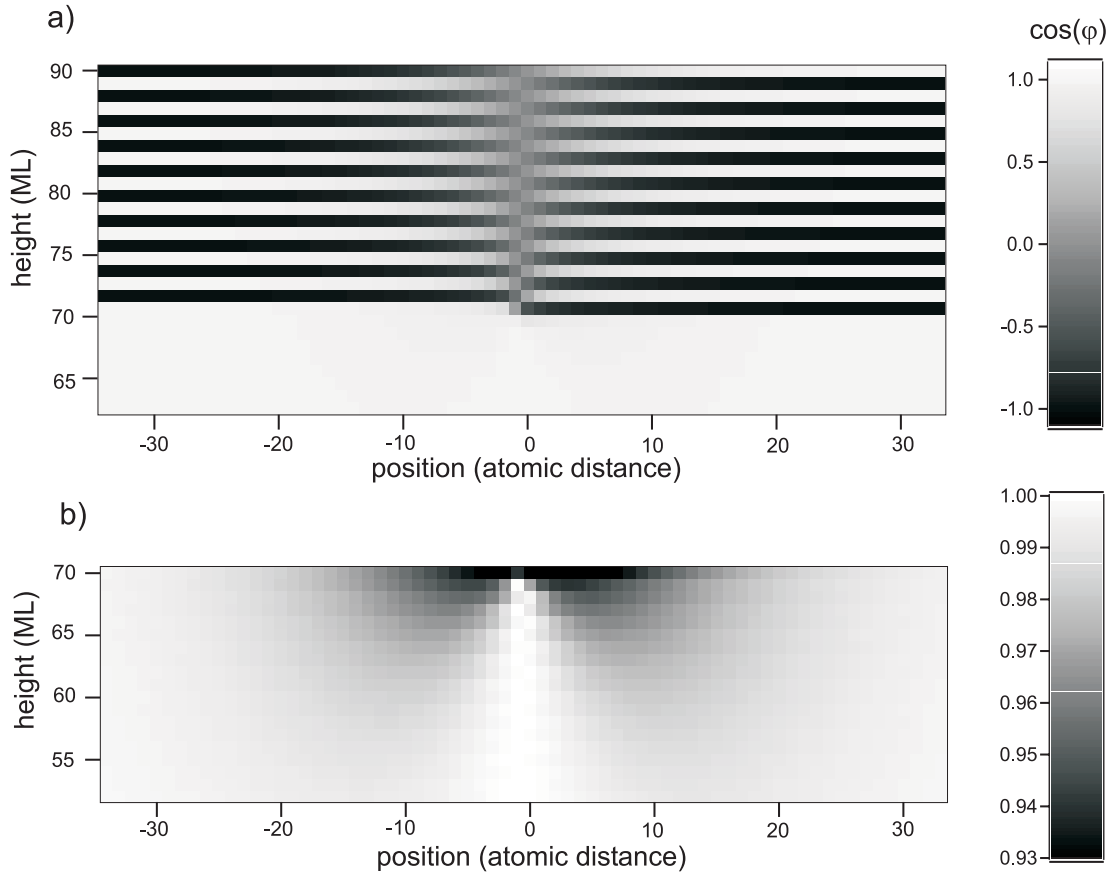
a)



b)



Figure 5.3: a) The calculated angle $\varphi$ of the local magnetic moments projected along the direction of the undisturbed Fe moments above and below an Fe step edge for a 20.5 ML thick Mn film. The first layers showing the alternating contrast present the antiferromagnetic order of adjacent Mn layers. The Fe magnetic moments below the step edge of a) are shown in b) with a considerably increased contrast (about 95%).

In Fig. 5.4a) a calculated line profile taken at the top most Mn layer in Fig. 5.3a) is shown. To determine the calculated wall width of the magnetically frustrated region, the curve was fitted with a *tanh*-function as in the case of the measured data. A good agreement between the calculated wall profile and the behavior of a *tanh*-function was found (red dots).

Fig.5.4b) shows the width of the magnetically frustrated region within a 20.5 ML thick Mn film from the interface to the Mn surface layer (dashed line). The wall width was determined from line profiles within the film presented in Fig. 5.3. A strong widening is found in the first few Mn layers above the interface and only small changes are found close to the surface layer. In this case, the ratio between the exchange coupling at the interface and in the Mn film is $J_{MnFe}/J_{Mn} = 1$. The product of both, the ratio of $J_{MnFe}/J_{Mn}$ and the film thickness is much bigger than
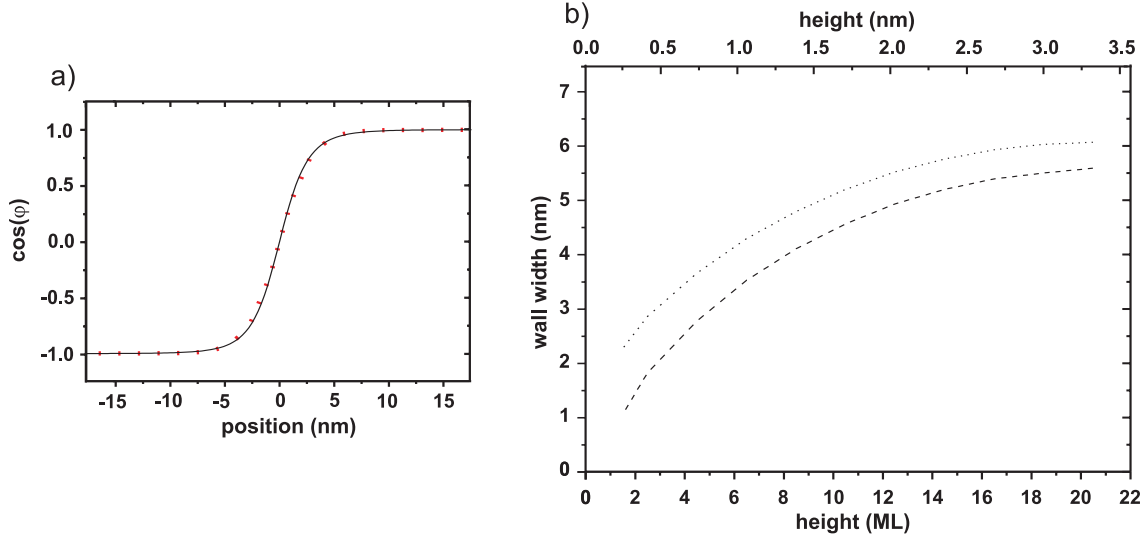
Figure 5.4: a) Calculated line profile projected along the direction of undisturbed Fe moments, taken at the surface of a 20.5 ML thick Mn film (black line) together with a fit of a *tanh*-function (red dots). b) Shows the calculated behavior of a wall within a 20.5 ML thick Mn film for the case that $J_{Mn}$ is equal $J_{MnFe}$ (dashed line) and $J_{MnFe}$ is four times smaller than $J_{Mn}$ (dotted line).

one. For this case, numerical simulations performed by Levchenko and coworkers [59] (for a general system consisting of a thin antiferromagnetic film on top of a ferromagnetic substrate) show a similar behavior of widening of a magnetic frustration within an antiferromagnetic film. In their calculations, a nearest neighbor Heisenberg model was used as a basic model for the simulations. When decreasing the ratio of $J_{MnFe}/J_{Mn}$, the numerical simulations of Levchenko and coworkers predict that the shape of the curve stays the same and that the curve is only shifted to higher wall width. By decreasing $J_{MnFe}/J_{Mn}$ by a factor four, our calculations yield the curve presented by dots in Fig.5.4b). In agreement with the simulations, the two curves showing nearly the same behavior and the one having a low ratio of $J_{MnFe}/J_{Mn}$ is only shifted to higher wall width.

In Fig. 5.5 the measured wall widths and the calculated widths are shown. Blue stars present the case where the energetic minimum of the magnetic frustrated Mn film was calculated by taking into account only the nearest neighbor exchange interaction. The calculated wall widths as a function of the Mn film thickness have a lower slope than the experimentally determined one and the widths of the walls are smaller. In a next step, the wall width was calculated by considering the nearest and next nearest neighbor exchange interaction. The values of our calculations are indicated by red stars in Fig. 5.5. The slope is much closer to the linear fit to the experimental data, but still a small offset occurs. The calculated width is again smaller than the experimental one. For both calculations a ratio of $J_{MnFe}/J_{Mn}$=1 was used.
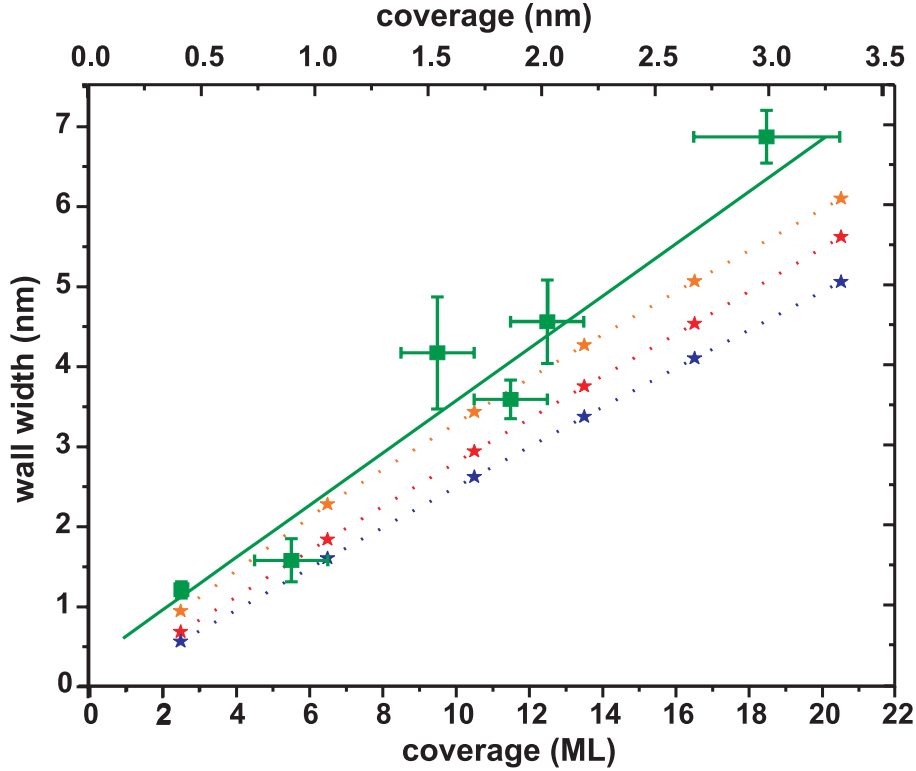
Figure 5.5: The measured data (green data points) with a linear fit (green line) shown in Fig. 4.10 are presented together with the calculated wall widths of the magnetically frustrated region using the Heisenberg model. The calculated data shown in blue are obtained by considering only the nearest neighbor exchange interaction and in red by considering the nearest as well as the next nearest neighbor exchange interaction and the bct structure of Mn. Using the same parameters as in the latter case and reducing the exchange at the interface to 25% one obtains the values presented in orange.

The width of the wall obtained in our calculation with the ratio of $J_{MnFe}/J_{Mn} = \frac{1}{4}$ is presented in orange in Fig. 5.5. The agreement to the experimental data is better than in the case that $J_{MnFe}/J_{Mn} = 1$ (red stars) which suggest that the exchange interaction at the interface between Fe and Mn may be reduced. This prediction is supported by the observation that at some areas no magnetic frustrations were observed at the surface of a Mn film above a buried Fe step indicating a relatively small interface coupling compared to the exchange of Mn (see section 4.2.1). Taking into account the crude approximations in particular for the exchange in the Mn film and at the interface, the agreement between the calculated wall width and the experimental one is rather satisfying.

The remaining difference between the calculated and experimental widths of the magnetically frustrated region may have several origins. The values for the exchange in the Mn film and at the interface are only estimated values. As has been shown, in

particular the exchange interaction at the interface is a critical parameter. Since in the experiment the Mn films were deposited on Fe having a temperature of 370 K, intermixing at the interface occurred which is also not included in the theoretical model. The lattice mismatch (caused by the difference in the out-of-plane lattice constant) at the position where Mn overgrows an Fe step edge is not considered as well. Possible changes of the exchange interaction or of magnetic moments close to the surface and interface are neglected. Several of the above discussed considerations can be taken into account by ab-initio calculations. Therefore, these calculations would be highly desirable for this system.

Both models, the Heisenberg model and the continuum model, describe the widening at the surface rather satisfying. The main difference between these two considerations is the behavior within the Mn film. In the Heisenberg model, a parabolic behavior was found while from the continuum model a linear widening is expected within the Mn film. The behavior within a Mn film is, however, not accessible with Sp-STM measurements.

## 5.2   Voltage dependent spin contrast

It may be surprising at first glance, that a spin contrast is observed on an antiferromagnetic surface. The basic requirement is the symmetry breaking at the sample surface. In the case of a layer-wise antiferromagnet, each ferromagnetic plane is spin-polarized but adjacent layers have opposite polarization. Therefore, a translation of the crystal by one ML is equivalent to a rotation of the spins by 180°. Due to symmetry reasons, bulk bands in layered antiferromagnets are spin-polarized but degenerate. At the surface, this symmetry is broken resulting in a possible non zero spin contrast at every bias voltages. Using the Sp-STM, this effect should result in a difference in the spin-polarized tunneling current measured between two neighboring Mn layers. Sp-STS studies performed at the surface of a layer-wise antiferromagnetic bulk Cr crystal [5] and Mn films on Fe(001) [6] showed that a spin contrast could be observed only close to spin-polarized surface states.

As we have seen in Fig. 4.13, we find a rather complex dependence of the spin contrast on the bias voltage for ultrathin Mn films on Fe(001) which is difficult to explain only by surface states. Thus, the question arises whether other states can also contribute to a spin polarization on antiferromagnetic surfaces.

Before we address this point, we will discuss the voltage dependent spin contrast measured with the Sp-STM on another antiferromagnetic material, thin Cr films on Fe(001). In this system, the situation seems to be simpler. We have obtained the data by the same technique and under similar conditions as used for the measurements for Mn on Fe(001), for details see section 4.2.2. Cr(001) surfaces show a layer-wise antiferromagnetic order similar to Mn on Fe(001), as illustrated for example by SEMPA (thin Cr films on Fe(001)) [45] and by Sp-STS (bulk Cr(001) single crystal) measurements [5].
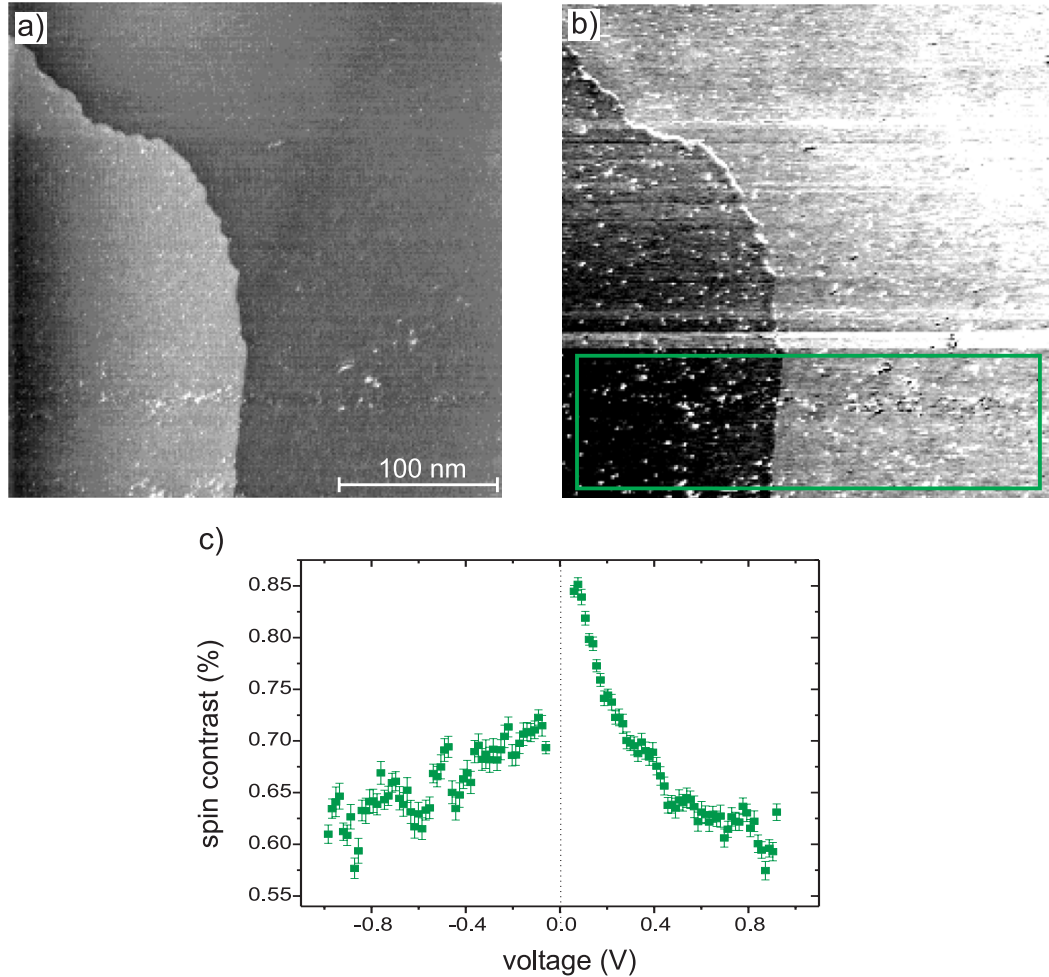
Figure 5.6: a) Topography and b) spin signal of a 12.8 ML thick Cr film on Fe(001). The two different gray levels in a) represent two Cr terraces separated by a monatomic step. The contrast in b) shows the antiferromagnetic order between the two Cr layers. The images were taken at a bias voltage of 0.08 V and an average tunneling current of 3 nA. c) Spin contrast as a function of the bias voltage, obtain within the green box in b). The spin contrast was measured between the 12 and 13 ML ($\pm 1$ ML) Cr.

An antiferromagnetic order of neighboring Cr layers grown on Fe(001) was imaged with Sp-STM. In Fig. 5.6, a Sp-STM measurement performed on a Cr film of 12.8 ML thickness deposited on Fe(001) at a substrate temperature of about 540 K is presented. In the topography (Fig. 5.6a)), two different Cr terraces are visible which show a different spin polarization in the corresponding spin signal (Fig. 5.6b)). The spin contrast between these two Cr terraces was measured as a function of the bias voltage and the result is shown in Fig. 5.6c). Except for an increase at positive voltages close to 0 V, a constant spin contrast of about 0.6% is observed. As

known from other publications, a surface state exists close to the Fermi level at about $-0.05$ V [5, 85]. Most likely, the increase of the spin contrast is caused by this surface state, which is spin-polarized, as shown e.g. by Sp-STS measurements [5]. Because of the dispersion of the surface state with $k_\parallel$, a shift in the energy can occur which may explain the slight shift in the energy position of our measured peak in the spin contrast[2]. In Sp-STS measurements performed on a bulk Cr(001) single crystal [5], a spin signal could only be found close to the spin-polarized surface state. Our observations on Cr films on Fe(001) suggest that the spin contrast measured at voltages different from that of the surface state could be caused by bulk states.

Now we come back to the more complex behavior of the spin contrast with the bias voltage found for Mn films on Fe(001). In this context, a more detailed description of antiferromagnetic bulk bands causing a spin-dependent tunneling current will be given.

To discuss possible underlying physical properties, we describe the relations between our experimental data and the band structure and the spin resolved spectral density of states calculations. Furthermore, the experimental behavior of the spin contrast is compared to calculations of the spin-dependent tunneling current performed for the system Fe(001)/vacuum/Mn/Fe(001) [118].

In general, the theoretical description of the tunneling process is done either in the Tersoff-Hamann or the Landauer-Büttiker approximation, which were introduced in section 2.2. In the Tersoff-Hamann model, only the local density of states at the sample surface at the position of the tip is taken into account. Using this model, a difference in the density of states for spin up and spin down electrons produces a spin-polarized tunneling current.

The calculations of the band structure and the Bloch spectral density of states for bct Mn [118] have been done from first-principles using the local spin-density approximation of the density-functional theory [128]. Here, an appropriate extension of the boundary conditions for surfaces and interfaces was taken into account [129]. The result for $k_\parallel = 0$ is presented in Fig. 5.7. The bands in bulk antiferromagnets are degenerate so that the dispersion $E(k)$ for spin up and spin down states is the same, as discussed before. Thus, the depicted bands represent two bands lying on top of each other (Fig. 5.7a)). The spectral density of states is labelled with $+M$ and $-M$ standing for adjacent Mn layers with opposite magnetization (Fig. 5.7b)). The spectral density of states is a local property in real space and thus spin up and spin down electrons show differences depending on the magnetization of the layer. The peaks arising at different energies are only caused by bulk states. No surface states were observed in these spectral density of states [118]. The calculations show that at different energies different spin characters dominate and that the order is reversed in

---

[2]During this Sp-STM measurement, the distance between the tip and the sample surface was varied as the tunneling current was kept fixed for different bias voltages (see section 4.2.2). Thus, in the range close to 0 V more states with $k_\parallel \neq 0$ contributed to the tunneling process in our Sp-STM experiment. The dispersion of surface states is well known for surface states on noble metals [127] and in Mn density of state calculations a similar but weaker effect was found [118].
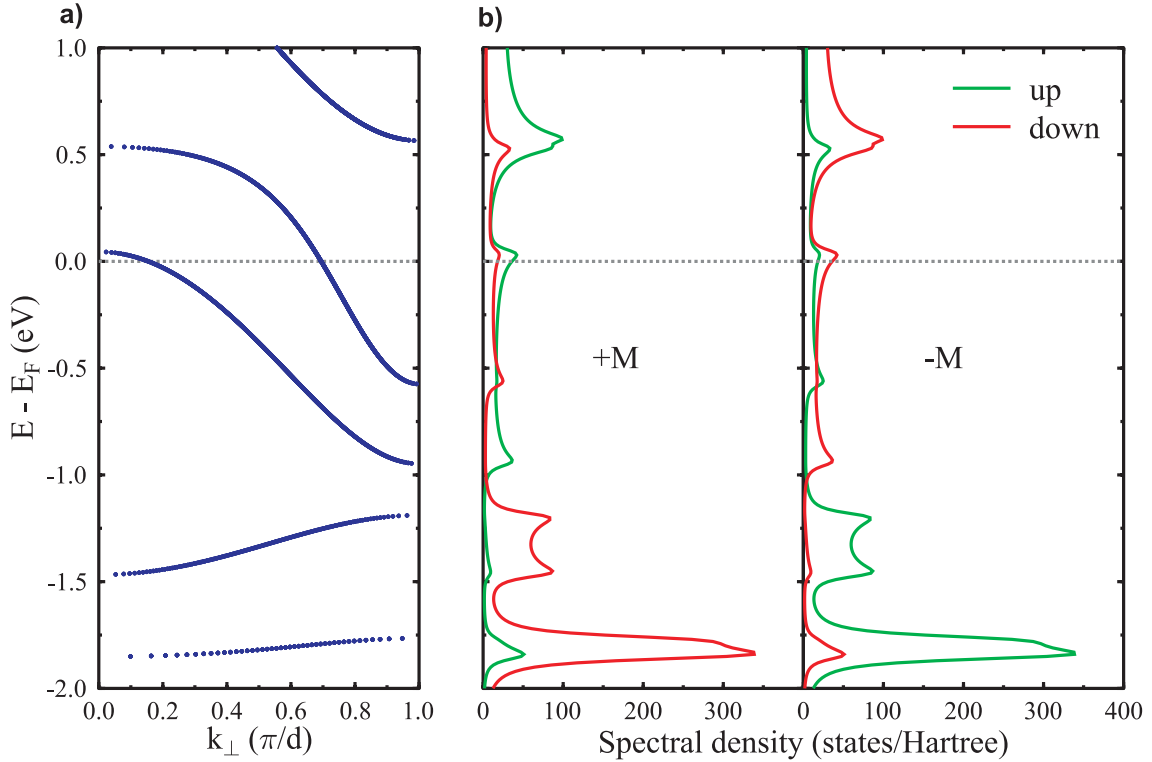
Figure 5.7: a) Result of band structure calculations of a layered antiferromagnetic bct bulk Mn crystal for $k_\parallel = 0$. b) Corresponding spin resolved spectral density for opposite spin-polarized Mn layers indicated by $+M$ and $-M$ [118].

$+M$ and $-M$ layers ($n_{up}(+M) = n_{down}(-M)$). This should result in a spin contrast for certain bias voltages. The experimental data in Fig. 4.13 show a change of sign of the spin contrast for a bias voltage just below 0 V. In the calculations a transition between the spin up and spin down character of the electron states below the Fermi energy is observed. Qualitatively, this change of spin states should produce a change of sign in the spin contrast.

The two shoulders visible in the experimental $(dI/dU)/(I/U)$ spectrum in Fig. 4.14 can be explained on the basis of the band structure and density of states. At the position of both shoulders at about $-0.5$ V and $+0.25$ V, a band edge is present which creates a small peak in the spectral density. This is most likely responsible for the experimentally measured plateau. The corresponding states of the above mentioned bands have a component perpendicular to the surface. They can contribute to the tunneling current. States of other bands have more contributions in the plane of the surface which results in a reduced transmission probability, like the band being responsible for the high peak at 0.5 V [118].

Another possible approach to describe the measured dependence of the spin contrast as a function of the bias voltage theoretically is a calculation of the current asymmetry based on the Landauer-Büttiker formalism. The current asymmetry $\delta$

is defined as the difference of the tunneling current for parallel ($I_P$) and antiparallel ($I_{AP}$) spin alignment of the two electrodes divided by the sum, $\delta = \frac{I_P - I_{AP}}{I_P + I_{AP}}$. $I_P$ and $I_{AP}$ are defined with respect to the direction of magnetization of the underlying Fe substrate. This formalism is a description of the transport in which the transmission probability between the different layers of the whole tunneling system is calculated. Here, realistic band structures are considered and the different matching of the electronic states between the layers is an important quantity for the determination of the tunneling current.

To calculate the spin-polarized tunneling current through thin antiferromagnetic Mn films, the layer-wise order is associated with a periodic arrangement of potential wells and potential barriers, like in a Kronig-Penney model [130]. Thus, an electron of a given spin direction sees an alternating step potential with a period of two ML and an electron of opposite spin is exposed to the same periodic repetition of the potentials but shifted by one ML. Therefore, the transmission of the spin-polarized electrons coming from the spin-polarized underlying Fe substrate is different travelling through an even or odd amount of Mn layers. The ballistic transport calculations of the spin-polarized tunneling current are performed for Mn layers on Fe separated by a vacuum gap from a pure Fe electrode representing the Sp-STM tip. Since in Sp-STM measurements, the tunneling current is determined by states close to the Fermi energy the current asymmetry is calculated for energies between -1 V and +0.6 V. To perform calculations of the current asymmetry using the simplified picture of a Kronig-Penney model, some simplifications of the calculated band structure were done. In this energy range, the Fe bands were approximated by one averaged band which is exchange split. For the antiferromagnetic Mn film the band structure was approximated also by one bulk band where the spin states are degenerate. The potential step in the Kronig-Penney model was chosen in the way to reproduce this band. The result of the current asymmetry is presented in Fig. 5.8a) [118]. The behavior is similar for opposite magnetized Mn layers (here shown for the case of 8 ML and 9 ML Mn) of course with the reversed sign. Above 6 ML Mn, no significant changes of the current asymmetry are expected because no changes are found in the spectral density of states. In Fig. 5.8b), the difference of the current asymmetry between these two oppositely magnetized Mn layers is plotted which represents the experimentally measured situation of the spin contrast.

The main conclusion of this simple model is that the calculated current asymmetry is small, of the order of 1% and changes sign between 0 V and -1 V. These two findings are in qualitative agreement with the experimental results presented in Fig. 4.13. This agreement could only be found when the Fe under the Mn film is considered which provides spin-polarized electrons travelling through the Mn film.

When comparing the experimental data to the ballistic transport theory, a critical parameter is the length that an electron travels before it looses its spin information. If this length is approximately equal to the Mn film thickness, the theory described above, breaks down. In layer-wise antiferromagnets, the spin character of majority and minority electrons alternates with a period of two ML. Thus, this
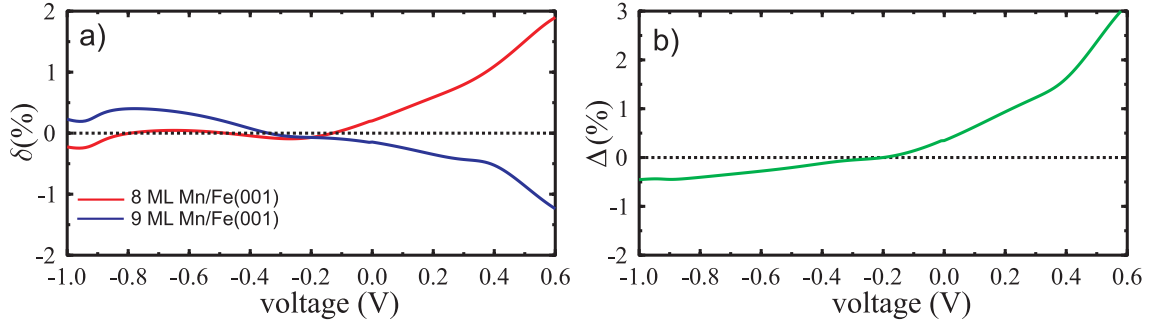
Figure 5.8: a) Calculations of the current asymmetry ($\delta$), the calculations are presented for oppositely magnetized Mn layers, here presented for the case of 8 ML and 9 ML Mn. The difference of the current asymmetry ($\Delta$) between both Mn layers is presented in b) [118].

length will be equal for majority and minority Fe electrons when films of several layers are considered. To the best of our knowledge, this length is unknown for Mn and it is also rather difficult to estimate the value. From literature it is known that the spin diffusion length in Co is about 40 nm [131] near the Fermi edge. This length decreases rapidly when the bias voltage increases. For 1 eV the averaged spin-dependent inelastic mean free path is about 30 Å [132,133]. The inelastic mean free path is, however, smaller than the length that an electron travels before it looses its spin information. Thus, the latter value can be assumed as an upper limit and Mn films under investigation had a thickness of about 20 Å, the theoretical model should be valid.

The calculated data are obtained for $k_\parallel = 0$ and for a constant distance between the Fe electrode and the Mn film surface. Since in the experiment the averaged tunneling current was kept constant while varying the bias voltage, the distance between ring and sample surface changed. This effect is only of importance for small tunneling voltages when the distance is reduced significantly. This might lead to changes in the contribution of states with $\vec{k}_\parallel \neq 0$, which are not considered in the calculations. Thus, the comparison of the experimental data and the calculations is problematic in the range close to 0 V. Hence, the model is not suited to describe the fine details of the experimental data. Considering the simplicity of the model, however, the principal behavior of the measured voltage-dependent spin contrast presented in Fig. 4.13 is in reasonable agreement with the calculated data in Fig. 5.8b). The theoretical model gives a possible explanation of the current asymmetry of thin antiferromagnetic films on a ferromagnetic substrate by considering only the bulk states of Mn. One should keep in mind that localized states, e.g. surface states, do not contribute to the tunneling current in the ballistic Landauer-Büttiker formalism while they will contribute in the Tersoff-Hamann model.

The increase of the measured spin contrast at about 0.1 V can be described on the basis of band structure calculations and spectral density of states. One possible

reason for this experimental finding could be the band edge of one Mn band close to the Fermi edge. Another explanation is based on the contribution of states with different $\vec{k}_\parallel$ which have been performed as well, but not presented here [118]. The calculations show that for certain $k_\parallel$ a localized resonance is formed at the interface between Fe and Mn and a localized surface state arises in the Mn surface layer at about 0.1 V. Both localized states show the same spin polarization which should lead to a higher transmission from the Fe into the Mn film and from Mn into the vacuum for one spin channel. This enhanced transmission for one spin channel can produce an increase of the measured spin contrast at 0.1 V.

In summery, two different possible theoretical explanations for the spin contrast observed at the Mn surface were introduced. On the one hand, the spin contrast can occur due to the different spin character of bulk Mn states visible in the spin-dependent density of states at the sample surface. On the other hand, the transmission probability of spin-polarized electrons from the underlying Fe could be different for even and odd layers of Mn and it can cause a different spin polarization at the Mn surface.

The calculations show that polarization effects on antiferromagnetic surfaces can arise without any spin-polarized surface states. However, it is likely that the highest spin contrast in both systems, Mn on Fe(001) and Cr on (Fe001), is caused by spin-polarized surface states.

# Chapter 6

# Conclusion

In this work, it was shown that Sp-STM can be used to image one well-defined in-plane component of the spin polarization of a sample surface with high lateral resolution. This was achieved by the proper choice of a Sp-STM electrode, namely a ring. The magnetization at the tunneling part of the ring lies in the plane of the sample surface. The plane of the ring defines the direction which the ring is sensitive to. Thus, a well-defined in-plane component can be imaged. By choosing either a ring or a tip electrode, the in-plane or the out-of-plane component of the spin polarization can be measured with the Sp-STM. The functionality of the new Sp-STM electrode was tested on a well characterized system, 180° domain walls at the surface of Fe-whiskers.

The capability of the Sp-STM was used to measure the spin arrangement of antiferromagnetic surfaces with a high lateral resolution of at least 1 nm. The main part of this work deals with the investigation of thin layer-wise antiferromagnetic ordered Mn films which are in direct contact to a ferromagnetic Fe(001) substrate. In addition, measurements were performed on thin layer-wise antiferromagnetic ordered Cr films on Fe(001). In the Sp-STM images, clearly the layer-wise antiferromagnetic order of adjacent Mn and Cr layers is visible. For Mn films, this behavior was observed up to about 20 ML where Mn undergoes a phase transition.

Magnetically frustrated regions were found at the surface of Mn films on Fe(001). The magnetic frustrations are explained by the interface roughness between Mn and Fe. When Mn is overgrowing a monatomic Fe substrate step, the Mn layer thickness is different by one atomic layer on both sides of the step. Assuming the same magnetic coupling between Mn and Fe on both sides of the step edge, the layer-wise antiferromagnetic order within the Mn film cannot be fulfilled on both sides of the step without creating a magnetic frustration. The investigation of the spin arrangement influenced by monatomic steps has been beyond the resolution limit of the established magnetic imaging techniques. Here, Sp-STM provides an ideal tool to probe the behavior of single, laterally confined magnetic frustrations. The possibility to image the topography and the magnetic signal simultaneously allows the correlation between magnetic structures and specific topographic features.

The Sp-STM experiments showed that a magnetic frustration appeared predominantly at the Mn film surface above a buried monatomic Fe substrate step. This suggests that a magnetic frustration is formed through the entire Mn film induced by a topological defect line. These kind of magnetic frustrations are different from natural bulk domain walls though they also show the rotation of the spin polarization by 180° from one side to the other. In contrast to bulk walls, the magnetic frustrations are pinned along substrate step edges and it was found that they are very narrow for thin Mn films. By investigating the width of these magnetic frustrations as a function of the Mn film thickness, a linear widening with increasing Mn thickness was observed. A width of the magnetically frustrated region between 1 nm (between the second and third ML Mn) and 7 nm (between the 18 and 19 ML Mn) was found.

The experimental finding of the widening of the magnetic frustration with increasing Mn film thickness was compared to two model descriptions of this effect, a continuum model and calculations based on a Heisenberg model. Both models reproduced the observed widening of the magnetic frustration at the Mn surface with increasing Mn film thickness rather satisfying. However, the behavior within the Mn films is significantly different for both models. Since Sp-STM is a surface sensitive technique, only the behavior at the Mn film surface could be investigated.

The Sp-STM experiments showed that the difference of the spin-dependent tunneling current measured between two oppositely spin-polarized Mn surface layers on Fe(001) depends on the bias voltage. The sign of the spin contrast changed in the investigated voltage range of +0.8 V to -1.4 V. In the case of Cr films on Fe(001), a constant spin contrast was found except for an enhancement close to the Fermi level. Likely, in both systems the highest spin contrast was observed near spin-polarized surface states. In the case of Mn, the behavior of the spin contrast as a function of the bias voltage was compared to calculations. Two different theoretical descriptions showed different mechanisms which could be responsible for the observed spin contrast. It was pointed out that a spin polarization at an antiferromagnetic surface can be explained solely by bulk states. Therefore, no spin-polarized surface states are needed to obtain a spin polarization at the surface of antiferromagnetic Mn films.

The presented Sp-STM measurements showed real space studies of magnetic frustrations caused by the influence of monatomic steps at an interface between two exchange coupled systems. Qualitatively, our results should hold also for other layered antiferromagnets in contact to a ferromagnet.

# Bibliography

[1] A. Yamasaki, W. Wulfhekel, R. Hertel, and J. Kirschner, Phys. Rev. Lett. **91**, 127201 (2003).

[2] A. Wachowiak, J. Wiebe, M. Bode, O. Pietzsch, M. Morgenstern, and R. Wiesendanger, Science **298**, 577 (2002).

[3] M. Bode, M. Getzlaff, and R. Wiesendanger, Phys. Rev. Lett. **81**, 4256 (1998).

[4] W. Wulfhekel and J. Kirschner, Appl. Phys. Lett. **75**, 1944 (1999).

[5] M. Kleiber, M. Bode, R. Ravlić, and R. Wiesendanger, Phys. Rev. Lett. **85**, 4606 (2000).

[6] T. K. Yamada, M. M. J. Bischoff, G. M. M. Heijnen, T. Mizoguchi, and H. van Kempen, Phys. Rev. Lett. **90**, 056803 (2003).

[7] U. Schlickum, W. Wulfhekel, and J. Kirschner, Appl. Phys. Lett. **83**, 2016 (2003).

[8] U. Schlickum, N. Janke-Gilman, W. Wulfhekel, and J. Kirschner, Phys. Rev. Lett. **92**, 107203 (2004).

[9] H. Barkhausen, Phys. Z. **20**, 401 (1919).

[10] S. Heinze, M. Bode, A. Kubetzka, O. Pietsch, X. Nie, S. Blügel, and R. Wiesendanger, Science **288**, 1805 (2000).

[11] F. Bitter, Phys. Rev. **41**, 507 (1932).

[12] A. Hubert, Phys. Status Solidi **24**, 669 (1967).

[13] Y. Martin and H. K. Wickramasinghe, Appl. Phys. Lett. **50**, 1455 (1987).

[14] L. Abelmann, S. Porthun, M. Haast, C. Lodder, A. Moser, M. E. Best, P. J. A. van Schendel, B. Stiefel, H. J. Hug, G. P. Heydon, A. Farley, S. R. Hoon, T. Pfaffelhuber, R. Proksch, and K. Babcock, J. Magn. Magn. Mater. **190**, 135 (1998).

[15] H. J. Williams, F. G. Foster, and E. A. Wood, Phys. Rev. **82**, 119 (1951).

[16] C. Durkan, I. V. Shvets, and J. C. Lodder, Appl. Phys. Lett. **70**, 1323 (1997).

[17] P. Fumagalli, A. Rosenberger, G. Eggers, A. Münnemann, N. Held, and G. Güntherodt, Appl. Phys. Lett. **72**, 2803 (1998).

[18] B. L. Petersen, A. Bauer, G. Meyer, T. Crecelius, and G. Kaindl, Appl. Phys. Lett. **73**, 538 (1998).

[19] K. Koike and K. Hayakawa, Appl. Phys. Lett. **45**, 585 (1984).

[20] M. R. Scheinfein, J. Unguris, M. Aeschlimann, D. T. Pierce, and R. J. Celotta, J. Magn. Magn. Mater. **93**, 109 (1991).

[21] H. Matsuyama and K. Koike, J. of Electron Microscopy **43**, 157 (1994).

[22] R. Allenspach, IBM J. Res. Dev. **44**, 553 (2000).

[23] T. Kohashi and K. Koike, Jap. J. Appl. Phys. **40**, L1264 (2001).

[24] C. T. Chen, Y. U. Idzerda, H. J. Lin, G. Meigs, A. Chaiken, G. A. Prinz, and G. H. Ho, Phys. Rev. B **48**, 642 (1993).

[25] G. Binnig, H. Rohrer, C. Gerber, and E. Weibel, Appl. Phys. Lett. **40**, 178 (1981).

[26] G. Binnig, H. Rohrer, C. Gerber, and E. Weibel, Phys. Rev. Lett. **49**, 57 (1982).

[27] D. T. Pierce, Physica Scripta **38**, 291 (1988).

[28] M. Jullière, Phys. Lett. **54A**, 225 (1975).

[29] M. Johnson and J. Clarke, J. Appl. Phys. **67**, 6141 (1990).

[30] R. Wiesendanger, H. J. Güntherodt, G. Güntherodt, R. J. Gambino, and R. Ruf, Phys. Rev. Lett. **65**, 247 (1990).

[31] M. W. J. Prins, R. Jansen, and H. van Kempen, Phys. Rev. B **53**, 8105 (1996).

[32] Y. Suzuki, W. Nabhan, and K. Tanaka, Appl. Phys. Lett. **71**, 3153 (1997).

[33] H. Kodama, T. Uzumaki, M. Oshiki, K. Sueoka, and K. Mukasa, J. Appl. Phys. **83**, 6831 (1998).

[34] M. Pratzer, H. J. Elmers, M. Bode, O. Pietzsch, A. Kubetzka, and R. Wiesendanger, Phys. Rev. Lett. **87**, 127201 (2001).

[35] H. F. Ding, W. Wulfhekel, and J. Kirschner, Europhys. Lett. **57**, 100 (2002).

[36] C. Kittel, *Einführung in die Festkörperphysik*, R. Oldenbourg Verlag, München, Wien, 1999.

[37] W. Heisenberg, Z. Phys. **38**, 411 (1926).

[38] A. Aharoni, *Introduction to the theory of ferromagnetism*, Clarendon Press., Oxford, 1996.

[39] E. C. Stoner, Proc. Roy. Soc. A **154**, 656 (1936).

[40] E. C. Stoner, Proc. Roy. Soc. A **165**, 372 (1938).

[41] P. Mohn, *Magnetism in the Solid State*, Springer, Berlin, Heidelberg, New York, Hong Kong, London, Milan, Paris, Tokyo, 2003.

[42] V. L. Moruzzi, J. F. Janak, and A. R. Williams, *Calculated Electronic Properties of Metals*, Pergamon Press Inc., New York, Toronto, Oxford, Sydney, Frankfurt, Paris, 1978.

[43] J. X. Shen and M. T. Kief, J. Appl. Phys. **79**, 5008 (1996).

[44] T. G. Walker, A. W. Pang, H. Hopster, and S. F. Alvarado, Phys. Rev. Lett. **69**, 1121 (1992).

[45] D. T. Pierce, J. Unguris, R. J. Celotta, and M. D. Stiles, J. Magn. Magn. Mater. **200**, 290 (1999).

[46] T. G. Walker and H. Hopster, Phys. Rev. B **48**, 3563 (1993).

[47] D. A. Tulchinsky, J. Unguris, and R. J. Celotta, J. Magn. Magn. Mater. **212**, 91 (2000).

[48] A. Hubert and R. Schäfer, *Magnetic domains: the analysis of magnetic microstructures*, Springer, Berlin, 1998.

[49] A. E. LaBonte, J. Appl. Phys. **40**, 2450 (1968).

[50] A. Scholl, J. Stöhr, J. Lüning, J. W. Seo, J. Fompeyrine, H. Siegwart, J. P. Locquet, F. Nolting, S. Anders, E. E. Fullerton, M. R. Scheinfein, and H. A. Padmore, Science **287**, 1014 (2000).

[51] F. Nolting, A. Scholl, J. Stöhr, J. W. Seo, J. Fompeyrine, H. Siegwart, J. P. Locquet, S. Anders, J. Lüning, E. E. Fullerton, M. F. Tonney, M. R. Scheinfein, and H. A. Padmore, Nature **405**, 767 (2000).

[52] H. Ohldag, A. Scholl, F. Nolting, S. Anders, F. U. Hillebrecht, and J. Stöhr, Phys. Rev. Lett. **86**, 2878 (2001).

[53] N. B. Weber, H. Ohldag, H. Gomonaj, and F. U. Hillebrecht, Phys. Rev. Lett. **91**, 237205 (2003).

[54] E. Gomonay and V. Loktev, J. Magn. Magn. Mater. **242-245**, 1418 (2002).

[55] A. Berger and H. Hopster, Phys. Rev. Lett. **73**, 193 (1994).

[56] A. Berger and E. E. Fullerton, J. Magn. Magn. Mater **165**, 471 (1997).

[57] A. I. Morosov and A. S. Sigov, Phys. Solid State **46**, 395 (2004).

[58] D. Stoeffler, Spin Structures in Metallic Multilayers: theoretical aspects, in *Magnetische Schichtsysteme in Forschung und Anwendung, 30. Ferienkurs des Institutes für Festkörperforschung*, pages B4.1–28, Forschungszentrum Jülich, 1999.

[59] V. D. Levchenko, Y. S. Sigov, A. I. Morozov, and A. S. Sigov, J. of exp. and theo. Phys. **87**, 985 (1998).

[60] A. Vega, C. Demangeat, H. Dreyssé, and A. Chouairi, Phys. Rev. B **51**, 11546 (1995).

[61] E. E. Fullerton, K. T. Riggs, C. H. Sowers, S. D. Bader, and A. Berger, Phys. Rev. Lett. **75**, 330 (1995).

[62] D. Stoeffler and F. Gautier, J. Magn. Magn. Mater. **147**, 260 (1995).

[63] R. Robles, E. Martínez, D. Stoeffler, and A. Vega, Phys. Rev. B **68**, 094413 (2003).

[64] C. Bai, *Scanning Tunneling Microscopy and its Application*, Springer, Berlin, Heidelberg, New York, Barcelona, Budapest, Hong Kong, London, Milan, Paris, Tokyo, 1995.

[65] J. Tersoff and D. R. Hamann, Phys. Rev. Lett. **50**, 1998 (1983).

[66] J. Tersoff and D. R. Hamann, Phys. Rev. B **31**, 805 (1985).

[67] Y. Kuk, *Scanning Tunneling Microscopy I*, edited by H. J. Güntherodt and R. Wiesendanger, Springer, Berlin, 1994.

[68] S. A. Komolov, *Total Current Spectroscopy of Surfaces*, Gordon and Breach Science Publishers, Philadelphia, 1992.

[69] S. Blügel, Theorie der Rastertunnelmikroskopie, in *Physik der Nanostrukturen, 29. Ferienkurs des Institutes für Festkörperforschung*, pages A3.1–55, Forschungszentrum Jülich, 1998.

[70] M. Büttiker, Phys. Rev. Lett. **57**, 1761 (1986).

[71] N. Müller, W. Eckstein, W. Heiland, and W. Zinn, Phys. Rev. Lett. **29**, 1651 (1972).

[72] M. Landolt and Y. Yafet, Phys. Rev. Lett. **40**, 1401 (1978).

[73] Landolt-Börnstein, *Magnetic Properties of Metals, New Series III / 19a*, Springer-Verlag, Berlin, Heidelberg, New York, London, Paris, Tokyo, 1986.

[74] J. C. Slonczewski, Phys. Rev. B **39**, 6995 (1989).

[75] J. M. MacLaren, X. G. Zhang, and W. H. Butler, Phys. Rev. B **56**, 11827 (1997).

[76] W. H. Butler, X. G. Zhang, X. Wang, J. van Ek, and J. M. MacLaren, J. Appl. Phys. **81**, 5518 (1997).

[77] J. M. MacLaren, X. G. Zhang, W. H. Butler, and X. Wang, Phys. Rev. B **59**, 5470 (1999).

[78] W. H. Butler, X. G. Zhang, T. C. Schulthess, and J. M. MacLaren, Phys. Rev. B **63**, 054416 (2001).

[79] O. Wunnicke, N. Papanikolaou, R. Zeller, P. H. Dederichs, V. Drchal, and J. Kudrnovský, Phys. Rev. B **65**, 064425 (2002).

[80] H. F. Ding, W. Wulfhekel, J. Henk, P. Bruno, and J. Kirschner, Phys. Rev. Lett. **90**, 116603 (2003).

[81] J. Henk and P. Bruno, Phys. Rev. B **68**, 174430 (2003).

[82] N. Papanikolaou, J. Opitz, P. Zahn, and I. Mertig, Phys. Rev. B **66**, 165441 (2002).

[83] W. Wulfhekel, H. F. Ding, W. Lutzke, G. Steierl, M. Vázquez, P. Marín, A. Hernando, and J. Kirscher, Appl. Phys. A **72**, 463 (2001).

[84] A. Kubetzka, M. Bode, O. Pietzsch, and R. Wiesendanger, Phys. Rev. Lett. **88**, 057201 (2002).

[85] J. A. Stroscio, D. T. Pierce, A. Davies, R. J. Celotta, and M. Weinert, Phys. Rev. Lett. **75**, 2960 (1995).

[86] M. Bode, A. Wachowiak, J. Wiebe, A. Kubetzka, M. Morgenstern, and R. Wiesendanger, Appl. Phys. Lett. **84**, 948 (2004).

[87] R. Vollmer, Lineare und nichtlineare Magnetoptik an ultradünnen ferromagnetischen Schichten und Vielfachschichten, in *Magnetische Schichtsysteme in Forschung und Anwendung, 30. Ferienkurs des Institutes für Festkörperforschung*, pages C7.1–34, Forschungszentrum Jülich, 1999.

[88] Micro-STM, Omicron Vacuumphysik GmbH, Germany.

[89] J. V. Barth, H. Brune, G. Ertl, and R. J. Behm, Phys. Rev. B **42**, 9307 (1990).

[90] M. A. van Hove, R. J. Koestner, P. C. Stair, J. P. Bibérian, L. L. Kesmodel, I. Bartoš, and G. A. Somorjai, Surf. Sci. **103**, 189 (1981).

[91] H. Theuss, B. Hofmann, C. Gómez-Polo, M. Vázquez, and Kronmüller, J. Magn. Magn. Mater. **145**, 165 (1995).

[92] image is kindly provided by H. Menge, MPI für Mikrostrukturphysik .

[93] M. R. Scheinfein, J. Unguris, R. J. Celotta, and D. T. Pierce, Phys. Rev. Lett. **63**, 668 (1989).

[94] H. P. Oepen and J. Kirschner, Phys. Rev. Lett. **62**, 819 (1989).

[95] E. Zueco, R. Rave, W. Schäfer, M. Mertig, and L. Schulz, J. Magn. Magn. Mater. **196**, 115 (1999).

[96] M. R. Scheinfein, J. Unguris, J. L. Blue, K. J. Coakley, D. T. Pierce, R. J. Celotta, and P. J. Ryan, Phys. Rev. B **43**, 3395 (1991).

[97] C. G. Shull and M. K. Wilkinson, Rev. Mod. Phys. **25**, 100 (1953).

[98] R. W. G. Wyckoff, *Crystal Structures*, Interscience Publisher, New York, London, Sydney, 1963.

[99] B. Heinrich, A. S. Arrott, C. Liu, and S. T. Purcell, J. Vac. Sci. Technol. A **5**, 1935 (1987).

[100] S. T. Purcell, M. T. Johnson, N. W. E. McGee, R. Coehoorn, and W. Hoving, Phys. Rev. B **45**, 13064 (1992).

[101] S. K. Kim, Y. Tian, M. Montesano, F. Jona, and P. M. Marcus, Phys. Rev. B **54**, 5081 (1996).

[102] S. Andrieu, M. Finazzi, P. Bauer, H. Fischer, P. Lefevre, A. Traverse, K. Hricovini, G. Krill, and M. Piecuch, Phys. Rev.B **57**, 1985 (1998).

[103] R. Pfandzelter, T. Igel, and H. Winter, Surf. Sci. **389**, 317 (1997).

[104] D. T. Pierce, A. D. Davies, J. A. Stroscio, D. A. Tulchinsky, J. Unguris, and R. J. Celotta, J. Magn. Magn. Mater. **222**, 13 (2000).

[105] T. K. Yamada, M. M. J. Bischoff, T. Mizoguchi, and H. van Kempen, Surf. Sci. **516**, 179 (2002).

[106] H. Brune and K. Kern, Heteroepitaxial metal growth: the effects of strain, in *The Chemical Physics of Solid Surfaces*, edited by D. A. King and D. P. Woodruff, volume 8 of *Growth and Properties of Ultrathin Epitaxial Layers*, pages 146–206, Elsevier, 1997.

[107] M. M. J. Bischoff, T. Yamada, A. J. Quinn, and H. van Kempen, Surf. Sci. **501**, 155 (2002).

[108] S. Andrieu, M. Finazzi, F. Yubero, H. Fischer, P. Arcade, F. Chevrier, K. Hricovini, G. Krill, and M. Piecuch, J. Magn. Magn. Mater. **165**, 191 (1997).

[109] S. Andrieu, M. Finazzi, F. Yubero, H. M. Fischer, P. Arcade, F. Chevrier, L. Hennet, K. Hricovini, G. Krill, and M. Piecuch, Europhys. Lett. **38**, 459 (1997).

[110] O. Rader, W. Gudat, D. Schmitz, C. Carbone, and W. Eberhardt, Phys. Rev. B **56**, 5053 (1997).

[111] C. Roth, T. Kleeman, F. U. Hillebrecht, and E. Kisker, Phys. Rev. B **52**, R15691 (1995).

[112] S. Andrieu, E. Foy, H. Fischer, M. Alnot, F. Chevrier, G. Krill, and M. Piecuch, Phys. Rev. B **58**, 8210 (1998).

[113] E. Kneller, *Ferromagnetismus*, Spinger, Berlin, Göttingen, Heidelberg, 1962.

[114] H. Kronmüller and M. Fähnle, *Micromagnetism and the Microstructure of Ferromagnetic solids*, Cambridge University Press, Cambridge, 2003.

[115] W. Wernsdorfer, E. B. Orozco, K. Hasselbach, A. Benoit, B. Barbara, N. Demoncy, A. Loiseau, H. Pascard, and D. Mailly, Phys. Rev. Lett. **78**, 1791 (1997).

[116] G. D. Fuchs, N. C. Emley, I. N. Krivorotov, P. M. Braganca, E. M. Ryan, S. I. Kiselev, J. C. Sankey, D. C. Ralph, and R. A. Buhrman, Appl. Phys. Lett. **cond-mat/0404002** (2004).

[117] H. F. Ding, W. Wulfhekel, U. Schlickum, and J. Kirschner, Europhys. Lett. **63**, 419 (2003).

[118] J. Henk, MPI für Mikrostrukturphysik , private communication.

[119] D. Jiles, *Introduction to Magnetism and Magnetic Materials*, Chapman & Hall, London, Weinheim, New York, Melbourne, Madras, 1996.

[120] R. Ravlić, M. Bode, A. Kubetzka, and R. Wiesendanger, Phys. Rev. B **67**, 174411 (2003).

[121] M. Pajda, J. Kudrnovský, I. Turek, V. Drchal, and P. Bruno, Phys. Rev. B **64**, 174402 (2001).

[122] S. Bouarab, H. Nait-Laziz, M. A. Khan, C. Demangeat, H. Dreyssé, and M. Benakki, Phys. Rev. B **52**, 10127 (1995).

[123] P. Krüger, O. Elmouhssine, C. Demangeat, and J. C. Parlebas, Phys. Rev. B **54**, 6393 (1996).

[124] A. P. Sutton, M. W. Finnis, D. G. Pettifor, and Y. Ohta, J. Phys. C **21**, 35 (1988).

[125] S. Morán, C. Ederer, and M. Fähnle, Phys. Rev. B **67**, 012407 (2003).

[126] P. Escudier, Ann. Phys. (Paris) **9**, 125 (1975).

[127] F. Reinert, G. Nicolay, S. Schmidt, D. Ehm, and S. Hüfner, Phys. Rev. B **63**, 115415 (2001).

[128] J. P. Perdew and Y. Wang, Phys. Rev. B **45**, 13244 (1992).

[129] A. Ernst, J. Henk, and P. Bruno, to be published .

[130] R. E. Hummel, *Electronic Properties of Materials*, Springer, Berlin, Heidelberg, New York, Barcelona, Budapest, Hong Kong, London, Paris, Tokyo, 1993.

[131] L. Piraux, S. Dubois, A. Fert, and L. Belliard, Euro. Phys. J. B **4**, 413 (1998).

[132] M. Aeschlimann, M. Bauer, S. Pawlik, W. Weber, R. Burgermeister, D. Oberli, and H. C. Siegmann, Phys. Rev. Lett. **79**, 5158 (1997).

[133] S. van Dijken, X. Jiang, and S. S. P. Parking, Phys. Rev. Lett. **90**, 197203 (2003).

# Deutsche Zusammenfassung

In dieser Arbeit wurde gezeigt, dass mit der spinpolarisierten Rastertunnelmikroskopie (spin-polarized scanning tunneling microscopy (Sp-STM)) eine wohldefinierte Komponente der Spinpolarisation in der Ebene der Probenoberfläche mit einer hohen lateralen Auflösung abgebildet werden kann. Als Rasterelektrode wurde ein ferromagnetischer Ring eingesetzt. In der Messung wird die Projektion der Spinpolarisation der Probe auf die Richtung der Magnetisierung des Rings abgebildet. Die Funktionstüchtigkeit der Ringelektrode wurde an einem gut untersuchten System, 180° Domänenwänden in Fe-Wiskern getestet.

Die Methode des Sp-STM wurde eingesetzt, um die Spinanordnung von antiferromagnetischen Oberflächen zu untersuchen. Der Schwerpunkt dieser Arbeit ist die Abbildung von dünnen, lagenweise antiferromagnetischen Mn und Cr Filmen in direktem Kontakt mit einem ferromagnetischen Fe(001) Substrate. In den Sp-STM Bildern ist die antiferromagnetische Ordnung von aufeinanderfolgenden Mn beziehungsweise Cr Lagen an der Oberfläche deutlich sichtbar.

An der Oberfläche von Mn Filmen auf Fe(001) wurden magnetisch frustrierte Bereiche gefunden. Diese Bereiche, in denen die magnetische Ordnung gestört ist, wurden durch das Vorhandensein von atomaren Stufen an der Grenzfläche zwischen Film und Substrat erklärt. Bildet ein Mn Film über einer atomaren Substratstufe eine atomar glatte Oberfläche, so unterscheidet sich die Schichtdicke auf beiden Seiten der Substratstufe um genau eine Lage. Somit ist eine ungestörte lagenweise antiferromagnetische Ordnung in dem Mn Film nicht möglich, wenn die magnetischen Mn Momente an der Grenzfläche auf beiden Seiten der Stufe vom ferromagnetischen Substrat gleich ausgerichtet werden. Das Resultat sind magnetisch frustrierte Bereiche.

Für die Untersuchung der Spinanordnung in den Mn Filmen, die durch atomare Fe Stufen beeinflusst wird, ist das Sp-STM eine geeignete Messmethode. Im Vergleich zu etablierten magnetischen Abbildungstechniken, erlauben Sp-STM Messungen die Untersuchung magnetischer Strukturen mit höchster lateraler Auflösung. Die Sensitivität zu einzelnen, lateral begrenzten magnetischen Strukturen und die gleichzeitige Abbildung der Topographie der Probenoberfläche erlaubt die Korrelation beider.

Die Sp-STM Untersuchungen zeigten, dass magnetische Frustrationen überwiegend über vergrabenen Fe Stufen an der Oberfläche von Mn auftreten. Diese Beobachtung deutet darauf hin, dass sich die magnetisch frustrierten Bereiche durch den gesamten Mn Film, vom Substrat bis zur Oberfläche ausbilden. Diese magnetischen Frustrationen sind keine natürlichen Domänenwände, obwohl sich die Magnetisierung in ihnen ebenfalls um 180° dreht. Im Unterschied zu Volumenwänden sind die magnetisch frustrierten Bereiche lokal an Substratstufen gebunden. Die Breite dieser frustrierten Bereiche ist für dünne Filme viel schmaler als für

Domänen-wandbreiten im Volumen zu erwarten wäre. Die Untersuchung der magnetisch frustrierten Bereiche als Funktion der Mn Schichtdicke zeigten, dass sich diese Bereiche linear mit zunehmender Mn Schichtdicke aufweiten. Es wurden Breiten von 1 nm zwischen der zweiten und dritten Monolage bis 7 nm zwischen der 18 und 19 Monolage gemessen.

Die experimentell ermittelten Breiten der magnetisch frustrierten Bereiche wurden mit zwei Modellen verglichen, einem Kontinuumsmodell und einem Heisenbergmodell. Beide Modelle reproduzieren den Verlauf der Aufweitung der magnetisch frustrierten Bereiche an der Oberfläche zufriedenstellend. Die Modelle unterscheiden sich hingegen in der Beschreibung der magnetischen Frustrationen im Inneren der Mn Filme. Da das Sp-STM eine oberflächensensitive Methode ist, ist es nur möglich das Verhalten an der Oberfläche zu untersuchen, an der sich nur geringfügige Unterschiede zwischen den Modellen ergeben.

Die Experimente zeigten außerdem, dass der Spinkontrast, gemessen zwischen zwei entgegengesetzt spinpolarisierten Mn beziehungsweise Cr Terrassen, stark von der angelegten Spannung abhängt. Der Spinkontrast auf Cr Filmen ist, bis auf eine Erhöhung nahe einer angelegten Spannung von 0 V, konstant. Im Falle von Mn zeigte sich ein relativ kompliziertes Verhalten. Zum Beispiel kommt es zu einem Vorzeichenwechsel des Spinkontrastes in dem untersuchten Spannungsbereich. Vermutlich wurde der höchste Spinkontrast in beiden Systemen nahe eines spinpolarisierten Oberflächenzustandes gemessen. Ein Vergleich mit theoretischen Berechnungen für dünne Mn Filme auf einem Fe Substrat zeigte, dass verschiedene Mechanismen für einen Spinkontrast an Mn Obflächen verantwortlich sein können. Es wurde gezeigt, dass eine Spinpolarisation an antiferromagnetischen Oberflächen auch alleine durch Volumenzustände hervorgerufen werden kann.

Die Sp-STM Messungen dieser Arbeit zeigten Realraumabbildungen von magnetischen Frustrationen, die durch atomare Stufen an der Grenzfläche zwischen zwei austauschgekoppelten magnetischen Systemen entstanden. Die Untersuchungen sollten qualitativ für andere lagenweise antiferromagnetische Filme in Kontakt zu ferromagnetischen Substraten gelten.

# Danksagung

Bedanken möchte ich mich an erster Stelle bei Herrn Prof. Dr. Jürgen Kirschner für die Möglichkeit, die vorliegende Arbeit durchzuführen, seine Diskussionsbereitschaft und seine vielen wertvollen Anregungen und Vorschläge.

Danken möchte ich Herrn Dr. habil. Wulf Wulfhekel für seine ständige Hilfsbereitschaft, seine Geduld und den Austausch von Ideen.

Mein ganz besonderer Dank gilt Herrn Markus Etzkorn für seine Unterstützung in jeglicher Hinsicht, vielen Dank!

Für ausführliche Diskussionen möchte ich mich besonders bedanken bei Herrn Dr. habil. Wolfgang Kuch, Herrn Dr. habil. Dirk Sander, Herrn Dr. Riccardo Hertel, Herrn Dr. Jürgen Henk, Herrn Dr. Rüdiger Vollmer und Herrn Prof. Dr. Bretislav Heinrich.

Danken möchte ich auch Herrn Dr. Haifeng Ding für die Einführung in Sp-STM Untersuchungen und Frau Barbara Slovik und Herrn Dr. Nathaniel Janke-Gilman für die experimentelle Unterstützung.

Bei Frau Heike Menge bedanke ich mich für die Bereitstellung von Kristallen und die Unterstützung beim Herstellen der Ringe.

Mein Dank gilt des weiteren Herrn Herbert Engelhard, Herrn Detlef Hartung, der elektronischen und mechanischen Werkstatt für Ihre technische Unterstützung.

Nicht zu vergessen sind alle Mitarbeiter, die zu einer angenehmen und schönen Arbeitsatmosphäre beigetragen haben: Dr. Anil Kumar, Dr. Carsten Winkler, Prof. Dr. Marek Przybylski, Carsten Tieg und alle anderen.

Mein ganz persönlicher Dank gilt meinen Eltern, die mich in allen Dingen hilfreichend unterstützt haben.

**Allen nochmals vielen Dank!**

# Erklärung an Eides statt

Hiermit erkläre ich, die vorliegende Dissertation

*Spin-polarized scanning tunneling microscopy studies on in-plane magnetization components of thin antiferromagnetic films on Fe(001)*

selbständig und ohne fremde Hilfe verfasst und keine anderen als die von mir angegebenen Quellen und Hilfsmittel benutzt zu haben. Die den benutzten Werken wörtlich oder inhaltlich entnommenen Stellen sind als solche kenntlich gemacht.

Halle, den 06.08.2004

Uta Schlickum

# Lebenslauf

**Persönliche Daten:**

| | |
|---|---|
| Name: | Katharina Uta Schlickum |
| Geburtsdatum: | 01.01.1976 |
| Geburtsort: | Herdecke |
| Familienstand: | ledig |

**Allgemeine Hochschulreife:**

| | |
|---|---|
| Juni 1996: | Abitur am Gymnasium Siegesstrasse in Wuppertal |

**Wissenschaftlicher Werdegang:**

| | |
|---|---|
| Oktober 1996 bis Juni 2001: | Studium der Geophysik an der Ruhr-Universität Bochum |
| Oktober 2000 bis Juni 2001: | Diplomarbeit mit dem Titel: *Surface Waves and Dispersion Analysis* |
| ab August 2001: | Doktorandin am Max-Planck-Institut für Mikrostrukturphysik in Halle |

Halle, den 06.08.2004

Uta Schlickum